IMPERIAL COLLEGE LONDON

DOCTORAL THESIS

Reducing uncertainty in climate prediction: enhancing the science case for TRUTHS

Author:
Amy SEALES

Supervisors:
Dr. Helen BRINDLEY
Dr. Paul GREEN

A thesis submitted in fulfillment of the requirements
for the degree of Doctor of Philosophy

in the

Space and Atmospheric Physics Group
Department of Physics

June 22, 2018

Declaration of Authorship

I, Amy SEALES, declare that this thesis titled, "Reducing uncertainty in climate prediction: enhancing the science case for TRUTHS" and the research presented in it are my own. I confirm that where I have quoted or consulted the work of others, this is fully acknowledged and attributed.

Copyright Declaration

The copyright of this thesis rests with the author and is made available under a Creative Commons Attribution Non-Commercial No Derivatives licence. Researchers are free to copy, distribute or transmit the thesis on the condition that they attribute it, that they do not use it for commercial purposes and that they do not alter, transform or build upon it. For any reuse or redistribution, researchers must make clear to others the licence terms of this work.

Abstract

The research in this thesis focuses on the ability of a proposed satellite mission, Traceable Radiometry Underpinning Terrestrial and Helio- Studies (TRUTHS), to detect signals of climate change as manifested in the Earth's reflected shortwave spectrum. TRUTHS aims to measure the total incoming solar irradiance, spectral solar irradiance and Earth's reflected shortwave radiation with sufficient radiometric accuracy to enable rapid detection of signals of climate change above natural variability. Early detection of such signals will potentially enable mitigation strategies to be employed faster.

Initially, sensitivity studies were conducted to investigate the atmospheric and surface variables that affect reflected shortwave spectra. TOA shortwave reflectances calculated from Climate Observation System Simulation Experiment (COSSE) data were then used to investigate how quickly changes could be detected above natural variability, as manifested in the simulations, using a linear regression model. The shortest detection times ranged from 7-15 years and 10-25 years under clear and all sky conditions respectively. The impact of spatial resolution was investigated by comparing 10° and 1.41° zonal average data. The 10° data provided 9.2% more detections at <20 years for all sky conditions than the high resolution data. The data were also separated into land and ocean to investigate the effect of surface type, however this in general yielded no clear improvement in detection times.

Finally, gaps were added to the data record to simulate realistic climate observation scenarios. These gaps varied from 10 to 25 years, with records lengths of 3 or 5 years based on the estimated lifetime of a TRUTHS mission. Detection times indicate that, of the scenarios investigated, a repeating 5 year mission followed by a 10 year gap is optimal, providing detection times of predominantly <20 years globally at 1600nm, 1680nm and 2190nm, and in the tropics at visible wavelengths.

Acknowledgements

Thank you, of course, to Helen for all of your supervision and many hours of discussion and help. Thank you to Paul for your help and to NPL for having me - I thoroughly enjoyed my time in Teddington. And finally, big thanks to Rich Bantges - you were my unofficial supervisor so thank you for coming to all of our meetings and for answering my (many) IDL questions.

To my wonderful friends, Ruth and Josh, who were my rocks. Our tea breaks were long and frequent (as were our holidays) but thanks to you guys I've had the best time at Imperial, and we all made it! And thank you to Alison for even more tea breaks and always lending an ear.

To my parents - you both gave so much to get me to where I am today and I will be eternally grateful, even though I'm too stubborn to say it. Apologies for being a nightmare to live with for the last couple of years.

And last but not least, thank you to Mark. I genuinely would not have gotten through the last couple of years without you and your unwavering love and support. We are the best team.

Contents

Declaration of Authorship **3**

Copyright Declaration **5**

Abstract **7**

Acknowledgements **9**

Contents **11**

List of Figures **15**

List of Tables **23**

List of Abbreviations **25**

1 Introduction **29**

1.1 Aims and Motivation 29

1.2 Background 30

1.2.1 Earth's Radiation Balance 30

1.2.2 Shortwave Radiation 32

1.2.3 ECVs and Climate Monitoring 36

1.2.4 TRUTHS 43

1.3 Thesis Outline 53

2 Data and Tools used in this Study **55**

2.1 Tools - Radiative Transfer Model 55

2.1.1 LibRadtran 56

2.2 Data 63

2.2.1 COSSE Data 64

3 Sensitivity Studies **71**

3.1 LibRadtran Sensitivity Studies 71

3.1.1 Method 72

3.1.2 Variables and Effects 73

SZA and Ozone 73

Aerosols 75

Albedo 78

Clouds 83

3.2 Polar Sensitivity Studies 89

3.2.1 Results 94

3.3 Water Vapour Sensitivity Study 98

3.3.1 Results 99

3.4 Summary 99

4 Time to detect **103**

4.1 Methods 103

4.1.1 Idealised case 107

4.2 Detection Time and Spatial Resolution 109

4.2.1 Noise Characterisation 110

Method and results 110

4.2.2 Resolution Comparisons 111

4.2.3 Summary and Inferences 123

4.3 Land-Ocean Comparisons 126

4.3.1 Global Detection Times 127

4.3.2 Land-Ocean Separation 133

4.3.3 Summary 138

5 Effect of data gaps on detection times **139**

5.1 Method 139

5.1.1 Idealised Time Series 148

5.2 Effect of Gaps in Climate Record 150

5.3 Effect of measurement uncertainty 162
5.4 Summary 167

6 Conclusions and Future Work **173**
6.1 Conclusions 173
6.2 Future Work 180

Bibliography **183**

List of Figures

1.1 Diagram showing the annual global energy balance calculated for a 4 year period (2000-2004). From Trenberth et al., (2008), ©American Meteorological Society. Used with permission. 31
1.2 Plot showing the incoming solar spectrum and irradiance at the surface. Certain absorption bands are identified. (Hoffmann, (2007)) 35
1.3 Plot showing the time series of the altitude of ERBS in kilometres above sea level. From Wong et al., (2005), ©American Meteorological Society. Used with permission. 41
1.4 Trend accuracy of cloud radiative forcing (CRF) against the time observing, with lines showing various calibration accuracies of current and future instruments, and a perfect observer (adapted from Fox, (2010)). . . . 45
1.5 Diagram of the inside of the TRUTHS satellite and placement of instrumentation. (Courtesy of Paul Green). 47

2.1 Flow chart of the inputs and outputs for uvspec in libRadtran. Variables T, P and ρ are temperature, pressure and gas densities respectively. Cloud variables τ and z are cloud optical depth and cloud height respectively. 58
2.2 Atmospheric constituent profiles for water vapour (left panel) and ozone (right panel) in the US Standard atmosphere. 59
2.3 Aerosol profiles for water soluble/insoluble components, and soot, for two OPAC defined aerosol types (desert and urban). Note the difference in the scales for the concentrations. 62
2.4 Evolution of CO_2 and SO_2 over time in the IPCC AR4 A2 emissions scenario. 65

2.5 The zonally and annually averaged values of the aerosol optical depth anomalies over time for the A2 scenario experiment data, with respect to the average AOD at 550nm for the period 2000-2009. 66
2.6 Zonally and annually averaged broadband clear sky albedo anomalies with respect to the average albedo for the period 2000-2009, at every 10° latitude band. The white contours highlight where the anomalies are zero. 69
2.7 Zonally and annually averaged spectrally resolved albedo anomalies at 20°N. The white contours highlight where the anomalies are zero. 69

3.1 TOA nadir reflectance spectrum for 'default' conditions - a US Standard Atmosphere, a uniform surface albedo of 0.25 and SZA of 30°. 73
3.2 a) TOA nadir reflectance spectra for US Standard atmosphere, with 100DU of ozone, b) the same as a) with 500DU of ozone, c) the 550DU reflectance minus the 100DU reflectance. Note the change in scale of the x-axis. . . 75
3.3 a) Difference between the TOA nadir reflectances for a pristine atmosphere, and the same atmosphere with urban aerosols over a surface of albedo 0.25, b) the same as (a) for desert aerosols. In both cases the pristine spectrum is subtracted from the polluted spectrum. 76
3.4 a) Difference between the TOA nadir reflectances for a pristine atmosphere, and the same atmosphere with urban aerosols over a surface of albedo 0.05, b) the same as (a) for desert aerosols. In both cases the pristine spectrum is subtracted from the polluted spectrum. Note the difference in the y-axis scales. 78
3.5 The surface albedo spectrum for a) a sand surface b) a grass surface, and c) an ocean surface. Note the different scales on each panel. 80
3.6 a) The TOA nadir reflectance spectrum for a sand surface b) the same as (a) for a grass surface, and c) the same as (a) for an ocean surface. Note the different reflectance scales on each panel. 82

3.7 a) Difference in TOA reflectance spectra between an atmosphere with a water cloud at 2-3km and 2-4km (2km thickness - 1km thickness), b) difference in TOA reflectance spectra between an atmosphere with a water cloud at 2-3km and 3-4km (3-4km cloud - 2-3km cloud). Note the difference in the scales. 84
3.8 Difference in TOA nadir reflectance between clouds with droplet radii 10 and 15 microns (15 - 10 μm). 85
3.9 a) Difference in TOA nadir reflectance between an ice cloud at 10-11km and 10-12km (2km cloud - 1km cloud), b) and the difference in TOA nadir reflectance between an ice cloud at 10-11km and 11-12km (11-12km cloud - 10-11km cloud). 86
3.10 Difference in TOA nadir reflectance between ice clouds with R_{eff} 20 microns and 25 microns (25 - 20 microns). 88
3.11 TOA nadir reflectance spectra for an atmosphere with a water cloud (red line) and with an ice cloud (blue line). 89
3.12 Variation of albedo with wavelengths 0.2-2.8μm on a snow covered surface, and with SZA. From (Wiscombe and Warren, (1980)), ©American Meteorological Society. Used with permission. 91
3.13 Global top of atmosphere reflectance maps at 1.41°x1.41° resolution, based on the COSSE data from Feldman et al., (2011)(b), for each wavelength. The Arctic region is considered to comprise of latitudes of 66°N and above. a) shows the map for 550nm, b) the map for 940nm and c) the map for 2190nm. Note the difference in scale between panels. 93
3.14 Flux profiles from 5km altitude to the surface for 550nm. a) SZA 40°, τ = 2, α = 0.5. b) is for the same case at α 0.9. Each line shows how the direct downwelling, diffuse downwelling and diffuse upwelling fluxes change with altitude above and below a cloud layer at 1-2km. 95

3.15 Schematic of the interactions between the radiation, the cloud and the surface for the cloud with τ=2, at 550nm, 40° SZA, and α = 0.5. Values from corresponding simulation. A. Direct downwards irradiance at cloud top, B. Direct downwards irradiance at surface, C. Diffuse downwards irradiance at surface, D. Diffuse upwards irradiance at surface, E. Diffuse upwards irradiance at cloud top. 97

3.16 Schematic showing the interactions between the radiation, the cloud and the surface for an optically thicker cloud (τ=8 case), at 550nm, 40° SZA, and α = 0.5. Values from corresponding simulation. Arrow labels as before; note there is no direct downwards irradiance at the surface in this case. 98

3.17 TOA nadir reflectances at 940nm over land and ocean surfaces, for increasing atmospheric water vapour. 100

4.1 Correlogram of the noise in all sky spectral reflectance at 550nm, for a 1.41° zonal mean band centred at 25°N. The autocorrelation falls to within the significance boundaries shown by the dotted lines after a lag of 1 year. 105

4.2 Detection time values from Equation 4.3 107

4.3 a) Noise for 550nm at each latitude band for the time period 100 years for clear sky conditions, b) the same for all sky conditions, c) white noise under clear sky conditions, d) the lag 1 autocorrelation for 100 years under clear and all sky conditions. All at 1.41°. 112

4.4 Zonally and annually averaged nadir reflectance anomalies for 10° latitude bands at 550nm, with respect to the average reflectance for the time period 2000-2009, under clear sky conditions. The black line indicates the time to detect; the white contours indicate zero anomaly. 115

4.5 Zonally and annually averaged nadir reflectance anomalies for 10° latitude bands at 550nm, with respect to the average reflectance for the time period 2000-2009, under all sky conditions. The black line indicates the time to detect; the white contours indicate zero anomaly. 115

4.6 Zonally and annually averaged nadir reflectance anomalies for 1.4° latitude bands at 550nm, with respect to the average reflectance for the time period 2000-2009, under clear sky conditions. The black line indicates the time to detect; the white contours indicate zero anomaly. 116
4.7 Zonally and annually averaged nadir reflectance anomalies for 1.4° latitude bands at 550nm, with respect to the average reflectance for the time period 2000-2009, under all sky conditions. The black line indicates the time to detect; the white contours indicate zero anomaly. 116
4.8 Detection times at 550nm clear sky for 1.4°, 10°, and the 1.4° data averaged into 10° latitude bands. 119
4.9 Detection times at 550nm all sky for 1.4°, 10°, and the 1.4° data averaged into 10° latitude bands 119
4.10 Time to detect for each latitude band, for every wavelength (300-2500nm). (a) 1.41° latitude bands, clear sky conditions, (b) 1.41° latitude bands, all sky conditions, (c) 10° latitude bands, clear sky conditions, (d) 10° latitude bands,all sky conditions. 122
4.11 a) Number of wavelengths which have a time to detection for the spectral nadir reflectance less than 10 years, for each latitude band, for clear sky conditions. The green bars show the values for the 1.4° latitude band data, while the black line shows the same values for the 10° latitude bands; b) same information for the all sky case; c) same information for clear sky case but with a condition of 20 years, and d) as (c) for all sky. 124
4.12 Map of the detection times at 2190nm, under clear sky conditions 129
4.13 Map of the detection times at 2190nm, under all sky conditions 129
4.14 Map of detection times at 940nm, under clear sky conditions 132
4.15 Map of detection times at 940nm, under all sky conditions 132
4.16 Land mask used for land-ocean separation 133
4.17 Time to detect over land under clear sky conditions for each wavelength and each 1.41° latitude band. 135
4.18 Time to detect over ocean under clear sky conditions for each wavelength and each 1.41° latitude band. 135

4.19 Time to detect over land under all sky conditions for each wavelength and each 1.41° latitude band. 137
4.20 Time to detect over ocean under all sky conditions for each wavelength and each 1.41° latitude band. 137

5.1 a) Detection times at each latitude band for 8 selected wavelengths under clear sky conditions, using the linear regression model, b) the corresponding detection times from Chapter 4, c) the difference in the detection times between the two methods (linear regression times minus original times). 144
5.2 a) Detection times at each latitude band for 8 selected wavelengths under all sky conditions, using the linear regression model, b) the corresponding detection times from Chapter 4, c) the difference in the detection times between the two methods (linear regression times minus original times). 145
5.3 a) TOA reflectance at 660nm for the 50-60°N latitude band under clear sky conditions. Red line denotes 26 year detection time, black line denotes the 57 year detection time. b) noise time series until the respective detection times using the original method and the linear regression method. The black line represents the linear regression model, and the red line represents the original method. 147
5.4 a) Detection times using 3 year periods of data, for each latitude band and wavelength under clear sky conditions. b) The same as a) using 5 year periods of data. Each wavelength band comprises of 4 detection times signifying the detection time for increasing gap length; 10, 15, 20 and 25 years respectively. Black areas represent no detection within 100 year record. 152

5.5 a) TOA reflectance under clear sky conditions at 1600nm for the 0-10°N latitude band. The grey panels show the 20 year gaps between 3 year periods of data and therefore the data points that are not used in calculations. The blue, green and red data points represent the points used with 10, 15 and 25 year gaps respectively, and are offset for clarity. b) the trend, standard deviation of the white noise, and the main body of Equation 4.3 at each data point for a 20 year gap. 154

5.6 a) TOA reflectance under clear sky conditions at 660nm for the 60-70°S latitude band. The grey panels show the 20 year gaps between 3 year periods of data and therefore the data points that are not used in calculations. The blue, green and red data points represent the points used with 10, 15 and 25 year gaps respectively, and are offset for clarity. b) the trend, standard deviation of the white noise, and the main body of Equation 4.3 at each data point. 157

5.7 a) Detection times using 3 year periods of data, for each latitude band and wavelength under all sky conditions. b) The same as a) using 5 year periods of data. Each wavelength band comprises of 4 detection times signifying the detection time for increasing gap length; 10, 15, 20 and 25 years respectively. Black areas represent no detection within 100 year record. 159

5.8 a) TOA reflectance for 0-10°N at 1600nm using 3 year data sets, with grey panels representing 15 year gaps, b) the same as (a) using 5 year data sets. 161

5.9 a) The detection times under all sky conditions for the continuous data set, b) the same as (a) accounting for measurement uncertainty. 164

5.10 a) The detection times under all sky conditions for 5 year data sets and 10 year gaps, b) the same as (a) accounting for measurement uncertainty. 166

5.11 The number of wavelengths per latitude band with a detection time of less than 30 years using the continuous data set (blue) or using 5 year records with a 10 year gap (green) under all sky conditions. 169

List of Tables

2.1 Composition of all aerosol types from OPAC; number density, N in cm^{-3}, and mass density, M in μgm^{-3}. Adapted from Hess et al., (1998). Table does not include all components of the aerosols. 61

3.1 Values of SZA, cloud optical depth at 550nm, and surface albedo used in simulations 90
3.2 The values of the single scattering albedo and asymmetry parameter of the cloud input into the atmosphere in libRadtran 92

4.1 Detection times for varying trends for an artificial time series. 108
4.2 Detection times for varying magnitudes of standard deviation of the white noise for an artificial timeseries. 109
4.3 Detection times for varying autocorrelations of the noise for an artificial timeseries. 109
4.4 Number of wavelengths with detectable signal for 1.4° and 10° latitude bands 126

5.1 Detection times for varying trends for an artificial time series. 149
5.2 Detection times for varying magnitudes of standard deviation of the white noise for an artificial timeseries. 149
5.3 Detection times for varying autocorrelations of the noise for an artificial timeseries. 150

List of Abbreviations

AERONET-OC	**Aero**sol **Ro**botic **Net**work - **O**cean **C**olour
AMOC	**A**tlantic **M**eridional **O**verturning **C**irculation
AOD	**A**erosol **O**ptical **D**epth
AR(1)	First-order **A**uto**r**egressive process
BRDF	**B**idirectional **R**eflectance **D**istribution **F**unction
BSRN	**B**aseline **S**urface **R**adiation **N**etwork
CCI	**C**limate **C**hange **I**nitiative
CCSM	**C**ommunity **C**limate **S**ystem **M**odel
CEOS	**C**ommittee on **E**arth observation **S**atellites
CERES	**C**loud and the **E**arth's **R**adiant **E**nergy **S**ystem
CLARREO	**C**limate **A**bsolute **R**adiance and **Re**fractivity **O**bservatory
COSSE	**C**limate **O**bservation **S**ystem **S**imulation **E**xperiment
CRE	**C**loud **R**adiative **E**ffect
CRF	**C**loud **R**adiative **F**orcing
CSAR	**C**ryogenic **S**olar **A**bsolute **R**adiometer
DISORT	**Dis**crete **O**rdinate Method molecular **R**adiative **T**ransfer
ECV	**E**ssential **C**limate **V**ariable
EO	**E**arth **O**bservation
ERB	**E**arth **R**adiation **B**udget
ERS	**E**urpoean **R**emote Sensing **S**atellite
ERBE	**E**arth **R**adiation **B**udget **E**xperiment
GCOS	**G**lobal **C**limate **O**bserving **S**ystem
GERB	**G**eostationary **E**arth **R**adiation **B**udget
GNSS-RO	**G**lobal **N**avigation **S**atellite **S**ystem - **R**adio **O**cculation
GOME	**G**lobal **O**zone **M**onitoring **E**xperiment

HITRAN	**H**igh resolution **Tran**smission molecular absorption
IPCC	**I**ntergovernmental **P**anel for **C**limate **C**hange
IR	**I**nfra**r**ed
IWC	**I**ce **W**ater **C**ontent
LBLRTM	**L**ine **B**y **L**ine **R**adiative **T**ransfer **M**odel
LWC	**L**iquid **W**ater **C**ontent
MODIS	**Mod**erate resolution **I**maging **S**pectrometer
MODTRAN	**Mod**erate resolution atmospheric **T**ransmission
MSI	**M**ulti **S**pectral **I**mager
NAO	**N**orth **A**tlantic **O**scillation
NIR	**N**ear **I**nfra**r**ed
NPL	**N**ational **P**hysical **L**aboratory
NRC	**N**ational **R**esearch **C**ouncil
OPAC	**O**ptical **P**roperties of **A**erosols and **C**louds
OSSE	**O**bservation **S**ystem **S**imulation **E**xperiment
RTE	**R**adiative **T**ransfer **E**quation
PDO	**P**acific **D**ecadal **O**scillation
QBO	**Q**uasi **B**iennial **O**scillation
SBUV	**S**olar **B**ackscatter **U**ltra**v**iolet
SCIAMACHY	**Sc**anning **I**mage **A**bsorption spectro**m**eter for **A**tmospheric **CH**artograph**Y**
SI	**I**nternational **S**ystem of units
SSA	**S**ingle **S**cattering **A**lbedo
SSI	**S**olar **S**pectral **I**rradiance
SW	**S**hort**w**ave
SWIR	**S**hort**w**ave **I**nfra**r**ed
SZA	**S**olar **Z**enith **A**ngle
TIROS	**T**elevision **I**nfrared **O**bservation **S**atellite
TOA	**T**op **O**f **A**tmosphere
TRUTHS	**T**raceable **R**adiometry **U**nderpinning **T**errestrial **H**elio **S**tudies
TSI	**T**otal **S**olar **I**rradiance
UNEP	**U**nited **N**ations **E**nvironment **P**rogramme

UNFCCC	**U**nited **N**ations **F**ramework **C**onvention for **C**limate **C**hange
UV	**U**ltra**v**iolet
WFOV	**W**ide **F**ield **O**f **V**iew
WRMC	**W**orld **R**adiation **M**onitoring **C**entre

Chapter 1

Introduction

1.1 Aims and Motivation

The fundamental aim of this project is to investigate how the TRUTHS satellite (Traceable Radiometry Underpinning Terrestrial and Helio Studies) would perform, and aid in optimising the design of TRUTHS. In order to assist with this brief, the focus of this study is on the ability of TRUTHS to detect a signal of climate change above the natural variability of the climate system by looking at the spectral range and spatial resolution. The way in which this will be investigated is by calculating the time it would take to detect a signal of climate change above the natural variability in a set of simulated data for the planned spectral range of TRUTHS. The spectral and latitude dependence of the time to detect is then investigated to answer the questions; are there specific wavelengths at which the time to detect a signal is quicker? Similarly, are there latitudes at which a robust signal of climate change emerges faster? These analyses are carried out at two different spatial resolutions in order to investigate the effect of resolution on the time to detection. All of the above can be used to assist in the final design of TRUTHS. Also, as previously discussed, the standard lifetime of a satellite instrument is 5 years (Wielicki et al., (2013)) and therefore it is highly likely that there will be gaps in any climate record. Therefore it is of great interest to understand how these gaps would affect the ability of TRUTHS to confidently detect this signal and this is one of the questions that needs to be answered. Once this has been understood, it is possible to then gauge how many TRUTHS-like satellites would be required, and in

what time frame, in order to still detect these signals and this can then be factored in to the design and planning of TRUTHS.

1.2 Background

1.2.1 Earth's Radiation Balance

Earth's Radiation Budget (ERB) is the balance between the incoming solar radiation and the outgoing radiation at the top of the atmosphere (TOA). The outgoing radiation is composed of two parts; the reflected solar radiation and the outgoing long-wave radiation that is emitted by the Earth itself. The global annual mean of the incident solar flux at the top of the atmosphere is approximately 341Wm^{-2}, and is shown in Figure 1.1, which describes the annual energy budget averaged over a four year period from March 2000 until May 2004. Around 23% of the incoming solar flux is absorbed by the atmosphere itself and another 23% is reflected by the atmosphere and clouds. This means that only 54% of the incoming solar radiation makes it to the surface. When at the surface, 161Wm^{-2} is absorbed by the surface, which corresponds to approximately 47% of the original solar radiation, and the remaining 23Wm^{-2} is reflected back to TOA. The ERB is calculated at the top of the atmosphere however there are other radiative processes occurring at various levels in the atmosphere which contribute to the global energy budget. These processes that influence the transfer of radiation within the atmosphere are absorption by the Earth's surface and atmosphere for both short-wave and long-wave radiation, reflection and emission by the atmosphere and surface and any absorption or scattering by aerosols and clouds.

The energy balance at TOA can be described by Equation 1.1 from Roberts et al., (2011), where F is the net irradiance. If there is a radiative equilibrium, F is equal to zero and the two terms on the right hand side of Equation 1.1 (incoming solar radiation and emitted infrared radiation respectively) are equal.

$$F = (1 - \alpha)\frac{S_0}{4} - \sigma_B T_E^4 \tag{1.1}$$

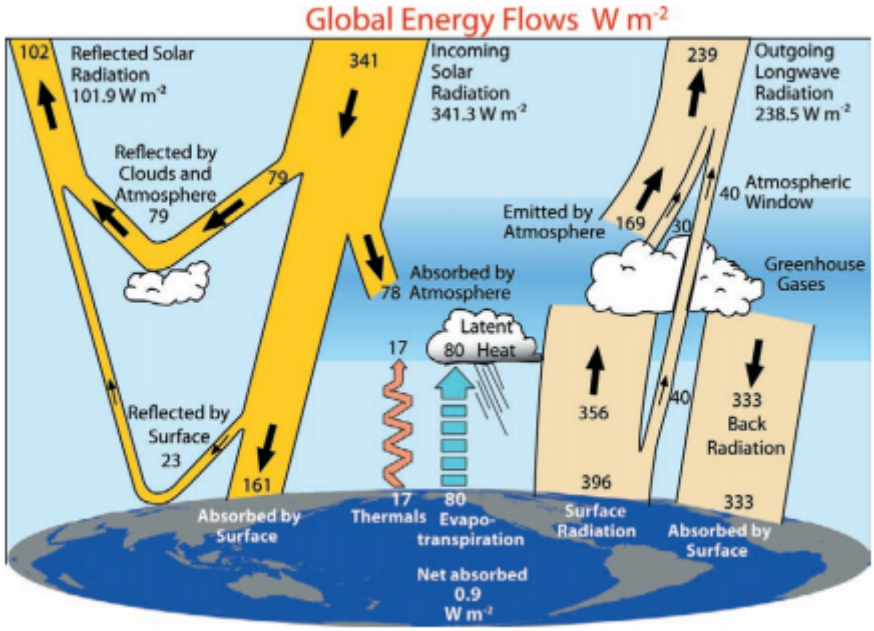


FIGURE 1.1: Diagram showing the annual global energy balance calculated for a 4 year period (2000-2004). From Trenberth et al., (2008), ©American Meteorological Society. Used with permission.

In this equation, albedo is given by α. Albedo is defined in Liou, (2002) as the ratio between the amount of flux reflected back into space and the incoming solar flux, and effectively describes the reflectivity of the Earth. Therefore, (1-α) is a measure of the amount of flux that is absorbed by the Earth. Sigma, σ_B, is the Stefan Boltzmann constant and T_E is the effective emission temperature of the Earth. S_0 is the solar constant which is taken to be 1370Wm^{-2} in Klassen and Bugbee, (2005), though different sources provide different values since the 'solar constant' is not truly constant. Therefore, $S_0/4$ is the average incident solar irradiance. Performing this calculation provides an average solar irradiance of 342.5Wm^{-2} which is clearly larger than the value stated in Figure 1.1. This is due to the variability of the solar constant and uncertainties associated with its measurement, since different instruments provide different values. Haigh, (2011) discusses the the two primary sources of this variability - the solar activity, and the changes in Earth's orbit around the sun. Solar activity is measured using several 'indicators', which include the total solar irradiance (TSI), cosmic ray neutron count, incidence of aurorae and the sunspot number which is the most well known (Haigh, (2011)). Sunspot numbers are shown to obey an 11 year cycle and there is data available for several centuries which show the variation in solar activity. Secondly, there is variation in the Earth's orbit, however these changes occur over much

longer timescales. These changes are referred to as the Milankovich cycles and affect the eccentricity of the Earth's orbit, the tilt of the Earth and its precession, and occur on timescales of over 100,000 years, 41,000 years and 26,000 years respectively (Haigh, (2011)). These three parameters change the amount of solar radiation that reaches the Earth, which would be expected to affect the climate. However, the extent to which the variability of sun affects Earth's climate is regularly debated and controversial (Haigh, (2003)). Therefore it is important that quantities such as the TSI are measured as accurately as possible, to know the exact value of the incoming solar radiation.

If the net irradiance at TOA is not zero, the Earth's energy budget is no longer balanced and even a slight discrepancy between the two terms in Equation 1.1 would mean either extra energy has been trapped within Earth's system causing net heating, or there has been a net loss of energy causing the system to cool down. Trenberth et al., (2008) show that for the period of 2000-2004 there was a net absorption of 0.9Wm^{-2} per year (Figure 1.1). The observed Earth energy imbalance consists of several terms - ocean contributions and non-ocean contributions which separate out into atmosphere, land and ice (Hansen et al., (2011)). In Hansen et al., (2011), the energy imbalance is calculated for the later period of 2005-2010 which reveals a net absorption of 0.58Wm^{-2}. This can be separated into the above contributions, with ocean displaying a heat gain of 0.51Wm^{-2} overall, and 0.071Wm^{-2} for non-ocean. These values for the energy imbalance are small, and it is not currently possible to measure the ERB with sufficient accuracy in order to identify these small changes and whether they are the result of natural variability or due to climate change.

The focus of this work will be on shortwave radiation; both the direct shortwave radiation received from the Sun and the Earth reflected shortwave radiation.

1.2.2 Shortwave Radiation

The shortwave radiation incident at TOA from the Sun is affected by several processes as it travels through the atmosphere. As previously discussed, Figure 1.1 shows that a

certain amount of the radiation will be absorbed and scattered by aerosols in the atmosphere, a certain amount will be reflected and scattered by clouds and the atmosphere, and the remaining radiation will be transmitted directly to the surface of the Earth. Transmissivity is defined in Wallace and Hobbs, (2006) as the ratio between the transmitted to incident radiation and is a function of wavelength. The Beer-Lambert law states that the transmissivity decreases exponentially with increasing optical depth, as shown in Equation 1.2 (Wallace and Hobbs, (2006)). Transmissivity is dimensionless and varies between zero and one, e.g. a transmissivity of zero indicates that the medium is totally opaque at a given wavelength, whereas a transmissivity of 1 indicates the medium is transparent at that wavelength.

$$T_\lambda = e^{-\tau_\lambda} \tag{1.2}$$

Optical depth, τ_λ, is a measure of how much a direct beam of radiation would be attenuated when travelling through a layer and is wavelength dependent. From Liou, (2002), optical depth is dependent on the mass density, ρ, of the medium through which the beam is travelling, the mass extinction coefficient, k_λ (units $\mathrm{m^2 kg^{-1}}$), and the thickness of the layer, dz. This is integrated over the layer (Equation 1.3).

$$\tau_\lambda = \int_{z_1}^{z_2} k_\lambda \rho \, dz \tag{1.3}$$

The attenuation of a beam of radiation is known as extinction and can be down to two processes – scattering and absorption. As with the extinction coefficient, there are also coefficients related to scattering and absorption separately. The relationship between these coefficients is shown in Equation 1.4 where the extinction coefficient is simply the sum of the scattering and absorption coefficients.

$$k_{\lambda,extinction} = k_{\lambda,scattering} + k_{\lambda,absorption} \tag{1.4}$$

Scattering occurs in the atmosphere due to cloud droplets, ice crystals, molecules and aerosol particles and is dependent on the composition, shape and size of the scatterers.

Different scattering regimes occur as a consequence of a change in the ratio between the wavelength of incident radiation and the size of the scattering particle, or the so-called size parameter, x, where;

$$x = \frac{2\pi r}{\lambda} \tag{1.5}$$

Typically, Rayleigh scatter (proportional to $1/\lambda^4$) occurs when x«1, so becomes more important for molecular scatter at visible wavelengths. At intermediate values of x, i.e. 0.1<x<50 (Wallace and Hobbs, (2006)), Mie scattering becomes dominant, assuming the particles are spherical.

The relationship between scattering and absorption is often expressed as the single scattering albedo (SSA) which measures the relative importance of scattering and is the ratio between the scattering and extinction coefficients. For a non-absorbing material, the SSA is 1, while a strong absorber is categorised as having a SSA <0.5. (Wallace and Hobbs, (2006)).

There are other parameters that affect the ability of a particle, molecule or droplet to scatter or absorb radiation. The asymmetry parameter states how much of the incident radiation is forward scattered or back scattered. The parameter, g, varies between -1 which signifies all radiation is back scattered, and +1 which means all radiation is forward scattered, with 0 showing radiation is isotropically scattered. There is also the phase function which is the angular distribution of the scattered radiation. The phase function is typically given as a function of scattering angle, which is the angle of the scattered beam relative to the angle of the incident radiation. It fundamentally shows the likelihood that the incident radiation will be scattered at a certain angle. Both the asymmetry parameter and phase function are functions of wavelength.

These processes that affect the incoming radiation can be seen in the spectra of the radiation that can be measured at the surface or TOA. Figure 1.2 demonstrates the difference between the TOA incoming solar spectrum and a shortwave spectrum at the surface and the typical way in which changes to the radiation manifest themselves.

The troughs in the spectrum are due to absorption from the labelled species such as water vapour and ozone. Any scattering of the radiation doesn't cause troughs but will change the distribution of the radiation.

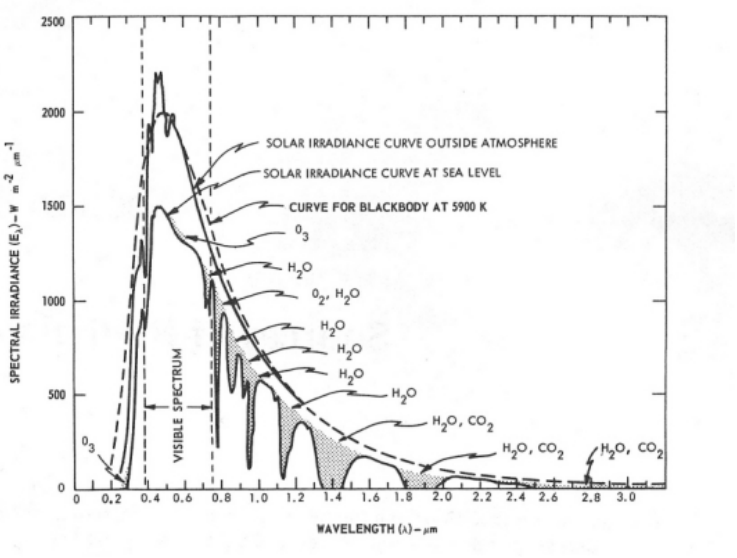


FIGURE 1.2: Plot showing the incoming solar spectrum and irradiance at the surface. Certain absorption bands are identified. (Hoffmann, (2007))

Absorption occurs at specific, well-known wavelengths depending on what the absorbed material is composed of. For example, it can be seen in Figure 1.2 that at wavelengths less than 700nm the absorption can be attributed to ozone molecules. Since these absorption bands occur at the same wavelengths consistently, using spectral data it is possible to attribute absorption bands and features to certain aerosol or gas species, and changes in the amounts or locations of these species will have a certain spectral signature. It is also possible to determine the amount and heights of clouds and aerosols as these particles also affect the measured radiation at TOA or the surface. An example of this is given by Bovensmann et al., (1999). Here, the method of how it is possible to invert measurements of radiance and irradiance to then calculate the amounts or various atmospheric constituents from a spectrum such as the one in Figure 1.2 is explained. This approach was used on data obtained by the SCIAMACHY instruments (SCanning Imaging Absorption spectroMeter for Atmospheric CHartographY) on board the European Space Agency's (ESA) Envisat satellite in a bid to quantify various constituents (such as O_3, O_2, CO_2, NO_2, H_2O, CH_4 etc. (Bovensmann et al., (1999))) and their vertical distributions.

This example from Bovensmann et al., (1999) shows that it is possible to gain valuable information about the composition of the atmosphere, the concentrations of constituents and their distributions, all from the spectrum of the ultraviolet to near-infrared (UV-NIR) radiation (240-2380nm range) reflected, transmitted and scattered by the atmosphere and surface. Not only this, but it is possible to gain knowledge about the surface albedo and temperature, cloud cover and height in the atmosphere (Bovensmann et al., (1999)).

Another example is the Global Ozone Monitoring Experiment (GOME) which was an instrument used on the Second European Remote Sensing Satellite (ERS-2). Its purpose was to measure the sunlight scattered by the Earth's atmosphere and reflected by the surface in order to calculate the global distribution of ozone (Burrows et al., (1999)). GOME was also able to provide information such as trace column amounts for other trace gases such as SO_2, NO_2 and NO_3. Prior to this, ozone profiles were derived from data collected from NASA's Solar Backscatter Ultraviolet (SBUV) experiment upon the Nimbus 7 satellite and subsequent instruments. The combination of the data records from these experiments allowed a 16 year global ozone profile record (Bhartia et al., (1996)).

Measuring the spectrally resolved radiances from Earth can provide insight into all of these variables. These are the kind of fundamental parameters that enable a better understanding of the Earth system and climate, and monitoring these would provide an understanding on how they and the climate are evolving over time, possibly attributing climate change to changes in these variables. GCOS (Global Climate Observing System) have compiled a list of variables such as these and designated them as Essential Climate Variables (ECVs) and these will be discussed in the next section.

1.2.3 ECVs and Climate Monitoring

An ECV is defined in Bojinski et al., (2014) as *'a physical, chemical, or biological variable or a group of linked variables that critically contributes to the characterisation of Earth's climate'* and was first described in a report by GCOS, (2003). There are 50 ECVs set

out by GCOS that cover three main Earth domains; atmospheric, oceanic and terrestrial which are listed in GCOS, (2011) as well as in other papers such as Bojinski et al., (2014). These were selected as variables that are both economically and technologically viable to observe and are used to advise the United Nations Framework Convention for Climate Change (UNFCCC) and the Intergovernmental Panel for Climate Change (IPCC). Examples of the ECVs specified include land and sea surface temperatures, land use, ocean colour, snow cover and albedo. However, it has been said that within the atmosphere there are critical climate variables such as temperature, water vapour, carbon dioxide concentrations, cloud and aerosols, and winds (Brindley and Russell, (2013)). ERB is one of the fundamental ECVs since the climate is driven by incoming solar radiation. The reflected TOA radiation can provide information about the climate and its evolution. For example, as previously mentioned, the SCIAMACHY instrument has been used to identify the atmospheric composition (Bovensmann et al., (1999)), and also measure changes in the climate using the shortwave Earth reflected radiance (Roberts et al., (2011)).

All ECVs (excluding the ERB) can't be measured directly and so are derived from fundamental measurements of radiance and reflectance. Fox et al., (2011) discuss the accuracy requirements needed for measurements of radiance and irradiances in order to produce climate quality ECVs. They suggest the following;

- Total Solar Irradiance (TSI) 0.01%
- Solar Spectral Irradiance (SSI) 0.1%
- Earth reflected solar radiance 0.3%
- Earth emitted IR radiances 0.1K

Fox et al., (2011) also note that it is expected that the temperature of the Earth will rise by approximately 0.2K per decade. However, currently there are no existing sensors that have the accuracy required to detect a 0.2K per decade change.

There are many methods by which to measure various aspects of the climate, for example radiosondes, ground based networks such as the Baseline Surface Radiation

Network (BSRN) run by the World Radiation Monitoring Centre (WRMC) (Ohmura et al., (1998)), and active and passive satellite sensors. One of the main benefits for using satellites for monitoring climate, as discussed in Hollmann et al., (2013), is that they are able to observe on a global scale. Measurements made using radiosondes or buoys provide detailed observations in their locality, but obtaining global coverage would require vast numbers of these which would be prohibitively expensive. The ability to observe climate globally is useful not only for monitoring climate, but to also assist in modelling of climate and in Earth System models. This enables the modelling community to better represent the climate, in order to improve short term forecasting capabilities and enable the attribution of climate change to various processes and changes (Hollmann et al., (2013)).

There are various international treaties in place to deal with climate change such as the Kyoto Protocol (UNFCCC, (1998)) and Montreal Protocol (UNEP, (1987)), as well as the IPCC which was put together to advise governments on climate change. These various efforts to advise and mitigate climate change over the last few decades show the urgent need to better the current understanding of climate.

Observing climate from space has a history that dates back to 1960 when the Television Infrared Observation Satellite (TIROS-1) was launched by NASA and became the first successful low Earth orbit weather satellite. The instrumentation on this satellite was limited to two television cameras (one high and one low resolution) which took still images that were transmitted back to Earth (Vaughn and Johnson, (1994), Neeck et al., (2005)). TIROS-1 began a series of satellite missions by NASA that are still continuing at present but under different guises, having lost the TIROS name. TIROS-N in 1978, detailed in Schwalb, (1978), is considered as the beginning of global EO via satellite as it was making measurements that could be used in global weather forecasting. This means, however, that there is only Earth Observation data available for the last 35 years. The IPCC considers climate on a 30 year timescale which means that using all data records since TIROS-N only matches and doesn't exceed the lower limit of timescale required to measure climate. Now there is a priority to obtain long-term measurements in order to detect global changes in climate, or begin to reduce the

amount of time it takes to detect such trends. For example, the Climate Change Initiative (CCI) was started in response to the call by GCOS for measurements of ECVs, and the aforementioned requirement for long-term measurements. The CCI was started by ESA and its member states, to provide Earth Observation (EO) records from the past 30 years to contribute to the ECV databases (Bojinski and Fellous, (2013)).

Ohring and Gruber, (2001) note that the decadal variations in climate signals are much smaller than the interannual variability and so being able to detect these changes is an issue that needs to be resolved. This interannual variability is due to phenomena such as El Niño and La Niña, and the North Atlantic Oscillation (NAO) which affect the Earth System as a whole via ocean-atmosphere interactions. These effects, along with volcanic eruptions and the solar cycle are considered in Liu et al., (2017) as the major factors of natural variability. There are, of course, other contributors such as the Pacific Decadal Oscillation (PDO) and the Atlantic Meridional Overturning Circulation (AMOC) (Liu et al., (2017)).

Another issue with a significant amount of the data that has been obtained from EO satellites is that they have been for weather forecasting, and not for climate studies. When forecasting weather, the focus is getting precise, detailed measurements over short timescales (Fox et al., (2011)). For climate studies data are required over long time periods and need to be very accurate in order to detect the small changes that are occurring over the large timescales (Ohring and Gruber, (2001)). The more accurately these variables and the way they are evolving over time can be observed, the sooner it is statistically possible to detect trends above the natural variability of the climate and policy can be enforced to try to counteract these changes. Hollmann et al., (2013) mention that the list of ECVs have been specified such that they will provide the right information in order to monitor the climate over sufficiently long timescales and to gauge the state of the global climate system.

There are various other issues with satellite observations, such as the fact that the launch of the satellite will cause vibrations that disrupt the pre-flight calibrations and

also that space is generally a very harsh environment. Therefore an on-board calibration system is required to calibrate the sensors once the satellite is in orbit. Another issue with EO satellites is that the standard lifetime for an instrument in orbit is approximately 5 years (Wielicki et al., (2013)). This means that in order to get long term records, time series are overlapped, inter-calibrated using the overlapping points and 'stitched' together to create one long data record. One problem with merging the datasets from various sensors is that when there are gaps in the data, the record is effectively ruined. It is also known that the satellite will drift in its orbit over the mission lifetime, but it is difficult to calculate by how much and correct the data for this.

There is a well-known example of this which is discussed in Wong et al., (2005). This paper was a re-examination of the same data used in a previous paper by Wielicki et al., (2002). Having studied data recorded from the Earth Radiation Budget Experiment (ERBE) Nonscanner Wide Field of View (WFOV) instrument, Scanner for Radiation Budget (ScaRaB) instrument, Cloud and the Earth's Radiant Energy System (CERES) scanner and others, a time-series of 22 years of satellite observed broadband radiative fluxes was created. With this time series, it was shown that there were large decadal changes in ERB in the tropical region (20N-20S). These were believed to be interesting results since the variation at TOA was previously assumed to be fairly small, but the analysis of their data showed large variations that Wielicki et al., (2002) attributed to changes in mean cloudiness. However, three years later during re-analysis of the datasets, it was discovered by Wong et al., (2005) that there was in fact a 'small but significant' drift in the altitude of the ERBS (ERB Satellite) over the 15 years of observations. It can be seen in Figure 1.3 that the altitude drifted by 26km between 1985 and 1999. Because the viewer was observing the entire Earth, the radiation incident on the scanner obeyed the inverse square law – meaning the amount received was affected by the distance between the Earth and the scanner; the decrease in altitude of the satellite made it appear that there was an increase in the TOA shortwave radiative flux.

There have been several efforts to address these types of issues. Weatherhead et al., (2017) states that the challenge is to provide stable and well calibrated climate records, however satellites and instruments are vulnerable to degradation and other effects

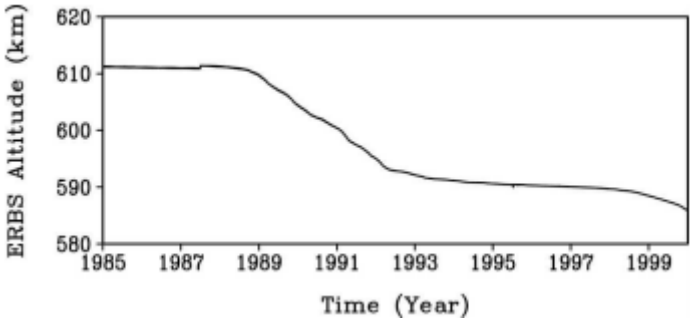


FIGURE 1.3: Plot showing the time series of the altitude of ERBS in kilometres above sea level. From Wong et al., (2005), ©American Meteorological Society. Used with permission.

which lead to the aforementioned jumps and drifts in the data sets. This is amplified by the fact that the data records from different instruments are used since the lifetimes of most instruments is relatively short compared to the timescales on which climate change in considered. It is concluded in Weatherhead et al., (2017) that one aspect that is controllable is to have overlap between instruments. While focussing on one wavelength, 280nm, Weatherhead et al., (2017) showed that an overlap of 5 months was required for 1% uncertainty in the estimation of the drift between two different instruments.

However, while it may be possible to have overlap between different instruments, it is more likely that there will be gaps or jumps in the data records. Loeb et al., (2009) investigated the effect of gaps in a data record on the error in trend estimation. This work used 30 year simulated fluxes from 5 years of CERES Terra data and examined the trend in the cloud radiative effect (CRE). The findings from these experiments found that the error in trend estimation was highly sensitive to where the gap occurs in the record; that the earlier the gap, the lower the error in the trend estimation. The conclusion by Loeb et al., (2009) is that a gap essentially restarts the record from zero and that while space-based calibration is not available, overlap between missions is necessary. Similar findings were shown in previous work by Weatherhead et al., (1998), where it was concluded that a jump in a data set would increase the time it would take to statistically detect a trend in a signal by 50%.

It has now been recognised that all EO data needs to be traceable to an agreed reference

with an associated uncertainty estimate, and that this quality assurance needs to be implemented over the entire validation and data-processing chain too. In the ideal case the reference would be SI traceable which means that the measurements of variables can be traced back to the International System (SI) of units (Goldberg et al., (2011)). CEOS (Committee on Earth Observation Satellites) encapsulates this in the Quality Assurance Framework for Earth Observation;

'All data and derived products must have associated with them a Quality Indicator (QI) based on documented quantitative assessment of its traceability to community agreed (ideally tied to SI) reference standards.'

In Leroy et al., (2008) the concept of climate benchmarking is discussed. They provide a quote from the U.S. National Research Council (NRC) who called for a change in the way climate was observed and monitored from space – systems should be designed to obtain climate records that are of *'high accuracy, tested for systematic errors on-orbit, and tied to irrefutable standards'*. It is also stipulated that *'the accuracy of core benchmark observations must be verified against absolute standards on-orbit by fundamentally independent methods, such that the accuracy of the record archived today can be verified by future generations. Societal objectives also require a long term record not susceptible to compromise by interruptions in that data record'*. Leroy et al., (2008) refer to climate benchmarks as observations that satisfy the above guidelines from the NRC. Often in climate monitoring, the instruments are assumed to be stable, however for climate benchmarking, in line with the previous discussion, instruments must be traceable back to an international measurements standard. This means that the measurements by these instruments are known to be accurate to within a certain degree. A climate benchmark is just one measurement, so by taking them over a series of time it is possible to create a time series and observe if there is any change or trend in the variable.

In order to create a series of climate benchmark measurements, it is important to have regular satellite missions. This is outlined in the ESA's 'Living Planet Programme' from 1998 in which they specify science and research goals and has the main aim of delivering smaller, more focussed and more frequent satellite missions (ESA, (1998)).

ESA launched its first meteorological satellite (Meteosat) in 1977 and has followed up with multiple satellites since (including the series of Meteosat satellites and Envisat). One of the statements from ESA is to *"develop satellite missions with maximum impact on understanding of the Earth System behaviour, with an appreciation of where the key gaps are, and where other space agencies are contributing"* (ESA, (2006)).

Traceable Radiometry Underpinning Terrestrial- and Helio- Studies (TRUTHS) is a proposed mission by the National Physical Laboratory (NPL) in the UK to ESA. The concept of TRUTHS is summarised in Fox et al., (2011) as:

'a mission to measure, SI traceably and with unprecedented accuracy, the interaction of solar radiation with the earth as a benchmark reference to enable the detection of decadal climate change.'

1.2.4 TRUTHS

TRUTHS is planned to be an Earth Observation satellite that will have high radiometric accuracy and SI traceability in orbit such that it can be used to inter-calibrate other satellites to these SI traceable standards, i.e. it will be a *'standards laboratory in space'*. Another aspect of TRUTHS is that it will be possible to measure spectrally resolved radiation in order to identify changes and attribute these changes to various processes. There is also the hope that it will be possible to take the data from TRUTHS and compare it to Earth System models in order to assess how well we model climate and climate processes, and to improve our understanding of these processes and our ability to predict future changes.

One area of atmospheric physics that is poorly understood is cloud radiative forcing (CRF), particularly how low clouds affect Earth's albedo (Wielicki et al., (2013)). Radiative forcing is the imbalance caused in the ERB at the top of the atmosphere as caused by a certain factor - in this case, clouds. The IPCC Fifth Assessment report (IPCC, (2013)), states the total anthropogenic radiative forcing is approximately 2.3Wm^{-2} and the radiative forcing for cloud-aerosol interations as -0.45Wm^{-2}, both for the time period 1750-2011. These values are calculated from a combination of observations and

model simulations. Considered here is the global mean shortwave CRF which fundamentally is the difference between the all sky and clear sky reflected fluxes (Wielicki et al., (2013)). Using the accuracy of the trend in the shortwave CRF, it is possible to investigate the effect of the calibration accuracy of an instrument. Figure 1.4 shows the trend accuracy with 95% confidence on the y-axis (as the percentage of CRF per decade), against the length of the record. The plotted lines show examples of increasing calibration accuracy (also with 95% confidence). These lines show the relationship between the calibration accuracy of an instrument, and the trend accuracy and time it would take to detect such a trend. The solid black line shows the case for a perfect observer (at 0%), and the further lines represent current and future instrument accuracies.

Figure 1.4 is an example of how a TRUTHS-like mission could greatly improve on the ability to detect a trend in the CRF as an example, on shorter timescales than is currently viable (Fox et al., (2011), Wielicki et al., (2013)). At the 100% positive cloud feedback line at 1.2%CRF/decade it is possible to see how long it would take various missions with increasing calibration accuracy to detect the trend in the CRF. TRUTHS is at 0.3% and is shown by the blue line and it is clear that TRUTHS closely follows the curve of the perfect observer. Figure 1.4 shows that the time to detect a trend at 100% is approximately 12 years, which is a significantly shorter timescale compared to CERES which would take twice as long at approximately 25 years, and MODIS (Moderate Resolution Imaging Spectroradiometer) which would take 40 years. In little over a decade it would be possible to detect a trend in the CRF with a mission such as TRUTHS operating at 0.3% accuracy, and improving the accuracy towards a perfect observer would not make a significant difference in the time to detect a trend.

It is thought that there may also be potential for TRUTHS to shorten the time to detect trends in other ECVs. The list of climate variables that TRUTHS could potentially be able to help with is vast; solar irradiance, ERB, surface albedo, cloud cover/optical depth/particle size, water vapour, ocean colour, ice/snow cover, vegetation and land use via direct observation, and the measurements could also impact on ozone and

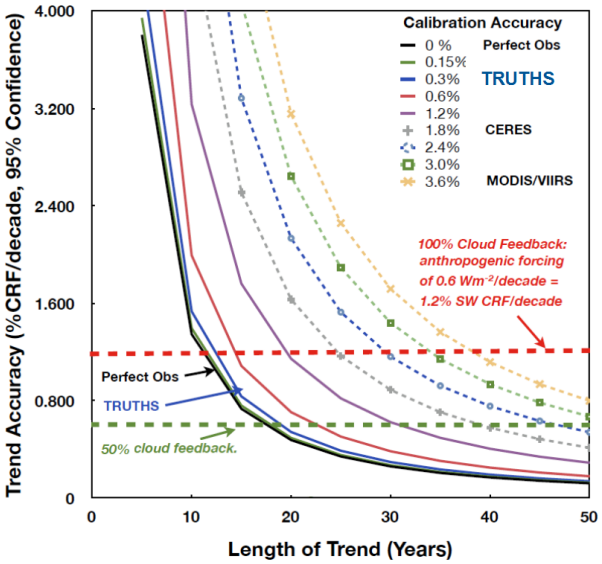


FIGURE 1.4: Trend accuracy of cloud radiative forcing (CRF) against the time observing, with lines showing various calibration accuracies of current and future instruments, and a perfect observer (adapted from Fox, (2010)).

aerosol optical depth (AOD) using TRUTHS for reference calibration (Fox, (2010)). Whether or not this would be feasible is yet to be determined.

TRUTHS was first proposed to ESA in 2002, and again in 2011, as a complementary mission to CLARREO (Climate Absolute Radiance and Refractivity Observatory) which has been proposed to NASA. The CLARREO mission, discussed in detail in Wielicki et al., (2013), is planned to be another high accuracy, SI traceable satellite mission. It also aims to observe the decadal variations in climate to improve our knowledge and understanding of climate forcings and feedbacks. However, CLARREO is proposing to also operate with an IR spectrometer covering a spectral range of 200-2000cm^{-1} and will measure the outgoing infrared radiation from Earth with 95% accuracy as well as being able to observe the reflected solar radiation between 320-2300nm at an accuracy of 0.3% - the same as TRUTHS. CLARREO will also use Global Navigation Satellite System Radio Occultation (GNSS-RO) receivers to measure atmospheric refractivity (Wielicki et al., (2013)). While TRUTHS will not make use of RO, it will have an absolute radiometer in the solar reflective domain which CLARREO does not have. The current status of TRUTHS is that the proposal will be submitted for Earth

Explorer 10 in 2018. Presently, the full CLARREO mission is indefinitely delayed although a proof of concept smaller mission - CLARREO Pathfinder - is scheduled to be launched within the 2022 time frame. While the two missions have some overlap, they are complementary and it is understood that both CLARREO and TRUTHS are needed in order to constrain climate change, particularly if the smaller scale CLARREO Pathfinder mission goes ahead.

Not only will TRUTHS be a complementary mission to CLARREO, it will improve on previous missions, like CERES and MODIS, as discussed previously. CERES was itself an improvement on the ERBE satellite with the intention to continue the data record of the TOA radiative fluxes as made by ERBE. CERES was also primarily concerned with the effect of cloud on the radiation budget, rather than the broader effects on the radiation budget, and only measured broadband fluxes (in three channels; shortwave, longwave and total) (Wielicki et al., (1996)). MODIS was launched on the NASA Terra and Aqua Earth Observing System satellites and only made measurements in 36 channels between 415nm and 14,235nm. In this range, the highest spatial resolution of 250m is at two spectral bands centred on 650nm and 860nm. Other bands have spatial resolutions of 500m and 1km (Platnick et al., (2003)). TRUTHS will improve on missions such as these as it will perform spectrally resolved measurements of the TOA radiative flux which will provide more information about climate change over time. TRUTHS will also operate at a higher spatial resolution than e.g. MODIS, which means that specific signals in regions may be detected and therefore can be attributed, in order for mitigation strategies to be put in place.

The current design of the instrumentation on TRUTHS is made up of six components; the hyperspectral Earth imaging spectrometer, Cryogenic Solar Absolute Radiometer (CSAR), irradiance sphere, transfer radiometer, diffuser wheel, and the laser diode suite with the rotating arm. The Earth imaging spectrometer will measure the spectral radiance from the Earth and SSI. The configuration of these components within the satellite is shown in Figure 1.5. The irradiance sphere is simply a hollow ball into which light is shone, where it reflects around inside and integrates itself and then comes out uniformly (for lasers and Sun). The transfer radiometer will measure the power from

the laser diode suite or the radiance reflected off the diffuser wheel. The diffuser wheel contains two diffuser plates, an aperture and a mirror and is what the Earth Imager is pointed towards. Finally, the laser diode feed bundle provides a monochromatic laser beam at six known wavelengths of which the cryogenic and transfer radiometers will measure the power. The lasers are connected to the rotating arm via a fibre optic cable (Fox, (2010)).

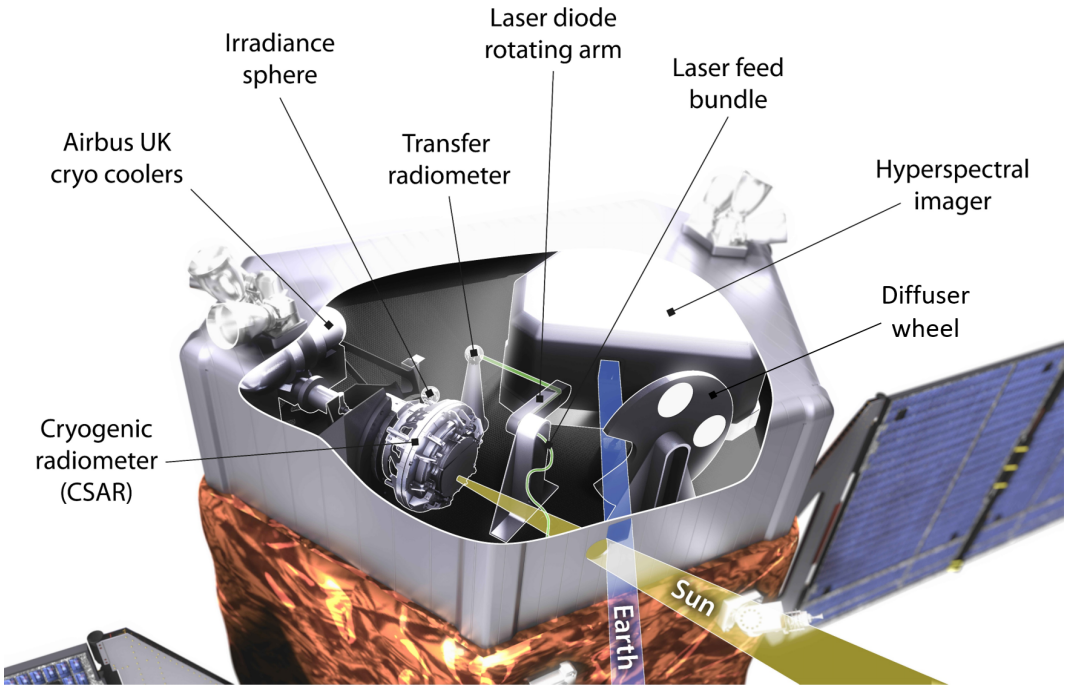


FIGURE 1.5: Diagram of the inside of the TRUTHS satellite and placement of instrumentation. (Courtesy of Paul Green).

The unique selling point of TRUTHS is the on-board calibration system that will deliver the ability to make SI traceable measurements and will lead to the improvement of other earth observation satellites. Traditionally, on-board calibration systems are fairly simple and use instruments that have already been proven to work and flown on other missions. One interesting feature of TRUTHS is the plan for it to be the first satellite with a Cryogenic Solar Absolute Radiometer (CSAR) on board. The CSAR was developed at the National Physical Laboratory (NPL) over 30 years ago and is used worldwide to calibrate instruments at terrestrial sites, however a version has been developed at NPL to be flown on the TRUTHS satellite. The cooling of the radiometer to cryogenic temperatures of <30K (approximately 20K on-board TRUTHS) reduces the uncertainty of the measurements by >10 times. The cryogenic radiometer on TRUTHS

is designed to have an accuracy of 0.02% in orbit, which is a factor of 10 less than has been proven on the ground and therefore will hopefully provide higher accuracy in practice.

Fundamentally a CSAR works on the principle that optical power incident on a black, spectrally flat, absorbing surface will cause said surface to rise in temperature. This temperature change can then be measured by a thermometer. The power is then switched off, and the same temperature rise is then caused by running an electrical current through a heater. The electrical power can then be equated to the optical power. Since electrical power can be measured easily, this allows optical power to be reliably measured through substitution. On TRUTHS, a cavity is used to maximise the absorptance, since some uncertainty arises from the reflection from a metal surface. These cavities do not need to be calibrated and have an absorptance of 0.99998. Since the absorptance is so high, it would take significant degradation to decrease the overall uncertainty. The cavity is also spectrally flat which means it can be used to make measurements in any spectral band without issue.

In this case, the CSAR functions by measuring the power of monochromatic radiation at six pre-defined wavelengths, provided by a laser-diode suite. Once the power of the monochromatic radiation is known, the lasers can be used as input into the other on-board optical instruments (discussed below) in order to provide the calibration in orbit. The CSAR measures the TSI directly when the laser input is switched for solar irradiance, however the Earth imager and transfer radiometer must be calibrated from the CSAR.

Two measurements that will be made on board are of the solar spectral irradiance (SSI) and the Earth reflected solar radiation, both of which will be measured to 0.3% accuracy. In order to obtain 0.3% radiometric accuracy in the measured values for the Earth reflected solar radiation, 99.7% of the solar spectrum must be observed, which means observing over almost the whole solar spectral range of 320-2300nm. Not measuring over the whole range means that estimates have to be made about the spectrum which introduces larger errors. The third variable to be measured is the total solar irradiance

(TSI), which will be measured to an accuracy of 0.02%.

The calibration method on TRUTHS follows several steps. The first stage of the process is calibrating the transfer radiometer against the CSAR; by shining the laser diode at each single wavelength into the CSAR, the instrument will measure how much power is in that laser. The same laser is shone into the transfer radiometer, and since the power from the CSAR is known, it is possible to calibrate the transfer radiometer. This is then repeated for all six wavelengths from the laser diode suite. The next stage is to calibrate the Earth imager against the transfer radiometer. Rotating the delivery arm in a circle means it is possible to point the laser into the irradiance sphere. When the light enters the irradiance sphere, it comes out of the other side and is focussed from the mirror onto a diffuser plate and then onto the diffuser wheel. The diffuser wheel is the second part of this system design that moves. The diffuser wheel can be rotated so that either a diffuser, mirror or aperture is seen by the Earth imager. If a second diffuser plate is used, this means that the light is twice as diffuse which reduces the power, and this is why there is a mirror option on the diffuser wheel so that in some cases the light is only diffused once. The transfer radiometer, which can also see the diffuser plate, measures the radiance and this can be compared to the radiance measured by the Earth imager. These steps are taken to calibrate the Earth imager.

The next steps are to calibrate the instruments for irradiance. As is shown in the diagram, the rotating arm with the laser diode suite also has an aperture built in – this is to allow solar radiation into the irradiance sphere, and therefore illuminate the diffuser, as before. The Earth imager can measure this, thus correcting for spectral solar irradiance measurements. Knowing the radius of the aperture at the entrance to the irradiance sphere is important and measurements are reliant on that aperture staying the same. A calibration for the aperture area will be done pre-flight but since this area will be exposed to direct sunlight (cosmic rays and high energy particles will be incident on the surface, potentially creating small holes/increasing the aperture to let more light in) it will need monitoring in-flight. This can be done by shining the laser at all of the apertures and measuring if there is more light coming in than during the previous calibration, which can be corrected for. Finally, the total solar irradiance (TSI)

can simply be measured directly by the CSAR, again using the aperture on the rotating arm. (Fox, (2010))

As mentioned previously, and shown in Figure 1.5, there are two diffusers on the diffuser wheel. Since the material of the diffuser will degrade over time due to being exposed to UV radiation, the idea is that one of the diffusers will be used on a daily basis, whereas the other will only be used occasionally to observe and measure how the diffuser degrades. As mentioned previously, it is usually assumed that the diffuser changes in a certain way, following a specific degradation curve, but if this method can be used it will be possible to see exactly how the diffuser surface is changing over time. Not only this, but one diffuser will be able to rotate – this means it will also be able to check the symmetry of the diffuser plate in order to map the reflectivity of it. All of these stages combined mean it would be possible to accurately calibrate the systems and adjust the measurements as time goes by, and pass these SI traceable standards to other satellites.

In this current system, there are only three moving parts; the rotating arm connected to the laser diode suite, the diffuser wheel rotates, and finally one diffuser that turns in its place. It is possible to cut this down to only two movements, and have the diffuser stationary. While it is not necessary to have this extra rotation it is expected to improve the confidence in the calibration.

The planned orbit of the satellite is expected to encounter several near simultaneous overpasses with various other Earth Observation satellites (that are be in geostationary or sun-synchronous orbits). These flyovers enable the transfer of the calibration to these other sensors such as GERB (Geostationary Earth Radiation Budget, Sandford et al., (2003)) and CERES (Clouds and Earth Radiant Energy System). The planned spectral and spatial resolution of TRUTHS means that it should be possible for its radiance measurements can be 'matched' to those of other sensors - TRUTHS needs to have a spatial and spectral resolution higher than the instruments which it is planning to calibrate. TRUTHS could potentially be used to improve terrestrial sites too such as LANDNET (Gürbüz et al., (2012)) and AERONET-OC (Aerosol Robotic

Network - Ocean Colour, Zibordi et al., (2009)) and Ocean Colour buoys. There is an idea that the past data retrieved from such sites could potentially be corrected which would mean highly accurate climate records going into the past – the more years of TRUTHS quality data we have increases our chances and reduces the time it will take to detect trends and understand climate processes. The logistics of this may or may not be possible.

Currently, the best imaging instruments around are operating at about 4% accuracy (MODIS) and the best reflected solar instruments (on CERES) are operating at about 2% accuracy (Wielicki et al., (2013)), both of which are an order of magnitude larger than what TRUTHS is aiming to be capable of. So there is improvement that can be made by inter-calibration between these types of instruments and a TRUTHS-like mission. TRUTHS will potentially be working at 0.3% accuracy, whereas e.g. the multi-spectral imager (MSI) instrument on Sentinel 2 is at 3-4%. All previous sensors have had an accuracy of only 2-6% because of the way on-board calibration has been carried out in the past and the problems with degradation which mean that there is no traceability in orbit (Fox, (2010)). One thing that needs to be considered is if it is possible to improve the accuracy of other satellites with TRUTHS. It is important to know what this improvement in accuracy would actually do for the scientific community that use the data and will that increase in accuracy of the measurements be useful to them.

The way in which TRUTHS can be used to inter-calibrate these other sensors is to do a near simultaneous measurement of a certain target by the two sensors where TRUTHS is the reference standard. For this option, the two satellites are required to have nearly identical placement in space/time/angle since the reflectance of the Earth is dependent on these viewing positions. By having the overpasses within 10-20 minutes of each other, the sensors can take several shots of the same site at varying angles and the calibration is given by the TOA reflectance ratio. Many test sites for this purpose have been identified, both land (LANDNET test-sites) and ocean sites on Earth, and also one on the Moon.

At present, it is proposed that the TRUTHS satellite should be in a nearly circular 90°

precessing polar orbit at 609km altitude, which would mean a revisit time of 61 days. The instruments are planning to take global nadir spectral radiances continuously in the spectral range of 320-2300nm which covers from the UV to the shortwave infrared (SWIR). The spectral resolution of the spectrometer is assumed to be <5nm for the range 320-1000nm (UV-NIR) and then <10nm for the range 1000-2300nm (SWIR). The current plan allocates 5-10 minutes each day for solar observations. The swath width of the satellite is expected to be in the region of 50-100km or larger. The planned lifetime of the satellite is set to be three years at the very minimum but the longer the better with regards to obtaining data and detecting trends above natural variability for climate change and so a lifetime of more than five years is preferable. TRUTHS will also be able to distinguish between clear and cloudy conditions. Using data from the Earth imaging spectrometer, it is possible to determin the cloud fraction. In order to perform this differentiation, a pixel size of <500nm is required, with TRUTHS intending to use a pixel size of 100nm in the imaging spectrometer. With regards to the spatial resolution on the ground; there will be a resolution of 50-100m over land, and 200m over ocean which will also allow surface differentiation.

The design of TRUTHS is ever evolving and subject to changes based on on-going studies and simulations. There are areas that need to be further examined such as the orbit of the satellite and whether 90 degrees and/or 609km is best for the kinds of observations that need to be made, and what changing this orbit would do to the measurements. It should also be investigated whether this orbit provides enough over-passes with other satellites and whether this is the optimal orbit for transferring the calibration standards to other sensors. The spectral range and resolution can also be explored to see if the range is large enough to capture the changes expected in the resolved spectra, based on simulations to gauge the spectral signatures and magnitudes of changes. Also, the spectral resolution needs to be small enough to resolve spectral features, and also needs to be better than current EO satellites in order to calibrate them to SI traceable standards. Another aspect of the mission that can be looked into is the proposed lifetime of the satellite and whether it is long enough to make sufficient impact into inter-calibrating other systems and contributing a long enough data record for the spectrally resolved radiances in order to calculate time series for ECVs

and detect trends.

Finally, observations underpin the formulation of models as well as evaluating model performance so it is vital to more accurate and more complete measurements of the Earth system. TRUTHS could help the modelling community by providing these accurate measurements over time of a variety of ECVs which can be used to assess how well the models are performing in the first place. These observations can also be used to correct the models so that they are representative of the current climate and how it's evolving, which should enable making more accurate forecasts of how the climate will potentially change and analyses of how to mitigate these changes, as is done by the IPCC in their regular reports (IPCC, (2013)). In order to make policies and come up with strategies to deal with climate change, the first stage is to understand the size and rate of the changes, where these changes are occurring and this is how missions like TRUTHS could help.

1.3 Thesis Outline

The structure of this thesis is as follows. Chapter 2 includes details of the main data set used in these studies. The data set used was produced as part of a Climate Observing System Simulation Experiment (COSSE) by Feldman et al., (2011)(a) at the same spectral range and resolution as TRUTHS. COSSEs are designed to simulate real climate observations in order to test the abilities of different instruments and designs to meet mission goals. Chapter 2 also outlines the radiative transfer model, libRadtran, that forms the basis of the initial experiments. The methods and results of these studies are discussed in Chapters 3-5. The focus of Chapter 3 is to understand which variables and processes affect the shortwave radiation, and to what extent. This was investigated by conducting a variety of sensitivity studies using libRadtran. Chapter 4 makes use of the COSSE data set to calculate the time it would take a TRUTHS-like satellite to detect the signals of climate change above the noise of natural variability. The effect of the spatial resolution on the ability to detect signals and on the relative signatures of land and ocean is also considered. Finally, in Chapter 5, as satellites have a limited lifetime,

gaps are added into the continuous COSSE data set to simulate real climate records. The time to detect the same signals was calculated in order to understand more realistically how a TRUTHS-like satellite would perform. This also gives an indication of the optimum number of satellites required, and the gap between them, in order to still confidently detect a climate change signal. Chapter 6 summarises the conclusions of these studies, and identifies areas of potential future research.

Chapter 2

Data and Tools used in this Study

In this chapter, the details of the tools and data set used in this thesis will be discussed. Firstly, the radiative transfer model used in the sensitivity studies in Chapter 3 to explore the effects of different variables on reflected shortwave radiation will be described in Section 2.1. As this study is centred on the TRUTHS satellite which is yet to be built, real data is not available. Therefore the data set used in Chapters 4 and 5 for the detection time analysis consists of simulated climate data, which is discussed in Section 2.2.

2.1 Tools - Radiative Transfer Model

As these studies are fundamentally based upon the Earth's TOA reflected shortwave radiation and its variability, it is important to gain an understanding of how various key factors affect this quantity. In order to do this, a radiative transfer model was used to perform sensitivity studies. While there are many radiative transfer models available that are widely used, such as MODTRAN (Berk et al., (1998)) and LBLRTM (Clough et al., (2005)), libRadtran (Mayer and Kylling, (2005), Mayer et al., (2014)) was chosen for this study. LibRadtran was chosen for several reasons; it covers the wavelength range of reflected SW radiation (the full range in libRadtran being 120nm - 100μm), it is capable of both band and line-by-line calculations, and it takes into account scattering processes. Finally, libRadtran is publicly and freely available. It was important to these sensitivity studies that the ability to take scattering into account in

the calculation was included, and that the program was easily available, which is why libRadtran was more suitable.

LibRadtran has been extensively validated by comparisons with various measurements, and also with other radiative transfer models as discussed in Mayer and Kylling, (2005). It has also been used for a wide range of research including analysis of UV radiation, cloud and remote sensing, remote sensing of surface properties, trace gas remote sensing, simulation of radiances for numerical weather prediction models, and validation of radiation schemes in climate models etc. (Emde et al., (2015)). For example, libRadtran is used as the reference in the shortwave in Forster et al., (2011) in order to evaluate radiance scheme performance. The details of the libRadtran code are provided in the following section.

2.1.1 LibRadtran

LibRadtran is the 'Library for Radiative Transfer' (Mayer and Kylling, (2005), Mayer et al., (2014)) and is a library of routines. The main routine is called 'uvspec' which is used to calculate spectral irradiances and radiances at all atmospheric levels under various atmospheric and surface conditions. Uvspec itself is unique in that it includes 10 different radiative transfer solvers, depending on the requirements of the user. LibRadtran has a separate routine to perform Mie scattering calculations to calculate optical properties for spherical particles, and there is one solver for 3D radiative transfer equations. Here, only the solver DISORT (Stamnes et al., (1998)) has been used. DISORT was chosen for its ease of use and ability to provide accurate calculations of the radiance, the variable of interest, and is a 1D solver. DISORT is described in the libRadtran User Guide (Mayer and Kylling, (2005)) as '*the most versatile, well-tested and mostly used 1D radiative transfer solver*'.

LibRadtran also makes use of the HITRAN (high-resolution transmission molecular absorption) 2004 line database, though there are more recent versions of the HITRAN database with the latest release being 2016. With the more recent versions, there are important updates, such as revised line intensities and positions for H_2O, and more

accurate line positions, intensities and shapes for CO_2 based on various experimental and theoretical studies (Gordon et al., (2017)). However, for the purpose of these sensitivity studies, the 2004 database is sufficient. HITRAN is a database formed of absorption cross sections for various molecules, refractive indices of aerosols and line parameters (such as position and strength) for various gas phase molecules (Rothman et al., (2005)). Radiative transfer models, such as libRadtran, read in these parameters as inputs in order to perform their calculations.

Figure 2.1 is a schematic that shows the order of the processes within uvspec. The primary stages are to set up the user defined inputs in order to describe the environmental conditions of the simulation for the radiative transfer calculations. This includes defining the extra terrestrial solar input at TOA, the surface features, and the atmospheric conditions in between. Starting from the TOA input, it is possible to select which solar spectrum (1 or 0.1nm resolution) for which the Kurucz (Kurucz, (1994)) solar spectrum was chosen at 1nm spectral resolution. There are other extra terrestrial data sets available within libRadtran, however these either did not cover the appropriate range of wavelengths (e.g. 200-800nm), or provided data at varying resolution across the spectrum. Kurucz, however, ranges from 250-10,000nm and the values are provided at 1nm across this whole range. The solar zenith angle (SZA) can also be set in order to look at the effect of the Sun's elevation on the incoming solar radiation.

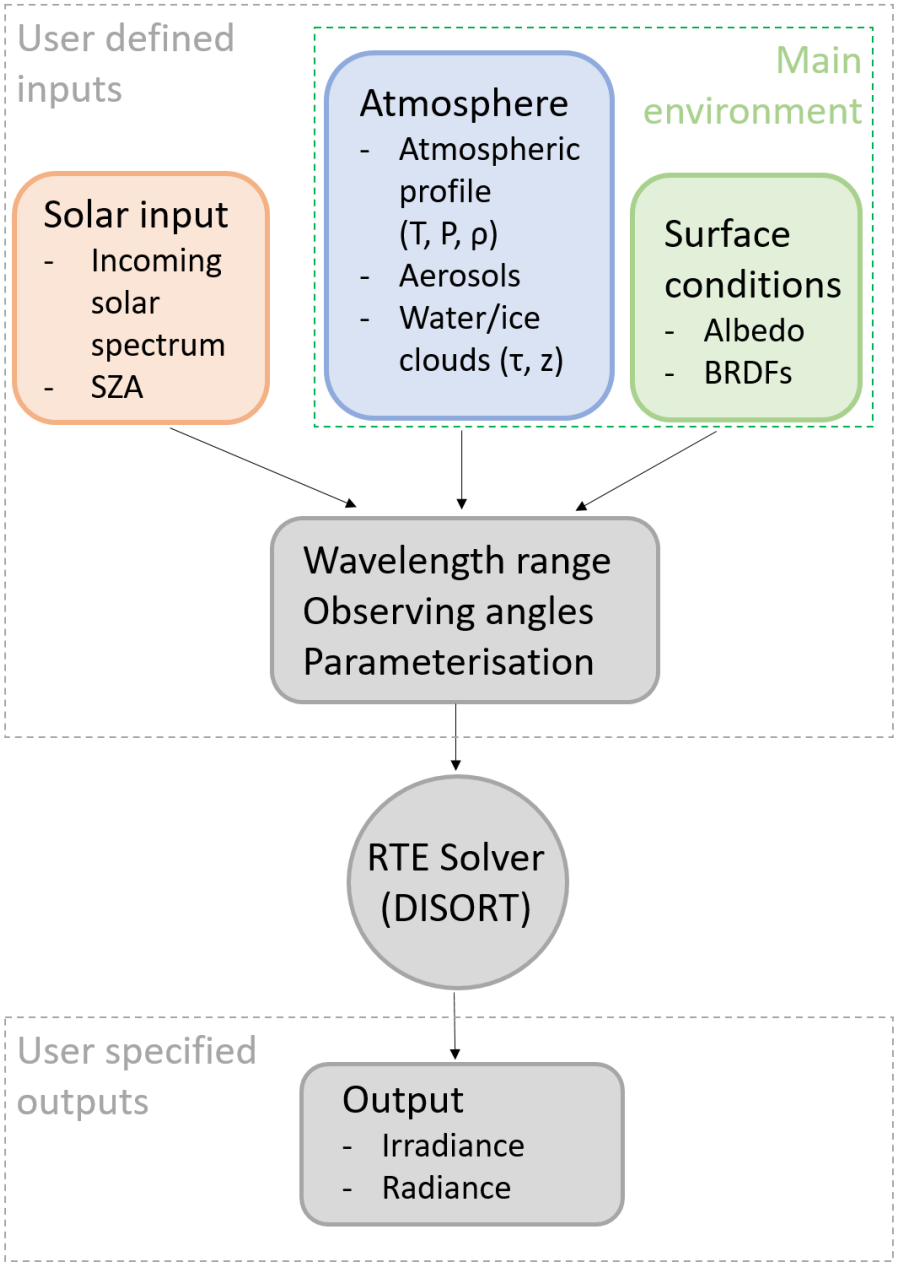


FIGURE 2.1: Flow chart of the inputs and outputs for uvspec in libRadtran. Variables T, P and ρ are temperature, pressure and gas densities respectively. Cloud variables τ and z are cloud optical depth and cloud height respectively.

The atmospheric profile can be selected from one of six predefined standard cases described by Anderson et al., (1986). These include tropical, subarctic summer, subarctic winter, mid-latitude summer, mid-latitude winter, and the U.S. standard atmosphere. These profiles give concentrations of O_3, O_2, H_2O, CO_2 and NO_2, and are provided from the surface to an altitude of 120km at pre-defined altitudes. The altitudes from 0-25km are at 1km intervals, then 25-50km at 2.5km steps, and finally from 50-120km every 5km. The temperature and pressure are also provided at these same altitudes. It is, however, possible to alter the concentrations of any of the above constituents to any required value. An example of selected constituent profiles (water vapour and O_3) for the US standard atmosphere can be seen in Figure 2.2. These profiles are only shown for altitudes up to 60km, as above this height the concentrations are significantly smaller and the profiles are featureless.

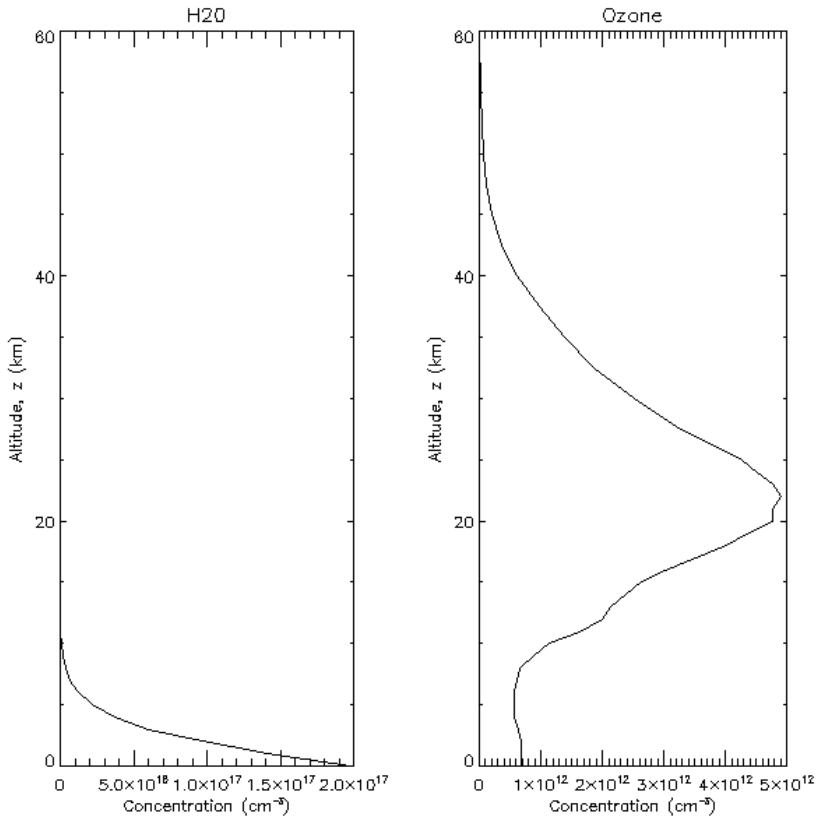


FIGURE 2.2: Atmospheric constituent profiles for water vapour (left panel) and ozone (right panel) in the US Standard atmosphere.

Molecular absorption and Rayleigh scattering are calculated by libRadtran by default. The code allows the user to include aerosols in the definition of the atmosphere and libRadtran provides various aerosol profiles for generalised conditions. These conditions cover both land and sea and are Antarctic, a continental average, clean or polluted continental, desert, urban, tropical maritime, and clean or polluted maritime. These profiles are provided from OPAC (Optical Properties of Aerosols and Clouds) (Hess et al., (1998)), and Table 2.1 shows the composition of the main constituents of each of the above aerosol types. In Hess et al., (1998) these aerosol types are defined as follows. The clean continental aerosol is representative of remote continental regions, or regions with low anthropogenic influences, while the polluted continental aerosols have high soot levels and represent regions significantly polluted by human activity. The average continental aerosol is, naturally, an average between the two previous continental examples, and represents areas that are influenced by human activity. Urban aerosol is representative of very highly polluted regions, with soot levels even larger than that of the polluted continental aerosol. The desert aerosol is not specific to a certain desert, such as the Saharan or Arabian deserts, but is representative of the general aerosol types and quantities that would be found in a desert area. The maritime aerosols are for undisturbed areas (clean) and for regions subjected to anthropogenic influences (polluted), while tropical maritime aerosol has lower sea salt levels due to an assumed lower wind speed. Finally, the Antarctic aerosol is specific to this region and also specifically for summer conditions.

The aerosol profiles available in libRadtran include the concentrations of the constituents at specific heights, as opposed to the single density values shown in Table 2.1. Figure 2.3 shows how some of these aerosol constituents vary both with altitude, and between the aerosol types. For Figure 2.3, the aerosol types chosen were urban and desert to show very contrasting aerosol types. The two panels in Figure 2.3 show the aerosol profiles for urban and desert aerosols with the three main constituents in each case plotted. In urban aerosol, the three constituents shown are insoluble aerosols, water soluble aerosols and soot. Insoluble aerosols are comprised of soil particles and also some organic matter, whereas the soluble aerosols are mostly sulphate, nitrates and other organic substances. Soot is absorbing black carbon and is not soluble. In the

Aerosol types	Components	N_i (cm^{-3})	M_i (μg m^{-3})
Continental clean	total	2600	8.8
	water soluble	2600	5.2
	insoluble	0.15	3.6
Continental average	total	15 300	24.0
	water soluble	7000	14.0
	insoluble	0.4	9.5
	soot	8300	0.5
Continental polluted	total	50 000	47.7
	water soluble	15 700	31.4
	insoluble	0.6	14.2
	soot	34 300	2.1
Urban	total	158 000	99.4
	water soluble	28 000	56.0
	insoluble	1.5	35.6
	soot	130 000	7.8
Desert	total	2300	225.8
	water soluble	2000	4.0
	mineral (nuc.)	269.5	7.5
	mineral (acc.)	30.5	168.7
	mineral (coa.)	0.142	45.6
Maritime clean	total	1520	42.5
	water soluble	1500	3.0
	sea salt (acc.)	20	38.6
	sea salt (coa.)	3.2E–3	0.9
Maritime polluted	total	9000	47.4
	water soluble	3800	7.6
	sea salt (acc.)	20	38.6
	sea salt (coa.)	3.2E–3	0.9
	soot	5180	0.3
Maritime tropical	total	600	20.8
	water soluble	590	1.2
	sea salt (acc.)	10	19.3
	sea salt (coa.)	1.3E–3	0.3
Antarctic	total	43	2.2
	sulfate	42.9	2.0
	sea salt (acc.)	0.47E-1	0.1
	mineral (tra.)	0.53E-2	0.1

TABLE 2.1: Composition of all aerosol types from OPAC; number density, N in cm^{-3}, and mass density, M in μgm^{-3}. Adapted from Hess et al., (1998). Table does not include all components of the aerosols.

desert aerosol, the three constituents shown are all mineral modes - accumulation, nucleation, and coarse minerals. The profiles in libRadtran are provided for 0-35km at a fixed vertical resolution (0-12km every 1km, and at 35km altitude), however the profiles here are confined to 0-5km as higher up in the atmosphere the profiles are similar with no distinguishing features, and the mass concentrations of the constituents are very low. As before, it is also possible to read in a specific aerosol profile or alter any of the values to meet requirements.

Another atmospheric condition that can be included is the presence of water or ice clouds. In order to do this, a separate cloud input file is created and read into the main environment, as seen in Figure 2.1. Setting the cloud base height and thickness of the cloud specifies the location, and then either the liquid water content and droplet size can be specified or the cloud optical depth can be set specifically, without the need for liquid water content and droplet size. There are various example files provided for clouds in libRadtran that can be used or modified. It is also possible to have a combination of both ice and water clouds in a multilayer cloud.

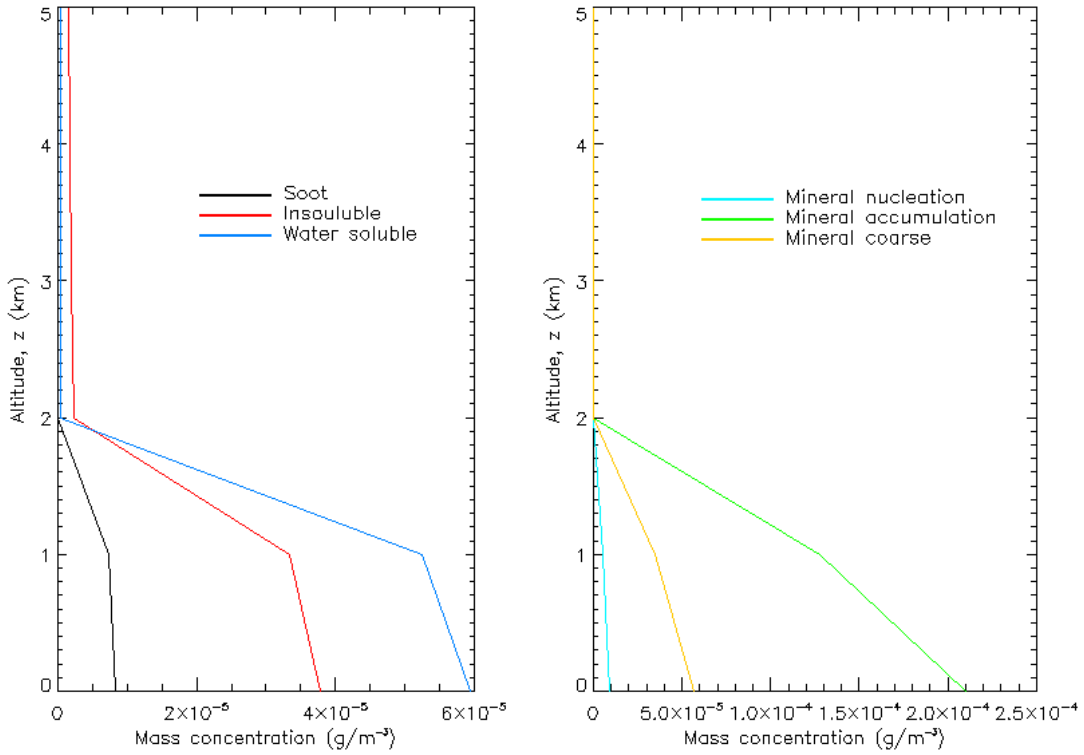


FIGURE 2.3: Aerosol profiles for water soluble/insoluble components, and soot, for two OPAC defined aerosol types (desert and urban). Note the difference in the scales for the concentrations.

Finally, the last set of inputs to define from Figure 2.1 are the surface properties. There are three options for the surface; to set the albedo to a spectrally constant value or include spectral variation and have a Lambertian surface (where the albedo has no dependence on viewing angle in both cases), or to use a Bidirectional Reflectance Distribution Function (BRDF) provided by libRadtran. Selecting a surface BRDF means that the albedo is inherently wavelength dependent, with further dependence on the azimuth and zenith angles.

Having set all of the input parameters for the incoming solar radiation, atmosphere and surface, the next stage of the uvspec process, as shown in Figure 2.1, is to specify the wavelength ranges, and any parameterisations. A band parameterisation is required in order to parameterise the molecular absorption from HITRAN, over a set spectral interval. For all cases, the parameterisation chosen was 'reptran'. Reptran itself works at three different resolutions - fine, medium and coarse. Here, reptran

is used at the default 'coarse' setting. This is the native resolution that the parameterisation is calculating the bands at, which is 15cm^{-1}. In the sensitivity studies in Chapter 3, the wavelength range is 300-2500nm at a 1nm resolution, and this is the resolution that the radiances are output at. In some cases, this output resolution will be higher than the resolution that the parameterisation is performing calculations at, for example between 240-395nm. Reptran uses the 'representative wavelength' method which means it performs the radiative transfer calculations at particular (representative) wavelengths. This method is a lot faster than performing the calculations line-by-line, but still tries to account for the fine line details from HITRAN. The parameterisation then calculates the output values based on weightings, in order to go from the 15cm^{-1} resolution to the required output resolution. By default, the output will be at the surface as opposed to TOA, and so here the output level must be defined. The output can be at any atmospheric level and the TOA is constrained by the atmospheric profiles which end at 120km.

The optical properties from the parameterisation are then input by uvspec into the Radiative Transfer Equation (RTE) solver, as seen in Figure 2.1. The default output from uvspec is in the form of irradiance - the direct downward irradiance, the diffuse downward irradiance, and the diffuse upward irradiance. However, if specified in the input file, the radiance will also be output along with the irradiances. These values can be output at any atmospheric level and this capability helps to identify the impact of perturbing different combinations of variables, as seen in Chapter 3.

2.2 Data

The aim of this study is to investigate how a TRUTHS-like instrument would perform, and aid in optimising the design of such an instrument. Therefore, the main part of this study looks at the ability of a TRUTHS-like instrument to detect a signal of climate change above the level of natural variability, or the time it would take to detect the signal confidently. In order to achieve this, an appropriate climate record is required. As

previously stated, TRUTHS is currently a proposed mission and so no suitable measurements are available, therefore another appropriate data set was required. For these studies, a simulated climate data set was obtained from a Climate Observing System Simulation Experiment (COSSE).

2.2.1 COSSE Data

OSSEs are used to simulate real observations in order to test the abilities of different instruments and designs to meet mission goals. Commonly used for weather forecasting applications, a recent development has been a move towards Climate OSSEs (COSSEs), based on the recognition that the current observing system is sub-optimal for climate monitoring (Weatherhead et al., (2017)). The experiments described here are based on data discussed in Feldman et al., (2011)(a) and Feldman et al., (2011)(b) and were provided by Dan Feldman at the University of Berkeley, California. These data are the product of COSSEs produced in order to investigate the capabilities of the CLARREO (Climate Absolute Radiance and Refractivity Observatory) mission; a NASA decadal survey satellite mission that has been designed to measure shortwave reflectances and IR radiances with in-orbit SI-traceable high accuracy (Wielicki et al., (2013)). The CLARREO shortwave instrument is designed to operate with comparable specifications to TRUTHS; it is planned that CLARREO would measure nadir reflectance from Earth within the wavelength range 320-2300nm at an 8nm resolution (Feldman et al., (2011)(b)). Given the similarities between the two mission designs the COSSEs from Feldman et al., (2011)(a) and Feldman et al., (2011)(b) can be employed to evaluate the potential capabilities of the TRUTHS mission.

The COSSEs were run for two different climate change scenarios from 2000-2100, both forced with historical greenhouse gas emissions and aerosols until 2000. The first is a 'control' run based on a constant carbon dioxide scenario, and the second is based on the Intergovernmental Panel on Climate Change (IPCC) AR4 A2 scenario (IPCC, (2007)) and is referred to here as the 'experiment'. The A2 scenario is defined by steadily increasing carbon dioxide levels (as well as CH_4 and N_2O) and with increasing sulphate aerosols until 2050, which then decrease to 1990 levels by 2100 (IPCC, (2007)).

These changes can be seen in Figure 2.4 which shows the increasing CO_2 levels, and also the evolution of sulphur dioxide levels in the atmosphere. Since SO_2 is a precursor to sulphate aerosol, the peak in SO_2 gas is earlier than in the sulphates themselves.

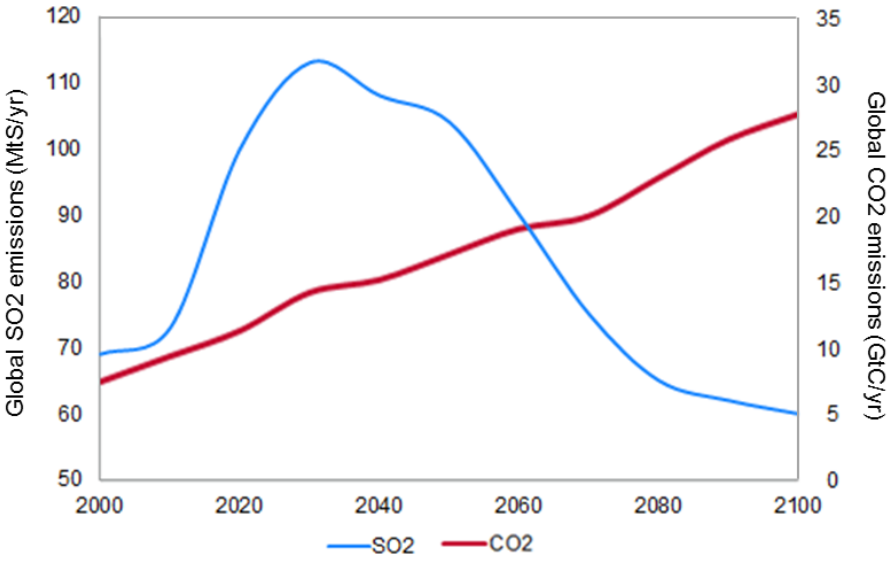


FIGURE 2.4: Evolution of CO_2 and SO_2 over time in the IPCC AR4 A2 emissions scenario.

In order to understand the temporal variability of certain key variables, and to check that they exhibited the expected changes given the characteristics of the climate change scenario, these variables were plotted. Figure 2.5 shows one of these variables, the aerosol optical depth (AOD). The data plotted in Figure 2.5 are the anomalies in the AOD, calculated by zonally and annually averaging the data and then subtracting the decadal average for the period 2000-2009, i.e. the first decade of the simulated data. The AOD peaks between 2020-2060, which is consistent with the A2 emission scenario specification of a peak in sulphates by 2050. The AOD then begins to decrease, along with the decreasing levels of sulphates until the end of the century. The COSSE data also contain the optical depths of several other components that contribute to the total AOD – soot, dust and sea salt. However, inspection of the dust and sea salt contributions to the total AOD show that these are negligible when compared to the soot and sulphates. Therefore, the change in AOD is dominated by the changes in the optical depths of sulphates and soot, both of which show a similar variability pattern to that

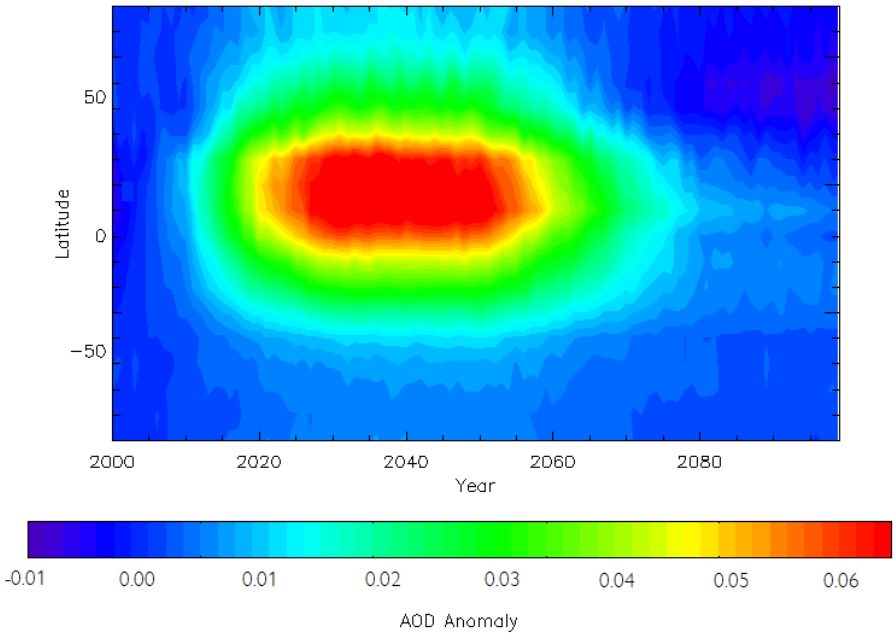


FIGURE 2.5: The zonally and annually averaged values of the aerosol optical depth anomalies over time for the A2 scenario experiment data, with respect to the average AOD at 550nm for the period 2000-2009.

seen in Figure 2.5.

The input for the radiative transfer simulation performed as part of the COSSE was created by the Community Climate System Model (CCSM3) (Collins et al., (2006)). Radiative variables were calculated using MODTRAN Version 5.3.0.0 (Berk et al., (1998)), with care taken to ensure that the integrated radiation variables from the more detailed calculations were compatible with the same variables as simulated directly by CCSM3. The simulated data from the COSSE are output as monthly means, for a variety of variables including (but not limited to) TOA spectral radiance, TOA solar downwelling flux, TOA diffuse upwelling flux, ice and water cloud optical depths and aerosol optical depths (for dust, sea salt, soot and sulphates). The radiance and fluxes are also produced for both clear and all sky conditions. In this study, 'clear sky' refers to cloudless conditions, but including aerosols and dust (i.e. not a pristine sky), and 'all sky' refers to cloudy conditions, also containing aerosols and dust. The data have full global coverage at a spatial resolution of 1.41x1.41° and cover the spectral range from 300-2500nm at a 8nm spectral resolution.

In this study, the variables of interest are TOA nadir spectral reflectance and TOA spectral albedo. These variables are not directly output by the COSSE but are calculated as follows. The TOA nadir spectral reflectance is defined as,

$$R_\lambda = \frac{\pi I_\lambda}{F_\lambda, solar} \tag{2.1}$$

where R_λ is the TOA reflectance at wavelength, λ, I_λ is the TOA upwards radiance (at a viewing zenith angle of 0°) and $F_{\lambda,solar}$ is the incoming solar flux at TOA.

The TOA spectral albedo, α_λ, is defined as,

$$\alpha_\lambda = \frac{F_\lambda^\uparrow}{F_\lambda, solar} \tag{2.2}$$

where $F_\lambda^\uparrow$ is the TOA diffuse upwards flux.

Finally, the broadband albedo, α, can be calculated as follows,

$$\alpha = \frac{\int_{\lambda_1}^{\lambda_2} F_\lambda^\uparrow}{\int_{\lambda_1}^{\lambda_2} F_\lambda, solar} \tag{2.3}$$

where λ_1 = 300nm and λ_2 = 2500nm.

Figure 2.6 shows 10° zonally and annually averaged broadband clear sky albedo anomalies for the entire 100 year period, calculated using Equation 2.3. These anomalies were calculated with respect to the average albedo for the first decade; 2000-2009. Figure 2.6 shows a strong negative signal emerging in the Arctic region – specifically for 70-90°N, which reaches -0.05. While there is a corresponding decrease at 60-70°S, it is smaller at <-0.035. These changes show that the albedo over time in these locations is decreasing compared to the first decade of simulations. Given that these are clear sky simulations and that the pattern of aerosol change is most marked in the tropics and mid-latitudes (Figure 2.5) it is most likely that these changes are a result of decreasing snow and ice fraction over both poles, but most significantly in the Arctic. Such a pattern is consistent with multi-model predictions of Arctic surface temperature warming reported

in IPCC AR4 (IPCC, (2007)). Figure 2.7 shows the clear sky spectral albedo anomalies at a specific latitude, 20°N, as a function of wavelength over the 100-year period. Figure 2.6 clearly shows that there is no appreciable broadband anomaly at 20°N for this time period. However, by analysing the spectrally resolved data, Figure 2.7 shows that there is in fact significant variation depending on which wavelength is observed. This suggests that by making spectrally resolved measurements there is the potential to detect signals and variability that could otherwise be missed if only broadband radiative quantities were measured. This shows that it is important for TRUTHS to make spectrally resolved measurements in order to observe more of this detail and therefore potentially detect signals of climate change faster.

Given the additional information contained in the spectrally resolved data, if there are specific wavelengths at which the signal of change is large and emerges quickly, then it needs to be ensured that these wavelengths are observed at a sufficiently high spectral resolution. However, there is a caveat in that the spectral distribution of the noise also needs to be considered as this will have a significant impact on the time to detection: it will only be possible to detect the spectrally resolved changes faster if the noise or natural variability in the data does not show a similarly rapid increase with spectral resolution. Accounting for this possibility is one of the strengths of the method employed in this research, as discussed further in Chapter 4.

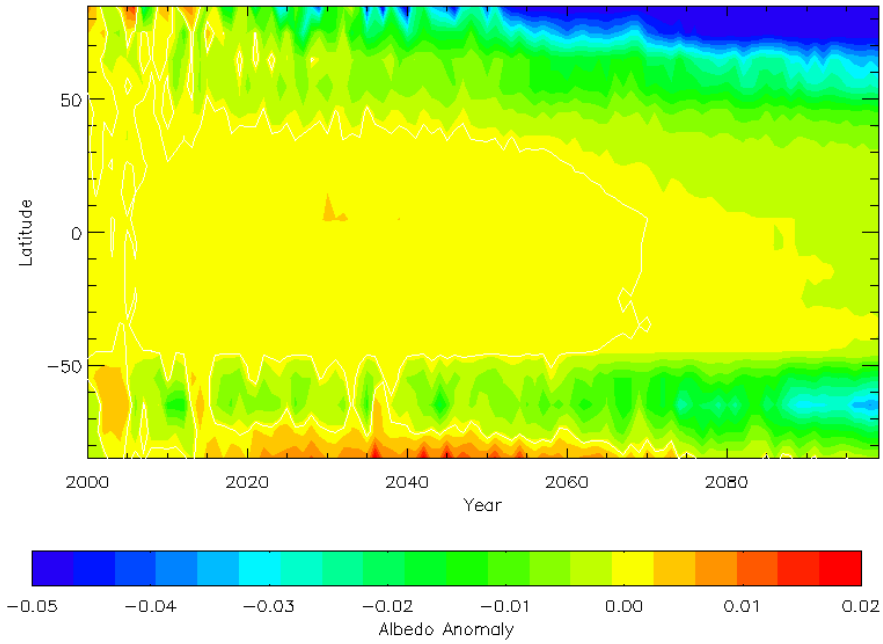


FIGURE 2.6: Zonally and annually averaged broadband clear sky albedo anomalies with respect to the average albedo for the period 2000-2009, at every 10° latitude band. The white contours highlight where the anomalies are zero.

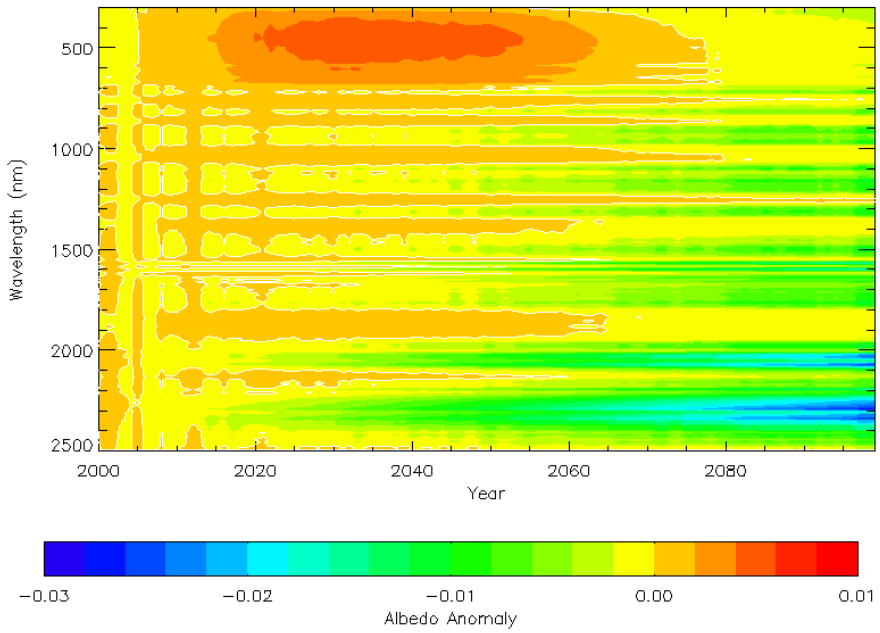


FIGURE 2.7: Zonally and annually averaged spectrally resolved albedo anomalies at 20°N. The white contours highlight where the anomalies are zero.

Having shown the importance of spectrally resolved data, specific wavelengths of interest were chosen to study in Chapters 3, 4 and 5. This is due to the fact that it is often unfeasible to investigate all wavelengths thoroughly due to processing time. The wavelengths chosen were chosen for various reasons. 550nm is a common wavelength used since it is a transparent band, and is often used to define optical properties, for example, the optical depth at 550nm. Then 660nm was chosen as it is in the red region of the visible spectrum, and 865nm was chosen as it is in the NIR and is used for red-edge vegetation characterisation, with both wavelengths used on Sentinel 2 (Li et al., (2017)). The water vapour absorption band centred at 940nm was chosen and would provide a useful comparison to the transparent wavelengths, since there are several water vapour absorption bands across the SW spectrum. 1375nm was chosen as it is used as a band centre for analysis of cirrus clouds on MODIS (Gao and Kaufman, (1995)), and is also in a water vapour and CO_2 absorption band. Sentinel 2 also uses a band centred at 1380nm for cirrus cloud detection. The wavelengths at 1600nm and 1680nm were chosen due to the fact that they are used to differentiate between ice and water cloud. Pilewskie and Twomey, (1987), discusses 1600nm being used for this purpose, with the absorption at this wavelength by ice clouds double that for water clouds, when comparing to lower wavelengths, such as 500nm. However, Knap et al., (2000), discusses the use of 1680nm, and shows that at this wavelength, water reflectivity is larger than that of ice. Both wavelengths were considered for comparison with lower wavelengths, and also to compare between the two wavelengths. Finally, 2190nm was chosen because it is a transparent band, and is also used by the Sentinel 2 satellite for snow, ice and cloud discrimination (Li et al., (2017)). Landsat also uses information from this band for plant and soil moisture analysis (Barsi et al., (2014)).

Chapter 3

Sensitivity Studies

As discussed in Chapter 1, it is possible to attribute changes in TOA SW spectra to various factors and effects, such as changes in atmospheric constituents. In order to do this, it is important to completely understand what these factors are, why they affect spectra, and also how they affect the spectra. It is for this reason that the following chapter investigates the effects of atmospheric constituents, clouds, surface properties, etc. in order to gain an solid understanding of the changes that could be observed by a TRUTHS-like satellite. Based on the analysis of the COSSE data shown later in Chapter 4, in Section 3.2 the focus is placed specifically on investigating the interplay between clouds and the surface in polar regions. Similarly, Section 3.3 investigates the effects of changing amounts of water vapour on the TOA reflectance, and the role of surface properties in modifying the response seen.

3.1 LibRadtran Sensitivity Studies

A variety of sensitivity studies have been conducted to try to gauge how the reflected solar spectrum varies and where the changes are spectrally depending on how the atmosphere and various conditions have been set up. The idea was to gain familiarity with the controls on the shortwave spectrum, and to identify spectral signatures associated with specific changes in the Earth system. By considering the possible changes that could occur in the Earth system, and analysing the resulting changes in the shortwave spectra, there is a possibility to optimise the design of a TRUTHS-like instrument in order to be able to successfully observe and measure these changes. For example,

changes are expected to occur in the future in aerosol amounts and so investigating the sensitivity of SW radiation to these changes and how these changes manifest themselves in the spectra indicates areas that could be of interest for a TRUTHS-like instrument to focus. This can then support the reasons for choosing specific spectral ranges and resolutions for TRUTHS.

3.1.1 Method

These sensitivity studies were performed using the libRadtran radiative transfer model described in Chapter 2. In these model runs, the spectrally resolved values for the TOA radiances were output, and then converted into TOA reflectances using Equation 2.1. The variables explored in Section 3.1.2 are the ozone levels, surface albedo, SZA and clouds. These were the initial sensitivity studies to investigate what affects the shortwave radiation spectrum, and the extent of these effects. For these experiments, the wavelength range was 300-2500nm. In these studies, the 'default' conditions used were as follows - a US Standard Atmosphere (Anderson et al., (1986)), a SZA of 30° and a uniform surface albedo of 0.25 which is broadly equivalent to a normal grassy scene (Park, (2001)). This default set-up had no additional aerosols or clouds. Figure 3.1 shows the TOA nadir reflectance spectrum for these default settings.

Following this, sensitivity studies were run specifically for polar regions, shown in Section 3.2. These were to investigate and understand how the SZA, surface albedo and clouds affect the radiation at various levels of the atmosphere in the polar regions, which were shown to exhibit high levels of noise in the COSSE runs analysed (discussed in Chapter 4). These studies were run at single wavelengths which were investigated specifically in Chapter 4, rather than for a wavelength range.

Finally, the last sensitivity study in Section 3.3 was to investigate how water vapour affects TOA reflectance over land and ocean surfaces. For these studies, the radiance was output so that the TOA reflectance could again be calculated and explored.

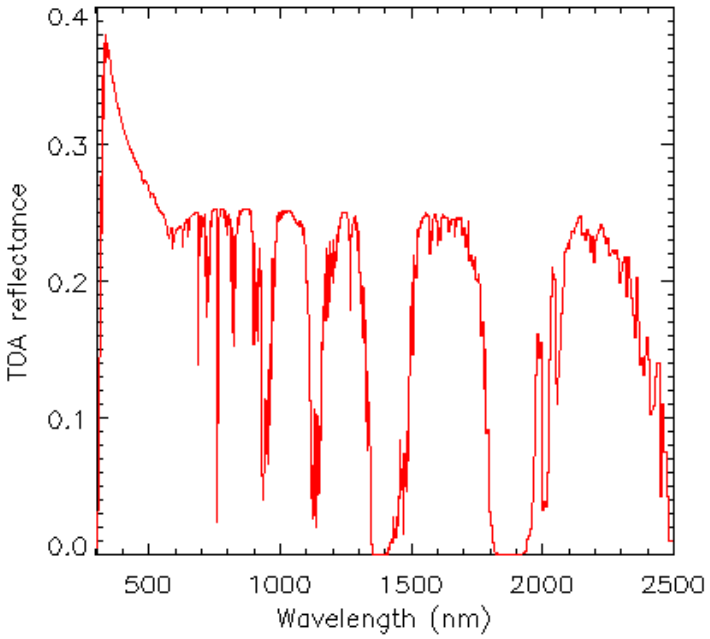


FIGURE 3.1: TOA nadir reflectance spectrum for 'default' conditions - a US Standard Atmosphere, a uniform surface albedo of 0.25 and SZA of 30°.

3.1.2 Variables and Effects

SZA and Ozone

The first sensitivity studies explore the effects of changing the solar zenith angle and concentration of ozone in the atmosphere on the TOA nadir reflectance spectra. The SZA sensitivity studies were run as a sanity check first, in order to inspect the TOA reflectance spectra, and check that the results were as expected before continuing with the sensitivity studies. For the SZA, the values chosen were 25, 50 and 75°. The US Standard Atmosphere (Anderson et al., (1986)) was used, along with a surface albedo of 0.25. As expected, increasing the SZA, significantly reduces the direct downward irradiance incident on the Earth. This is unsurprising since the SZA is the angle from the zenith, and so a larger SZA means the lower the sun is in the sky. When the sun is directly overhead, the radiation is direct, whereas at a larger SZA, the radiation covers a larger surface area and therefore is less intense. There is also the effect of the atmospheric path length - the larger the SZA, the further through the atmosphere the

radiation travels and is therefore attenuated more. This naturally results in a reduction of the TOA nadir reflectance with increasing SZA.

Next, the ozone runs were carried out with two different extremes to examine the effect ozone has on radiation. The runs were for 100 and 500DU; 100DU is the approximate value of the ozone in the ozone hole over Antarctica (Krummel et al., (2016)), and 500DU is the top end value of ozone, with the global average around 300DU (Burrows et al., (1999)). In these cases, the remaining variables were set to default.

Figure 3.2 shows 3 panels; the TOA nadir reflectance spectra for an atmosphere with 100DU of ozone (a), the same for an atmosphere with 500DU of ozone (b), and the difference between these two spectra (c) in order to explicitly show the changes of increasing ozone levels.

Comparing the spectra in Figure 3.2a and 3.2b shows little change, but on close inspection there is a decrease in the TOA reflectance between 300-400nm, and another decrease at 500-700nm with increasing ozone concentration. This is shown clearly in Figure 3.2c. This shows that the reduction in reflectance between 300-400nm is the largest which is in the Hartley-Huggins absorption bands, peaking at a reduction of 0.22 at 310nm. There is also another broader feature in Figure 3.2c which shows a reduction in the reflectance between 450-750nm. This peaks at around 550-600nm with a reduction of 0.025 in the reflectance. This feature is in the region of the Chappuis ozone absorption band which is a weaker feature compared to the Hartley-Huggins band, and so it is expected that the response in this spectral region would be smaller.

It is also possible to compare these responses to the accuracy of TRUTHS. TRUTHS will have 0.3% uncertainty in the reflected solar radiation, which is equivalent to $6x10^{-4}$ reflectance units (Feldman et al., (2011)(b)). This means that for the change to be detected, it must be larger than $6x10^{-4}$. In the ozone case, the changes due to an increase in ozone are sufficiently large that they would be detected by a TRUTHS-like satellite.

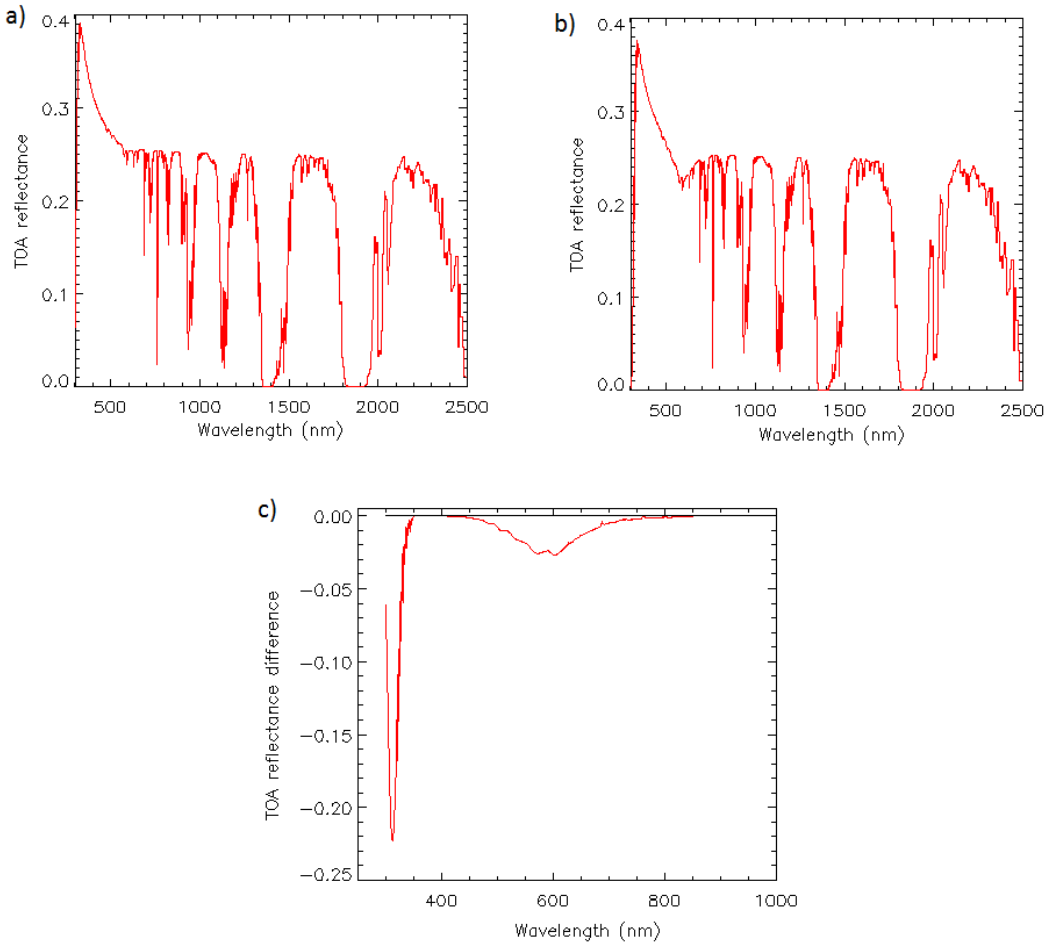


FIGURE 3.2: a) TOA nadir reflectance spectra for US Standard atmosphere, with 100DU of ozone, b) the same as a) with 500DU of ozone, c) the 550DU reflectance minus the 100DU reflectance. Note the change in scale of the x-axis.

Aerosols

The second round of sensitivity studies conducted looked at the effect of aerosols. The default aerosol is based on Shettle, (1989), and must be invoked in libRadtran in order to run the model with any aerosol. The sensitivity studies were run with two contrasting aerosol types as provided by libRadtran; urban and desert. The aerosol optical depth was set to 0.1 at 550nm for both aerosol types.

Figure 3.3a shows the difference between the TOA reflectances for the urban case and the pristine atmosphere with the default surface albedo of 0.25. The same information is shown in Figure 3.3b for the desert case. In both cases, the reflectance is reduced

with the addition of aerosol. In Figure 3.3a, the reduction in the reflectance peaks at 0.016 at 350nm which, compared to the pristine reflectance, is a decrease of 4%. The reduction in the reflectance due to the urban aerosol is spread across the spectrum (with exceptions due to strong molecular absorption bands), however, in Figure 3.3b the reduction in reflectance is predominantly between 300-700nm. Figure 3.3b shows that the reduction in reflectance peaks at 0.012 at 350nm.

The changes in Figure 3.3a due to an urban aerosol would be easily detectable by TRUTHS. However, the changes in Figure 3.3b due to desert aerosol are smaller in places. For example, between 800-2000nm the changes are too small to be detected by TRUTHS. The changes outside of this wavelength range would be detected, though, so the addition of desert aerosol would be detectable in some way.

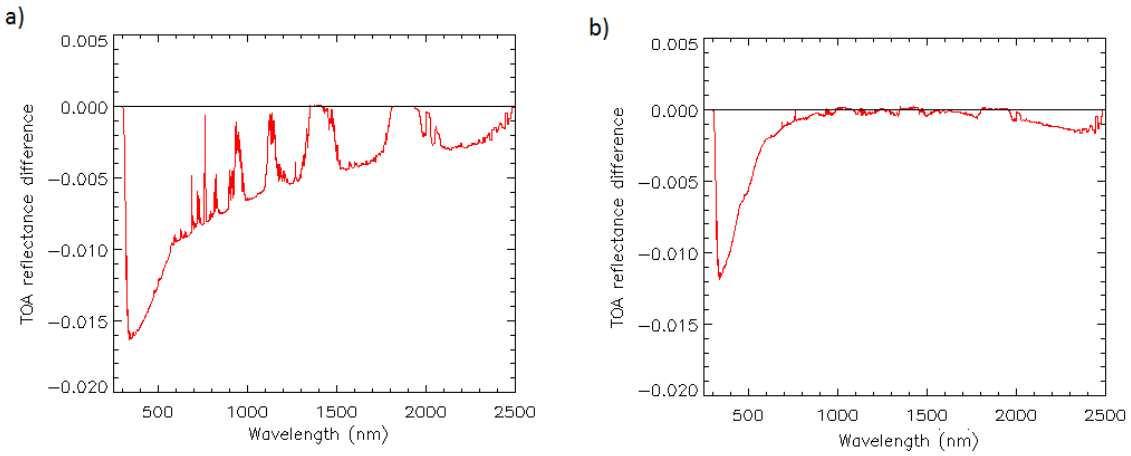


FIGURE 3.3: a) Difference between the TOA nadir reflectances for a pristine atmosphere, and the same atmosphere with urban aerosols over a surface of albedo 0.25, b) the same as (a) for desert aerosols. In both cases the pristine spectrum is subtracted from the polluted spectrum.

The TOA reflectance has been reduced in this case due to the fact that the aerosol has absorbed radiation, rather than reflecting it. This is due to the fact that the aerosol has been placed over a relatively bright surface. As discussed in Chapter 2, both aerosol types contain insoluble and water soluble constituents and soot, however, desert aerosols also contains dust in much larger concentrations than any of the aforementioned constituents. The aerosol is appearing darker than the surface in both of these cases and

therefore absorbing radiation, causing a reduction in the TOA reflectance.

However, when the same aerosols are placed over a darker surface, e.g. ocean, the desert aerosol is brighter than the underlying surface over the majority of the spectrum. Conversely, while the urban aerosol shows a small brightening at wavelengths <1500nm, enhanced absorption is still seen at longer wavelengths.. This example is shown in Figures 3.4a and b, which are the same as Figure 3.3 but with a surface albedo of 0.05. Figure 3.4b shows that the increase in reflectance is larger with desert aerosol, peaking at 0.005. This is consistent with the composition of the aerosol which is predominantly comprised of mineral components and would be significantly more reflective than an ocean surface. The urban case, Figure 3.4a, shows that the increase in reflectance reaches 0.002 at 400nm and quickly tails off. The increase in reflectance is likely due to the insoluble and water soluble constituents of the aerosol, which may appear brighter than the ocean surface. However there is still soot in the aerosol, which will still be absorbing some of the radiation. This shows that not only is the type of aerosol important, but the surface over which the aerosol is placed affects the TOA reflectance response. This was also shown in Patadia et al., (2009) which found that there was a threshold surface albedo of 0.35 for mineral aerosols such as desert dust. Above this 0.35 limit, the mineral dust is absorbing, whereas below this limit, the aerosol is reflecting.

Over a darker, ocean-like surface, since the changes in reflectance due to urban aerosols is smaller than in the previous case, this significantly affects the ability of TRUTHS to detect these changes. As the threshold for TRUTHS would be $6x10^{-4}$ reflectance units, it is clear to see from Figure 3.4a that the changes above 800nm would be undetectable. However, above the darker surface, the changes due to desert aerosol are larger and therefore now more easily detectable. It is discussed in Drury et al., (2008) that the ability to distinguish the aerosol from reflectance is easier over an ocean surface since the albedo is low and predictable. However, as pointed out in Kaufman et al., (1997), aerosol should be studied over land since the main sources of anthropogenic aerosols are on land and therefore is also the region with the largest radiative forcing. Therefore they conclude that studies should be conducted over darker land surfaces, such as soil

and vegetation which could be a way forward for this type of study.

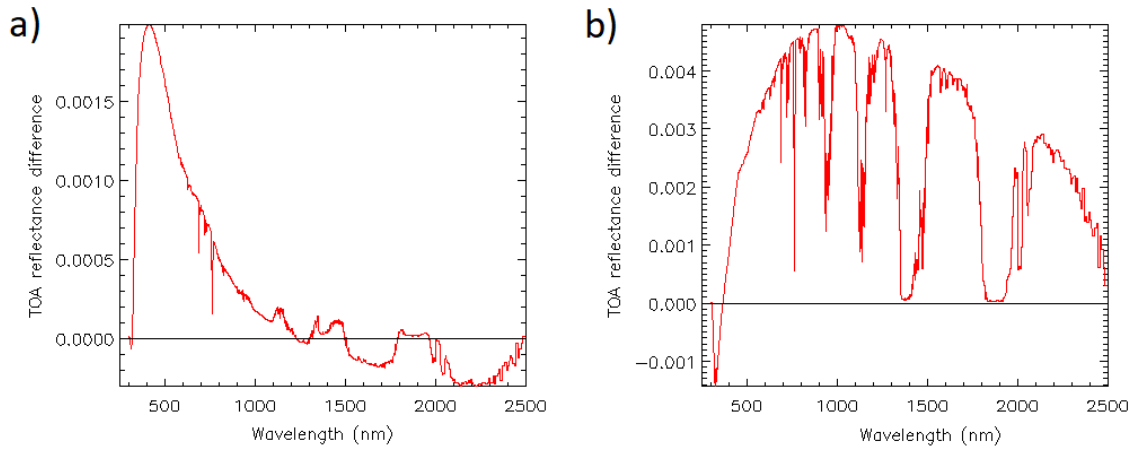


FIGURE 3.4: a) Difference between the TOA nadir reflectances for a pristine atmosphere, and the same atmosphere with urban aerosols over a surface of albedo 0.05, b) the same as (a) for desert aerosols. In both cases the pristine spectrum is subtracted from the polluted spectrum. Note the difference in the y-axis scales.

Albedo

For the albedo cases, various effects were investigated. Firstly, two different albedos were used for a Lambertian surface - at 0.05 to represent an ocean type surface (Payne, (1972)), and 0.25 to represent a grassy scene (Park, (2001)). In these cases, the albedos had no wavelength dependence. The second sensitivity studies used pre-set surfaces for a grass surface, a sand surface and an ocean surface. These albedos did contain a wavelength dependence. For both of these studies, the use of the US Standard Atmosphere was continued, as was the 30° SZA.

Firstly, comparing two Lambertian surfaces with albedos of 0.05 and 0.25 shows that, as expected, an increase in the surface albedo leads to an increase in the TOA nadir reflectance (not shown here). This is seen across all wavelengths due to the lack of the wavelength dependence in the albedo. The increase in reflectance due to an increase in albedo from 600nm onwards reaches nearly 0.2. The reflectance in this spectral region is approximately 0.05 with an albedo of 0.05, and increases to 0.25 with an albedo of

0.25 which shows that a five-fold increase in surface albedo leads to a five-fold increase in TOA nadir reflectance as expected.

Next, three different surface types were investigated; a grass surface, a sand surface and an ocean surface. These surface albedos were obtained from the ASTER Spectral Library Version 2.0 (Baldridge et al., (2009)) and are shown in Figure 3.5. Figure 3.5a shows the albedo spectrum for the sand surface. It is clear that the sand surface has the highest albedo of the surfaces as expected, reaching 0.8 at 800nm. There is a strong wavelength dependence, with several troughs in the spectrum - at 1450nm, 1950nm etc. - while the albedo dependence in the visible is relatively smooth.

Figure 3.5b shows the albedo spectrum for the grass surface. The main feature of this spectrum is the large peak in reflectance between 700-1450nm (after the red edge), with the albedo reaching 0.5. As in the sand albedo spectrum, there are two troughs at 1450nm and 1950nm. The most important feature, however, is at the visible wavelengths where the albedo is relatively low at 0.05, but there is a peak in the albedo at 550nm. This peak corresponds to the green wavelengths of light and the surface albedo doubles around this wavelength.

Finally, Figure 3.5c shows the albedo spectrum for the ocean surface. As expected, the albedo is very low at all wavelengths with a range of 0.016 to 0.03. The albedo gets smaller with increasing wavelength, but beyond this there is little wavelength dependence, with no marked features as in Figure 3.5a and b.

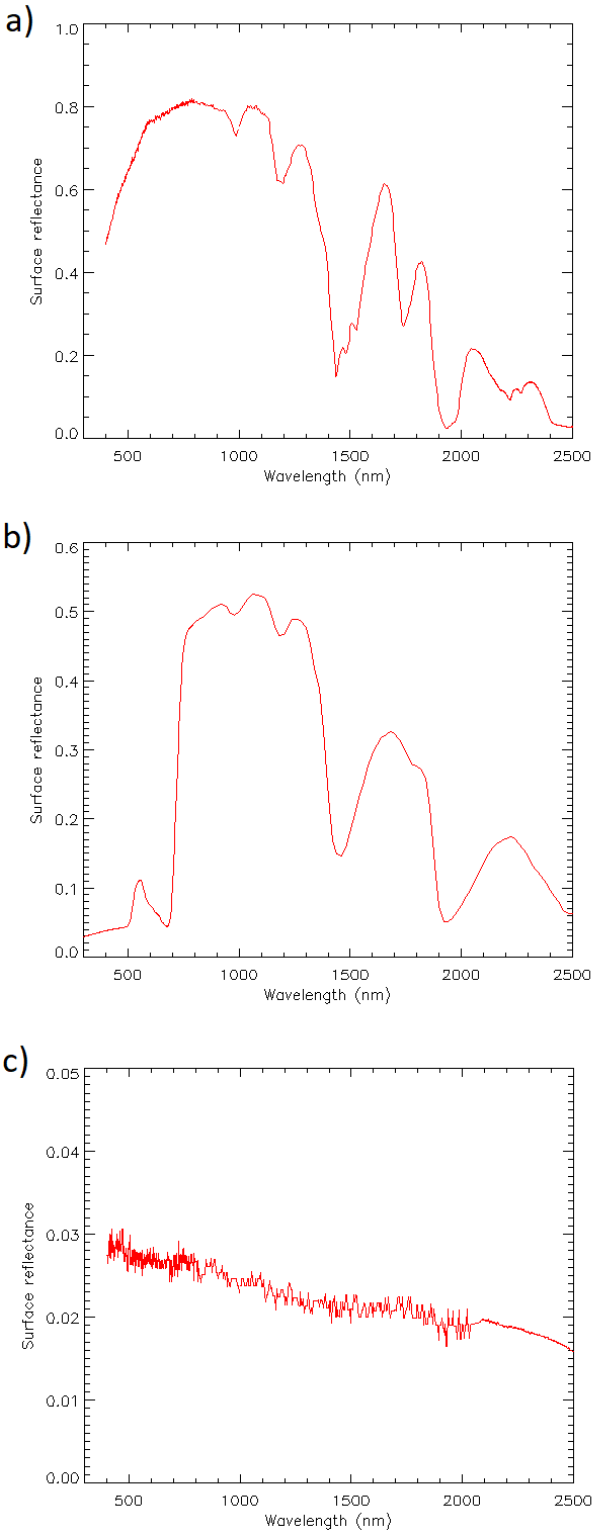


FIGURE 3.5: The surface albedo spectrum for a) a sand surface b) a grass surface, and c) an ocean surface. Note the different scales on each panel.

The plots in Figure 3.6 show the TOA nadir reflectance spectra for each of the surface types. Figure 3.6a shows the TOA spectrum for an environment with a sand surface. Comparing with the spectrally flat albedo of 0.25 in the previous studies, the TOA reflectance is lower between 300-400nm, and higher between 400-800nm for the sandy surface which agrees with the spectral variation of the surface. The reflectance at 2000-2500nm also matches the shape of the albedo in Figure 3.5a.

Figure 3.6b shows the effect on the TOA nadir reflectance of using the grass surface. There is a decrease in the TOA reflectance between 300-700nm which corresponds to the range for visible light. There is however, a feature at 500-600nm which shows a slightly larger reflectance. This region corresponds to the green portion of the visible range. This is due to the fact that grass reflects green light, while absorbing light in the other visible wavelengths. It is this reflection of the radiation at this wavelength range that causes an increase in the TOA reflectance. There is also a significant increase in the reflectance after 700nm - i.e. after the red edge. The red edge occurs between 680-750nm and is the boundary between where the chlorophyll is absorbing the red wavelengths of radiation, and where the reflectance of vegetation suddenly increases in the NIR due to scattering (Filella and Penuelas, (1994)).

Finally, Figure 3.6c shows the TOA reflectance spectrum over an ocean surface. As previously shown in Figure 3.5c, the surface albedo over the ocean is very low, and so it is expected that the TOA reflectance will also be low. The reflectance over an ocean surface peaks at 400nm at 0.15, but lies between 0.02-0.03 for most of the spectrum between 800-2500nm. The shape of the spectrum remains relatively intact compared to the original TOA reflectance seen in Figure 3.1. This is expected given the little spectral dependence exhibited in Figure 3.5c, whereas in the grass and sand examples, the shape of the reflectance spectrum very clearly matches that of the surface albedo.

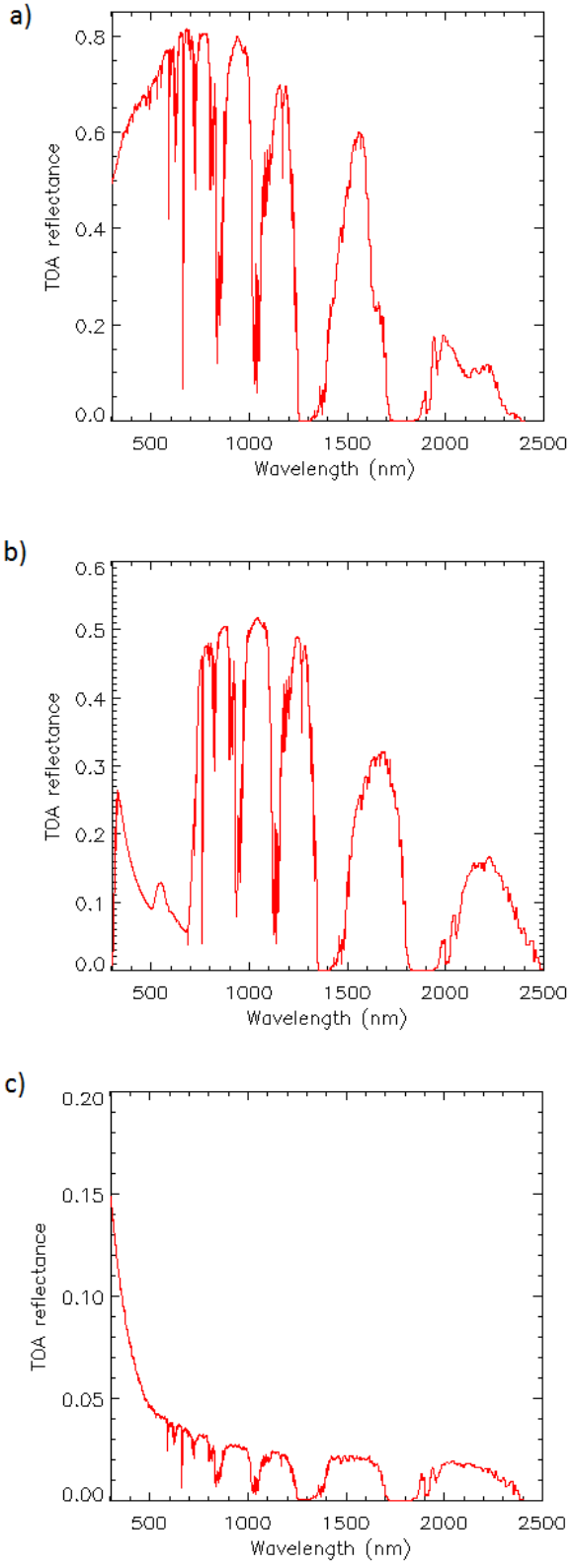


FIGURE 3.6: a) The TOA nadir reflectance spectrum for a sand surface b) the same as (a) for a grass surface, and c) the same as (a) for an ocean surface. Note the different reflectance scales on each panel.

Clouds

The next set of sensitivity studies conducted were for clouds and as before, these studies all used the default conditions. The first set of studies investigated the effect of an increase in cloud thickness. For this, a water cloud was specified between 2-3km, with the liquid water content (LWC) set at 1gm^{-3}, effective droplet radius (R_{eff}) of 10μm, and a cloud optical depth at 550nm (τ) of 5. The values for LWC and R_{eff} used are the default values within libRadtran for a water cloud. For comparison, a second study was run with a geometrically thicker cloud extending from 2-4km.

Given that one of the interests of this study is how the cloud interacts with the incident shortwave radiation, it is important to also understand how the physical properties of the cloud relate to their optical properties. While the optical depth of the cloud at 550nm is set at 5, it is possible to calculate the single scattering albedo (SSA) and the asymmetry parameter, g, within libRadtran based on the wavelength and effective radius of the droplets. As stated above, the R_{eff} is 10μm which leads to a SSA of 0.9999 at 500nm. This means that almost all of the radiation at this wavelength is scattered as opposed to being absorbed by the cloud droplets. The asymmetry parameter at 550nm, for droplets of R_{eff} = 10μm, is 0.8701. This means that the radiation is mostly forward scattered by the particles - a value of 1 meaning all radiation is forward scattered.

The difference between the TOA nadir reflectances for these two cases are shown in Figure 3.7a. This figure shows that there is an increase in TOA reflectance with a geometrically thicker cloud and these increases are occurring in the water vapour absorption bands (such as 940nm and 1375nm). This is due to the increase in the number of cloud droplets causing an increase in back scattered radiation to the TOA. These increases are very small relatively, reaching 0.009 at 1800nm, with almost no change in the visible wavelengths.

The second study investigated the effect of changing the height of the cloud. For this, the same cloud parameters were chosen and the cloud was placed at 2-3km, and then 3-4km, to compare the TOA nadir reflectance spectra. This difference can be seen in

Figure 3.7b. As before, there is an increase in reflectance when the cloud is raised from 2-3km to 3-4km, and these increases in the reflectance also occur in the water vapour bands. This is due to the scattering of the radiation by the cloud particles occurring sooner and higher in the atmosphere, before the radiation has been scattered and absorbed further. The radiation also has less distance to travel to reach the TOA, and undergoes less attenuation than the radiation reflected from the lower cloud. This increase in reflectance, however, is three times that in Figure 3.7a, reaching 0.03. This equates to an increase of 12.5% due to a change in cloud height. While all of these changes are relatively small, they would still be detected by TRUTHS.

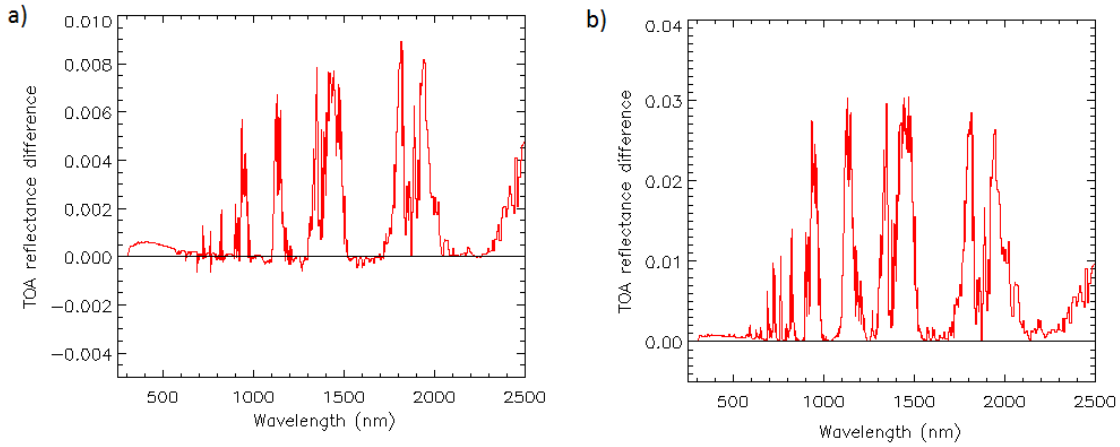


FIGURE 3.7: a) Difference in TOA reflectance spectra between an atmosphere with a water cloud at 2-3km and 2-4km (2km thickness - 1km thickness), b) difference in TOA reflectance spectra between an atmosphere with a water cloud at 2-3km and 3-4km (3-4km cloud - 2-3km cloud). Note the difference in the scales.

The next study was to investigate the effect of the LWC and R_{eff} on the TOA nadir reflectance. These studies were carried out with the same atmosphere, and with the cloud at 2-3km. In the first study, the effective radius of the cloud droplets was adjusted from 10 to 15 microns. This value is in accordance with Stubenrauch et al., (2013) which states that the global average for water droplet radii are 14 ± 1 microns. Figure 3.8 shows the effect of increasing R_{eff}. By increasing the droplet radius, the TOA reflectance decreases. Larger particles have a larger absorption cross section and so more radiation is absorbed by the cloud droplets, which reduces the reflectance.

Finally, the LWC was changed from 1gm^{-3} to 0.5gm^{-3} based on average LWC as discussed in Wallace and Hobbs, (2006). Changing these values result in zero change in the TOA reflectance. This is due to the fact that the optical depth of the cloud is relatively large and so varying the LWC of the cloud has no further effect on the radiation, and therefore the TOA nadir reflectance.

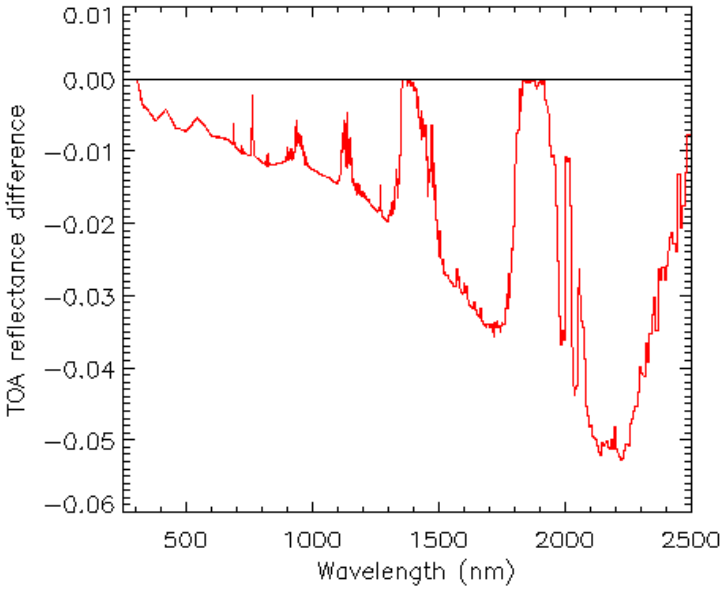


FIGURE 3.8: Difference in TOA nadir reflectance between clouds with droplet radii 10 and 15 microns (15 - 10 μm).

The next studies conducted were for ice clouds and used an ice water content (IWC) of 0.01gm^{-3} and R_{eff} of 20 microns, which are the default settings in libRadtran. The clouds also had a τ at 550nm of 5. For the initial runs, the cloud was placed at 10-11km, and then a geometrically thicker cloud at 10-12km, with the same optical depth, R_{eff} and IWC through the whole extent. Then a cloud was placed at 11-12km to investigate if the vertical location has an effect on the TOA nadir reflectance. As before, the SSA and asymmetry parameters were calculated for these clouds at 550nm, and were 0.9999 and 0.9018 respectively. As in the water cloud, the radiation is almost entirely scattered by the particles, and the ice particles are marginally more forward scattering than the water cloud particles.

The results of these sensitivity studies are shown in Figure 3.9. Figure 3.9a shows the difference in TOA nadir reflectance spectra due to an increased thickness of the above cloud, from 10-11km to 10-12km. While there is a difference between the spectra, it is relatively small. The peaks, as in the water cloud example, are in the water vapour absorption bands and the increase in reflectance is due to there being more particles to scatter radiation, resulting in more radiation scattered back towards the TOA. However, compared to the water cloud example, the difference in the reflectance is smaller. The difference is most significant in the two furthest bands at 1390nm and 1900nm, though small changes can be seen in the 940nm band, and at 1125nm. The changes around 1390nm and 1900nm are the only features that would be detected by TRUTHS since the other changes are too small, and less than the 6x10^{-4} threshold.

Figure 3.9b shows the difference in the TOA due to raising a cloud from 10-11km to 11-12km. In this case, the TOA nadir reflection also increases but by a larger amount than in Figure 3.9a, which means these changes are now detectable by a TRUTHS-like satellite. As in Figure 3.9a, and as in the water cloud example, the increases in the reflectance are in the water vapour bands, and are for the same reasons as in the water cloud case.

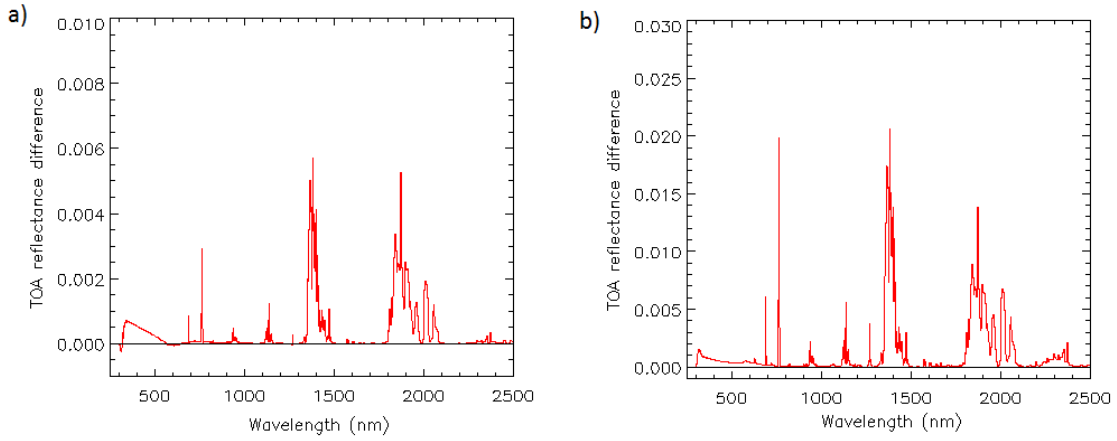


FIGURE 3.9: a) Difference in TOA nadir reflectance between an ice cloud at 10-11km and 10-12km (2km cloud - 1km cloud), b) and the difference in TOA nadir reflectance between an ice cloud at 10-11km and 11-12km (11-12km cloud - 10-11km cloud).

The final sensitivity study investigated the effect of the R_{eff} and the IWC on the TOA

nadir reflectance spectrum. Figure 3.10 shows the difference in the TOA reflectance spectra when the R_{eff} is increased from 20 microns to 25 microns (based on Stubenrauch et al., (2013) which states a global average R_{eff} for ice clouds as 25 microns). It is clear that the TOA reflectance decreases with the increase in the R_{eff} of the ice particles, peaking at a decrease of 0.03 at 1500nm. Between 300-1400nm, the decrease in the reflectance is steady, ranging from 0.005 to 0.01, but then suddenly increases in magnitude at 1400nm. In order to understand the shape of the change in the TOA reflectance, the asymmetry parameters and SSA for the surrounding wavelengths were calculated for both R_{eff}. While the asymmetry parameter for the 20μm R_{eff} varies steadily, for the 25μm case the asymmetry parameter changes from 0.805 to 0.828 at 1410nm. This shows that there is an increase in forward scattering by the larger cloud particles at this wavelength. The SSA for the 20μm particles also reduces steadily over this wavelength region, but for the larger particles drops dramatically from 0.996 to 0.93 also at 1410nm. This shows that there is more absorption after 1410nm by the 25μm particles. It is a combination of these two effects that means the TOA nadir reflectance spectrum is significantly lower in this wavelength range.

In both water and ice cloud scenarios, changing the R_{eff} leads to large changes in the TOA reflectancs which would be easily detectable by TRUTHS.

Finally, the IWC of the cloud was varied from 0.01gm^{-3} to 0.05gm^{-3}. This value was chosen based on Protat et al., (2007), and 0.05gm^{-3} is within the range of what is described in Protat et al., (2007) as an intermediate IWC. Comparing these results, the change in the TOA nadir reflectance spectrum was of the order 10^{-7}, which certainly would not be detectable. Again, the optical depth of the cloud is relatively large, and so variations in the LWC has a negligible effect.

In order to explicitly compare the effects of water and ice clouds on the TOA nadir reflectance, two cases were run with the same τ of 5 as before, and R_{eff} and LWC/IWC. Both ice and water clouds had a R_{eff} of 15 microns and LWC/IWC of 0.2gm^{-3} based on values from Wallace and Hobbs, (2006). The clouds were also placed at 8-9km. Figure 3.11 shows the TOA nadir reflectance spectra for the water cloud example and

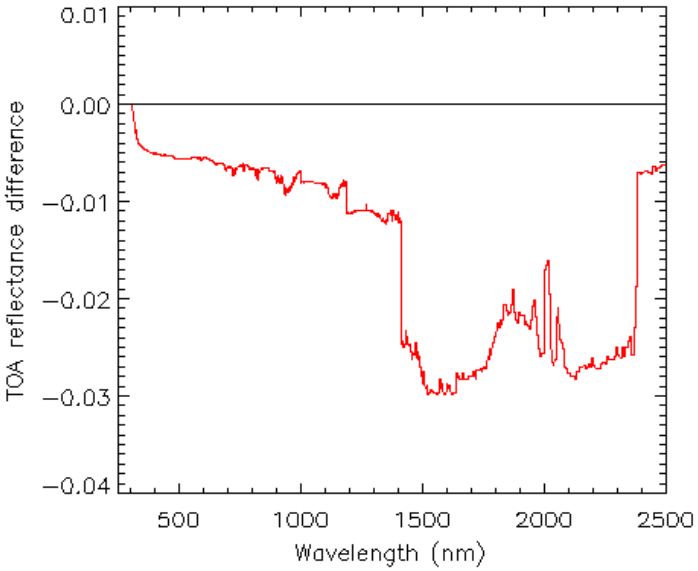


FIGURE 3.10: Difference in TOA nadir reflectance between ice clouds with R_{eff} 20 microns and 25 microns (25 - 20 microns).

the ice cloud example.

It can be seen that the ice cloud results in a higher TOA reflectance than the water cloud at most wavelengths, except for the region of 1500-1750nm, where the water cloud reflectance is higher. As discussed in Chapter 2, 1600 and 1680nm are used to discriminate between water and ice clouds. Figure 3.11 shows that, when compared to other wavelengths, 1600/1680nm would be able to help distinguish between the existence of ice and water clouds when looking at the TOA reflectance.

The effect of clouds on the TOA reflectance has been researched by Palle et al., (2004) who looked at the changes in Earth's reflectance over the last 20 years, with respect to cloud amounts and properties. They concluded that clouds have a larger effect in the visible wavelengths rather than in the UV or near IR. This is since ozone absorption and strong Rayleigh scattering, and absorption by water vapour and CO_2 limit the effect at the impact of clouds in the respective wavelength ranges. Palle et al., (2004) do, however, explore changing cloud over several years rather than the effects due to specific properties as examined here. However, it is very possible that these types of

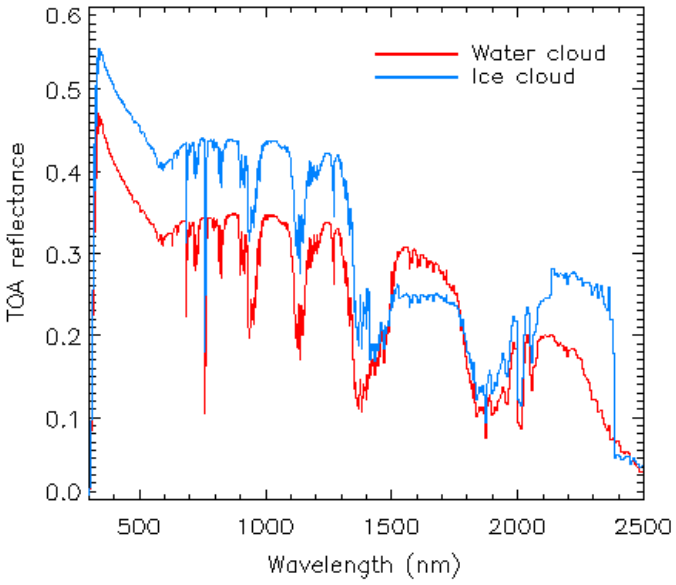


FIGURE 3.11: TOA nadir reflectance spectra for an atmosphere with a water cloud (red line) and with an ice cloud (blue line).

changes may be seen in the reflectance spectra from TRUTHS.

3.2 Polar Sensitivity Studies

So far, these sensitivity studies have only considered the general effects of atmospheric and surface conditions in a standard atmosphere. In this section, the focus is on the polar regions, and the specific conditions found there. As discussed later in Chapter 4, COSSE data show high levels of noise and variability in these areas and so sensitivity studies were carried out to investigate the factors affecting these regions. In the Arctic, the surface ranges from one extreme to the other; winter with mostly sea ice and snow cover, to the summer when the snow and ice melt, causing the albedo to dramatically drop to that of an ocean surface. The poles are also in darkness for half of the year, and during the summertime, the sun does not reach a high elevation in the sky as in other regions. It is for these reasons that the surface albedo and SZA were investigated, as well as the effect of clouds.

The sensitivity studies in this section were carried out using libRadtran and for the

purposes of this study, uvspec was set to use the 'subarctic summer' atmosphere, as defined by Anderson et al., (1986). These studies were carried out for selected wavelengths; 550nm, 940nm, and 2190nm. The two wavelengths at 550nm and 2190nm were chosen since they are relatively transparent and also show significant differences in snow surface albedo (as shown in Figure 3.12). Finally, 940nm was chosen as it is a water vapour absorption channel. The variables chosen to be studied are key parameters that affect TOA shortwave radiation – surface albedo, solar zenith angle (SZA), and the cloud optical depth. The values for these variables are provided in Table 3.1, which are based on values provided in various publications (Curry et al., (1996), Jin et al., (2007), Dong et al., (2010), Liu et al., (2012) and Wang et al., (2000)). The clouds used in the simulations were kept constant with a cloud base height of 1km and extended to 2km. The cloud properties were chosen based on papers by Curry et al., (1996) and Jin et al., (2007) as representative of summertime clouds in the arctic. The cloud optical depths are set at 550nm and vary with wavelength, using the parameterisation of Hu and Stamnes, (1993).

SZA	40	50	60	70
Cloud optical depth, τ_{550nm}	2	4	6	8
Surface albedo, α	0.1	0.2	0.3	0.4
	0.5	0.6	0.7	0.8
	0.9			

TABLE 3.1: Values of SZA, cloud optical depth at 550nm, and surface albedo used in simulations

The range of surface albedos was used to cover the whole range of possible albedos in the Arctic – from the high albedos of ice and snow, to the lower albedos of water for the ocean. Also, the real surface albedo varies with wavelength and SZA (Wiscombe and Warren, (1980)). It can be seen in Figure 3.12 that for 550nm and 940nm the surface albedo is high at 0.7-0.9, however, at the third wavelength of 2190nm the albedo is very low, between 0.05-0.15 (depending on the solar zenith angle). This means that for 550nm and 940nm, the focus was on the larger half of the range at 0.5-0.9 albedo, and for 2190nm the focus was for 0.1-0.5 in order to maintain realistic and representative surface albedos. An albedo of 0.5 was the mid-point of the range used and therefore was chosen as the limit between the two regimes.

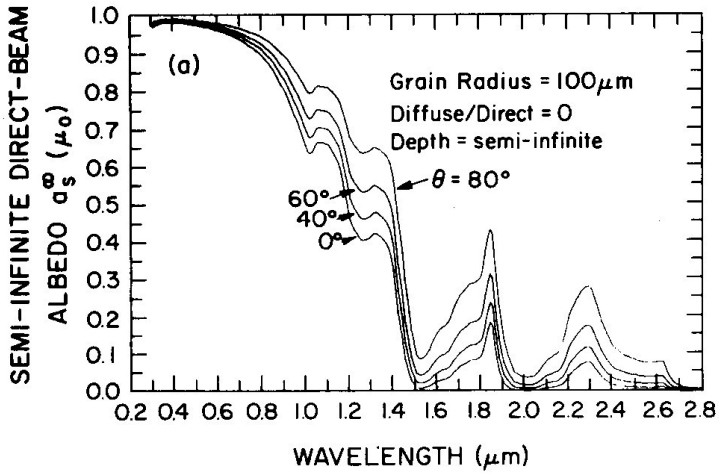


FIGURE 3.12: Variation of albedo with wavelengths 0.2-2.8μm on a snow covered surface, and with SZA. From (Wiscombe and Warren, (1980)), ©American Meteorological Society. Used with permission.

The initial simulations were performed in order to compare the values produced by libRadtran with realistic values for each of the three wavelengths. In order to do this, reflectances were calculated from the libRadtran simulation data and compared to the reflectances from the COSSE data introduced in Chapter 2. This was to ensure that the values output by libRadtran were similar to those in the COSSEs. COSSE output was taken for the summer months (averages across June, July, August for the 100 year data set) in the Arctic (66-90°N) and for the 3 wavelengths being used. There is expected to be some difference between the libRadtran simulations and COSSE values since there are several unknowns about the COSSE data, such as what the surface albedo is, how it changes with wavelength, and also how the atmosphere differs from the subarctic summer atmosphere used in libRadtran. Figure 3.13 shows global reflectance maps for the COSSE data at each wavelength considered, for the clear sky case. It is clear to see when looking at the polar regions, how the TOA reflectance varies with wavelength. Comparing the reflectances at 940nm and 2190nm, the reflectances are similar at around 0-0.17, however at 940nm there is a peak in the reflectance over Greenland. This peak reaches a reflectance value of 0.454. Greenland, even in summer, has a permanent covering of snow over most of the inland area, whereas at the North Pole in the summer, a majority of the ice and snow have melted away, causing a lower albedo. This can be seen in the 550nm example where Greenland also shows a higher reflectance than the rest of the Arctic. The clear sky values produced by libRadtran do

fall within the ranges of the equivalent values seen in the COSSE data in Figure 3.13, and so this gives confidence that the simulations performed are adequate to investigate the variability in the Arctic due to variations in surface albedo.

As in Section 3.1, it is important to understand the optical properties of the clouds. In this case, the cloud droplets are set at 7 microns in radius based on standard values discussed in Curry et al., (1996) and Jin et al., (2007). Table 3.2 shows the values obtained for the SSA and asymmetry parameters.

Parameters	550nm	940nm	2190nm
Single Scattering Albedo, SSA	0.999999	0.999938	0.975867
Asymmetry parameter, g	0.8579	0.8466	0.8169

TABLE 3.2: The values of the single scattering albedo and asymmetry parameter of the cloud input into the atmosphere in libRadtran

It is interesting to note that the SSA is effectively 1 for 550nm and 940nm. This means that a negligible proportion of radiation is absorbed by the cloud, providing 100% scattering at these wavelengths. Even the value at 2190nm is high, with little absorption occurring. The asymmetry parameter shows that the cloud droplets are mostly forward scattering in all cases with the values being nearer 1 (all forward scattering) than zero (isotropic).

Varying the effective radius of the droplets changes the values of the SSA and asymmetry parameter and also changes the spectral distribution of the optical depth. At 550nm, whether the radius is 2.5 or 60 microns (the limits within libRadtran), the SSA only changes by miniscule amounts and remains approximately 1. At 30 microns (the middle of the range), the SSA at 940nm decreases only to 0.99975, however, the SSA for 2190nm decreases to 0.91297 – a fairly significant change. At this wavelength increasing the droplet size increases the amount of radiation absorbed by the particles, and reduces the proportion of scattering. This can be explained by the fact that the incident radiation will interact more with the particles as it is taking longer to travel through the particle, increasing the likelihood of absorption. The asymmetry parameter also varies with the effective radius but in the opposite direction – at 550nm, increasing the radius

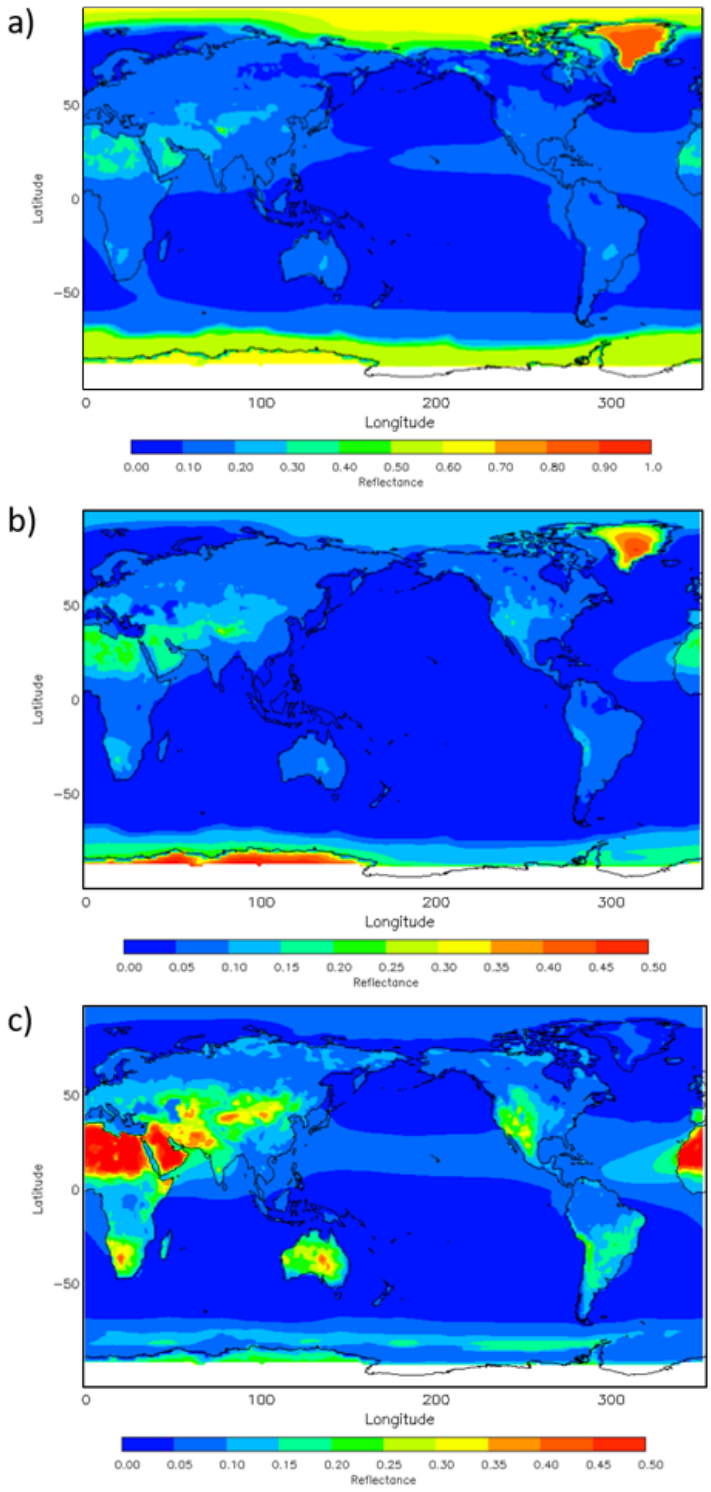


FIGURE 3.13: Global top of atmosphere reflectance maps at 1.41°x1.41° resolution, based on the COSSE data from Feldman et al., (2011)(b), for each wavelength. The Arctic region is considered to comprise of latitudes of 66°N and above. a) shows the map for 550nm, b) the map for 940nm and c) the map for 2190nm. Note the difference in scale between panels.

of the droplets increases g. For example, at 2.5 microns, g = 0.8244 and then by 60 microns, g reaches 0.8803. The asymmetry parameter increases with the radius because the intensity of the scattering is proportional to the size of the particles. Calculating the optical properties of the cloud in these simulations provides important information about the cloud behaviour and can aid the understanding and quantification of the radiation-cloud interactions in the simulations.

3.2.1 Results

In these simulations, the values calculated are the direct downwelling flux, the diffuse downwelling flux, and the diffuse upwelling flux. These values are output at each atmospheric level which covers 0-120km at predefined intervals discussed in Chapter 2. For this study, the focus will be on the region from 0-5km which is where the greatest change occurs to the fluxes, due to the location of the cloud layers. In this range, the levels are at a 1km separation, and as before, the cloud is between 1-2km altitude. Here, only the 'extreme' cases will be shown, i.e. the cases with the lowest and highest values of the variables. This is because examining the two extremes of the set of variables will encompass the whole range of the associated flux changes. However, every permutation of the variables listed in Table 3.1 has been simulated.

Figure 3.14 shows an example of one set of flux data obtained from libRadtran, for a wavelength of 550nm, SZA of 40° and cloud optical depth of 2. The only difference between the two panels is the surface albedo - Figure 3.14a shows the case with an albedo of 0.5, and Figure 3.14b shows the case with the albedo increased to 0.9. It is clear in both figures that the direct downwelling flux is dramatically reduced upon interaction with the cloud, from 1250 $\mathrm{mWm^{-2}nm^{-1}}$ to 100 $\mathrm{mWm^{-2}nm^{-1}}$. This coincides with an increase in the diffuse downwelling flux – the direct beam interacts with the cloud and is mostly forward scattered (g = 0.86) towards the surface, with a small amount scattered in other directions. As seen from the SSA in Table 3.2, the cloud is almost entirely scattering and so negligible radiation is absorbed by the cloud. Some of the radiation is reflected off the cloud top towards space. It can be seen in Figure 3.14b that the diffuse downwelling flux is larger at the surface compared to Figure

3.14a (1350 $mWm^{-2}nm^{-1}$ versus 1175 $mWm^{-2}nm^{-1}$). This is due to the increase in surface albedo. At 0.5 albedo, only 50% of the flux incident on the surface is reflected back towards space, however at 0.9 albedo this value is 90%, this increases the amount of radiation available for reflection back off the cloud base towards the surface. This increases the diffuse downwelling flux at the surface with these multiple scatterings occurring several times. The upwelling flux above the cloud layer is a combination of the reflected solar flux from the cloud top and the proportion of the upward diffuse fluxes and downward diffuse fluxes which are forward and back scattered by the cloud respectively. This is why in Figure 3.14a the diffuse upwelling flux increases by 100 $mWm^{-2}nm^{-1}$ above the cloud layer compared to what is reflected from the surface. However, this is different in Figure 3.14b, with the upwelling flux above the cloud layer less than the upwelling flux from the surface. This shows that the cloud will actually have a dimming effect on the TOA albedo compared to the equivalent clear sky conditions as it appears less bright than the underlying, high albedo surface. Figure 3.15 provides a schematic representation of the various interactions described above for the α = 0.5 case.

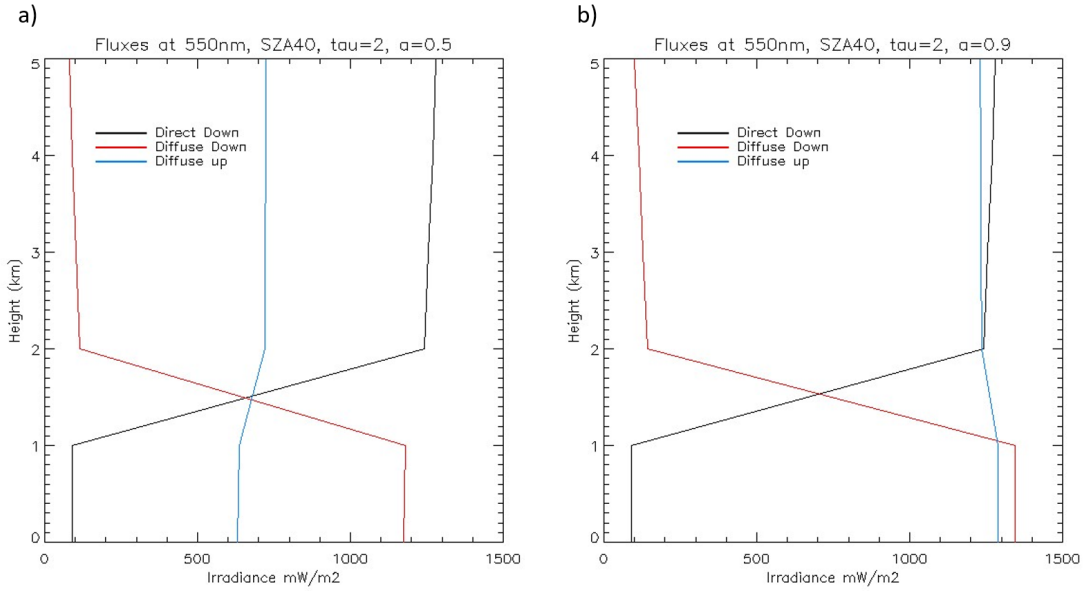


FIGURE 3.14: Flux profiles from 5km altitude to the surface for 550nm. a) SZA 40°, τ = 2, α = 0.5. b) is for the same case at α 0.9. Each line shows how the direct downwelling, diffuse downwelling and diffuse upwelling fluxes change with altitude above and below a cloud layer at 1-2km.

Comparing across the wavelengths, the magnitude of the fluxes decrease with increasing wavelength which is expected given the shape of the curves in Figure 1.2 – with a peak in radiation in the visible, and the magnitude of the flux tailing off by 940nm and then further at 2190nm. The flux profiles follow similar shapes for both 550nm and 2190nm however 940nm displays steep gradients showing decreasing flux as the radiation travels through the atmosphere, as opposed to the nearly vertical lines in Figure 3.14. These are due to the fact that 940nm is in a water vapour absorption band and so the radiation decreases as it travels through the atmosphere due to absorption by water molecules (not shown). An increase in albedo gives similar results at all wavelengths.

Figure 3.16 shows schematically how the interactions at 550nm change with an increase in cloud optical depth, all other parameters being set to the same values as in Figure 3.15. Increasing the optical depth from 2 to 8 decreases the direct downwelling radiation at the surface to a negligible amount (0.036 $\mathrm{Wm^{-2}nm^{-1}}$). Even though the cloud droplets predominantly forward scatter radiation, in an optically thicker cloud there is a larger number of scattering events, and so the beam can change direction more easily, and eventually get scattered back to space. A portion is still forward scattered through to the surface. As less radiation is transmitted through the cloud and more is reflected from the cloud top, the difference in the upwelling flux below and above the cloud is larger for the case with increased cloud optical depth. The diffuse downwards irradiance reaching the surface is also reduced in the high τ case due to the enhanced multiple scattering.

The final variable to explore is the solar zenith angle. Fundamentally, increasing the SZA from 40° to 70° decreases the incoming solar flux. At every wavelength considered, the incoming solar radiation decreases by over half (56-62%). This is because the radiation is travelling at a shallower angle through the atmosphere and is therefore traversing more atmosphere and being attenuated due to more absorption and more scattering. The other main feature in most of these cases is that the increase in the upwelling flux from below to above the cloud layer increases with increasing SZA. This can be explained by the fact that at a higher SZA the radiation is more easily scattered

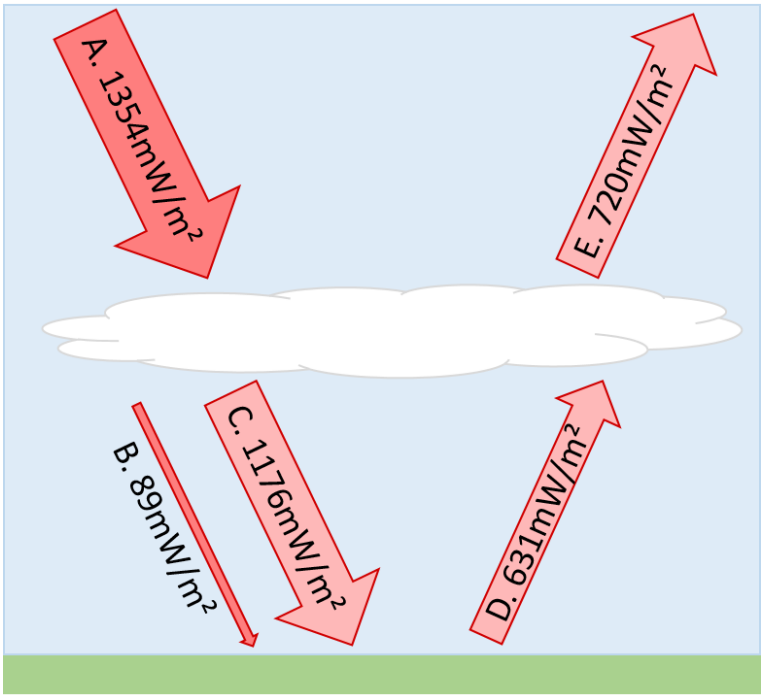


FIGURE 3.15: Schematic of the interactions between the radiation, the cloud and the surface for the cloud with τ=2, at 550nm, 40° SZA, and α = 0.5. Values from corresponding simulation. A. Direct downwards irradiance at cloud top, B. Direct downwards irradiance at surface, C. Diffuse downwards irradiance at surface, D. Diffuse upwards irradiance at surface, E. Diffuse upwards irradiance at cloud top.

upwards from the cloud layer.

Though only a single cloud layer scenario has been simulated, it is clear that SZA, surface albedo and cloud optical depth have significant and complex effects on SW fluxes and hence TOA radiation in conditions chosen to broadly represent polar environments. These effects also strongly depend on the wavelength considered due to the variations in surface albedo (Figure 3.13, and Figure 3.12) and the cloud optical properties (Table 3.2). Clouds are also very complex systems, and the one simple cloud layer in these simulations is unlikely to be what would occur in real life – Curry et al., (1996) discuss the 'frequently observed' multilayer clouds during the Arctic summertime. A mixture of cloud types, heights, optical properties would add complexity. The combination of these complex clouds with the ice growth and melt seen in the region are likely the reason for the high variability and noise seen in the polar regions in the COSSE simulations in the next chapter.

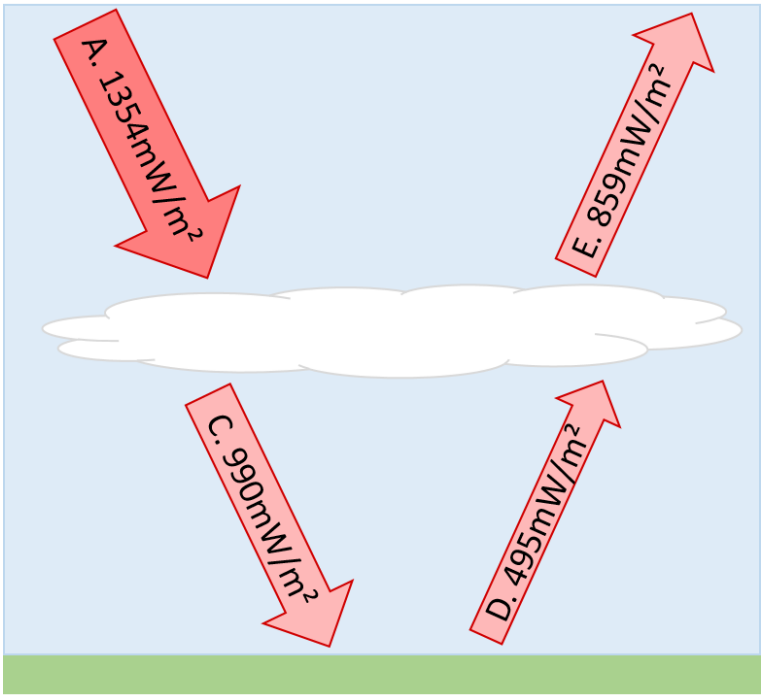


FIGURE 3.16: Schematic showing the interactions between the radiation, the cloud and the surface for an optically thicker cloud (τ=8 case), at 550nm, 40° SZA, and α = 0.5. Values from corresponding simulation. Arrow labels as before; note there is no direct downwards irradiance at the surface in this case.

3.3 Water Vapour Sensitivity Study

It is known that water vapour absorbs shortwave radiation at certain wavelengths, as seen in Figure 1.2. The sensitivity studies described here were run to investigate the effect of increasing water vapour on the TOA reflectance at 940nm, which is a well known water vapour absorption band. The investigation was also run for two different surface types; ocean and land. Simulating the changes over two different surface types provides more information as to whether water vapour absorption is expected to have a larger effect over land or ocean, something observed in the COSSE simulations in Chapter 4.

This study was conducted using a standard tropical atmosphere (from Anderson et al., (1986)), using a spectrally constant albedo of 0.05 to represent the ocean, and 0.25 to represent the land, consistent with Section 3.1. The column water vapour was then varied from 25-50mm based on a variety of factors. The global average column water vapour is approximately 25mm, with a full range of 0.03-75mm (Martin, (2014)). The

tropics have higher levels of water vapour as expected, with an average of 35mm as stated in Myers, (2013). Therefore the range was chosen to encompass the tropics average, with the global average as the lowest limit, and 50mm chosen as the upper limit so as not to reach the extremes of global water vapour levels mentioned above. As before, in order to convert the results into TOA nadir reflectances, the TOA radiances were output from libRadtran.

3.3.1 Results

Figure 3.17 shows the results from these sensitivity studies. This figure shows the TOA nadir reflectances at 940nm, for increasing water vapour. The black line shows the results over land, and the blue line shows the results over the ocean surface. The reflectance over land changes significantly from 0.067 to 0.032, compared to over ocean, where the reflectance decreases from 0.016 to 0.008. While this shows that for both cases the fractional changes in the TOA reflectance is the same, with both reflectances reducing by 50%, it is the absolute change that is important. Since the land surface albedo is typically higher, the TOA reflectance is also higher in the first place (Figure 3.14b), and so an increase in water vapour causes a larger absolute change in the TOA reflectance. In the ocean case, the albedo is a lot lower and so a much larger amount of the radiation is absorbed. This means that the addition of water vapour makes relatively little difference to the amount of radiation reaching TOA, since the value reflected from the surface is already low.

3.4 Summary

In conclusion, a wide range of sensitivity studies were carried out in order to gain an understanding of the factors that affect the shortwave radiation, and to what extent. These sensitivity studies focussed on a variety of factors including ozone, aerosols, surface albedo, SZA and cloud. The SZA was investigated to confirm the expected results before moving onto the rest of the sensitivity studies.

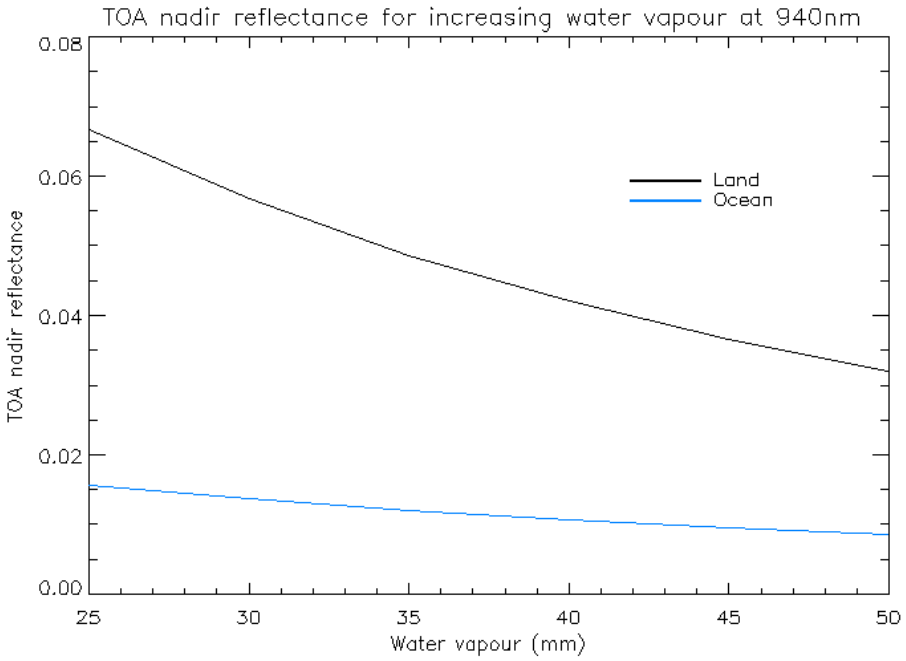


FIGURE 3.17: TOA nadir reflectances at 940nm over land and ocean surfaces, for increasing atmospheric water vapour.

Varying the ozone over a substantial range has a relatively small effect on the TOA reflectance, and this effect is concentrated in the ozone absorption bands at 300nm and 500-700nm (Hartley-Huggins and Chappuis bands respectively). The two different aerosols considered here both cause an effect smaller than the effect of ozone, though the AOD chosen in these studies is relatively low and the effects could be much larger in various regions. The aerosol studies show the effect of not only the aerosol type, but also the effect of the underlying surface on the TOA reflectance. It was shown that dust aerosols have a much larger effect on the reflectance when over a darker surface, as the dust reflects the radiation. Whereas the urban aerosol results in significant absorption of radiation over the brighter surface, due to the soot that comprises the aerosol.

Varying the albedo of a Lambertian surface (from 0.05 to 0.25 here) naturally has a linear relationship with the TOA reflectance as expected. However, by using a spectrally dependent surface albedo different changes are observed. Using the grassy scene albedo significantly reduces the TOA reflectance in the visible wavelengths, apart from

at green wavelengths. There is also a significant increase of almost double the reflectance from 700-800nm at the red edge. However, using a different surface type of sand, the peak of the reflectance is at 700nm. In these two cases, the albedo has a very specific shape, and the reflectance spectra clearly exhibit similar shapes and features. However, the albedo for the ocean doesn't exhibit strong spectral dependence, but is very low at all wavelengths, which is reflected in the low TOA reflectance.

Finally, the cloud sensitivity studies show that for both ice and water clouds, the effect of doubling the thickness from 1km to 2km, and raising the height of the cloud by 1km results in very small changes in the TOA reflectance. In the water cloud example, increasing the cloud height by 1km increasing the TOA reflectance by a maximum of 0.03, however this is over 3 times the increase seen in doubling the thickness of the cloud. This effect is smaller in the ice cloud, reaching 0.02 and 0.005 respectively. In the water cloud, increasing R_{eff} has an effect slightly larger than that of changing the location of the cloud, by reducing the TOA reflectance by a maximum of 0.05. In an ice cloud, this change in R_{eff} results in a much larger change than that of location, and is smaller than changing the R_{eff} of the water cloud droplets, at 0.03. These responses are spectrally different, however, with the ice cloud responding suddenly more strongly from 1400-2000nm. Changing the LWC/IWC did not elicit a response, likely because the cloud was already optically thick. It was also shown how the 1600/1680nm wavelengths can be used to discriminate between cloud phase, with a clear difference in the TOA reflectance shown at these wavelengths.

These sensitivity analyses have provided an indication of the spectral response of TOA reflectances to key parameters and have helped to reinforce the wavelengths identified in Chapter 2 as worthy of particular further analysis in Chapters 4 and 5. They also show that for a majority of the conditions considered in these studies, the spectral responses are large enough that they would definitely be detected by a TRUTHS-like instrument.

The second set of sensitivity studies were specific to the Arctic in order to gain an understanding of the large variability of the region, and how each of the three factors

(surface albedo, SZA and clouds) affected the shortwave radiation. These studies were carried out at specific wavelengths, in order to observe the changing radiation at various levels in the atmosphere at that wavelength. Firstly, the reflectance maps from the COSSE runs show the wavelength dependence for the TOA nadir reflectance, and how each wavelength can pick up different features, such as Greenland snow cover at 940nm. These studies also show how complex the processes are in the Arctic, with all three factors having a significant effect on the radiation. Figures 3.15 and 3.16 show how just changing the cloud optical depth can markedly affect the distribution of radiation above and below the cloud layer. Increasing the τ from 2 to 8 increases the amount of radiation returning to TOA by nearly 20%. Also, these studies were only performed with a single layer of cloud, whereas realistically there would be layers of clouds, adding to the complexity. Perturbations to surface albedo show that when this is high enough, the cloud layer actually reduces the TOA albedo as it appears less bright than the surface. These results will be used to help interpret the COSSE results reported in Chapter 4, which show particular interesting behaviour in the polar regions.

The last sensitivity study explored the effect of water vapour on the shortwave radiation and therefore the TOA reflectance. The results showed that water vapour has a larger effect on the magnitude of the TOA nadir reflectance over a land surface, rather than the ocean. This is due to the albedos of the respective surfaces; the albedo of the ocean is so low, that there is little radiation reaching TOA, even without the addition of extra water vapour. Water vapour added to the atmosphere absorbs some of the radiation, however over ocean there is less reflected radiation to absorb compared with over land where there is a higher surface albedo. This study will be used to help interpret the detection times discussed in the next chapter when the COSSE output is separated according to surface type.

Chapter 4

Time to detect

The aim of this research is to assist in optimising the design of the TRUTHS satellite. In order to fulfil this brief, the ability of a TRUTHS-like instrument to detect a signal of climate change above the noise of natural variability was investigated. Building on the work of Feldman et al., (2011)(b), the time for a change in signal to emerge from background noise is calculated as a function of wavelength and location in order to identify where, and under what conditions, signals of change may be more rapidly detected. The impact of stringent requirements on detection are investigated, as well as the impact of spatial resolution. The latter study helps identify if high spatial resolution data analysis is advantageous, and how much information is lost, if any, by analysing the data at a lower resolution. In Section 4.3, the effect of surface type on the detection time is investigated. For this analysis, the data points are separated into land and ocean due to the significant difference in the albedos of these surfaces. The land and ocean data are separately averaged into 1.41° latitude bands for time to detect calculations, but global detection times are also considered at a range of key wavelengths.

4.1 Methods

The 'time to detect' is defined here as the number of years of Earth climate observation it would take to detect a signal of climate change above the noise of natural variability. In this case, the signal of climate change is considered to be a change in the TOA spectral nadir reflectance. Since the COSSE data (discussed in Chapter 2) are produced over a comparable wavelength range and at a resolution similar to which TRUTHS would

operate, these calculations provide an understanding as to the timescales upon which the mission would potentially be able to detect changes in the climate (assuming it followed the IPCC AR4 A2 scenario (IPCC, (2007))). The method for these calculations is outlined in Feldman et al., (2011)(b), based on an approach provided in Weatherhead et al., (1998). The basis of this 'time to detect' method is the assumption that the change in the variable of interest with time can be modelled as having a linear trend. In this linear trend model, a variable (in this case spectral albedo or spectral nadir reflectance) can be represented as,

$$Y_t = \mu + \omega X_t + N_t \tag{4.1}$$

where Y_t is the variable at time t, μ is the mean, ω is the linear trend, X_t is the 'linear trend function' (which in this case is the time coordinate of the data), and N_t is the noise in the data. Here, annually averaged data are used at a variety of spatial resolutions. Initially, only zonal averages are considered.

The next assumption made is that the noise can be modelled as a first order autoregressive process (AR(1)),

$$N_t = \phi N_{t-1} + \epsilon_t \tag{4.2}$$

where ϕ is the autocorrelation in the noise time series and ϵ_t is the white noise. The autocorrelation gives an indication of how one data point is related to the previous data points depending on the time lag. Since this case considers annually averaged data, for a first order autoregressive process the time lag is one year. This assumption was checked for the purposes of this experiment by analysing the correlograms of the noise. A correlogram is defined by Chatfield, (2003), as "*a graph in which the autocorrelation coefficients are plotted against the lag, k, for k=0,1...M, where M is usually much less than D*", where D is the number of data points. The purpose of inspecting the correlograms was to confirm that a time lag of 1 can be used, and thus the noise can be modelled as an AR(1) process. For this to apply, the autocorrelation should fall to near zero by the first time lag (see Figure 4.1 for a typical example). Near zero is quantified in

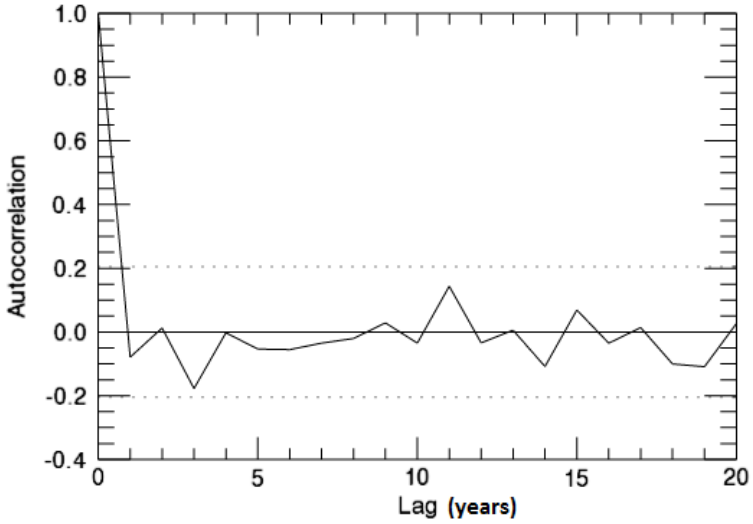


FIGURE 4.1: Correlogram of the noise in all sky spectral reflectance at 550nm, for a 1.41° zonal mean band centred at 25°N. The autocorrelation falls to within the significance boundaries shown by the dotted lines after a lag of 1 year.

Chatfield, (2003), as between $\pm 2/\sqrt{D}$. In general, the data obeys this criterion (with 67% of latitude bands for clear sky satisfying this condition, and 77% for all sky at 550nm) and so it was assumed that the noise could be modelled as an AR(1) process. It can also be concluded that the noise is random as the autocorrelation continues to be insignificant for all time lags (Chatfield, (2003)).

In Weatherhead et al., (1998) and Feldman et al., (2011)(b), the time to detect is defined as,

$$n_u = min\left(e^B\left[\frac{3.96\sigma(t)}{|\omega(t)|(1-\phi(t))}\right]^{2/3} < t\right) \tag{4.3}$$

where n_u is the estimate of the time to detect based on a subset of the time series data (t). B is the uncertainty in parameter estimation from a finite record and is dependent on the number of data points in the time series, M, and the autocorrelation, ϕ, as shown in Equation 4.4. The values of σ, ω, and ϕ are the standard deviation of the white noise, the trend and the autocorrelation respectively, based on a subset 't' of the whole record. These variables are calculated for increasing lengths of record, starting from a minimum length of 5 years, and so the value of each variable is dependent on the

timescale considered. n_u is the first point in the time series at which the first term on the right of Equation 4.4 is less than t, the time over which the data is considered. This can be considered as the time to detect a change above the noise with 95% confidence. The detection time was calculated for latitude bands; i.e. the reflectances were zonally averaged first, before calculating the time to detect for each band.

$$B = \frac{4}{3\sqrt{M}}\sqrt{\frac{1+\phi(t)}{1-\phi(t)}} \tag{4.4}$$

Equations 4.3 and 4.4 show that, if all other terms remain unchanged, as ω increases, the time to detect will decrease. However, a strong positive autocorrelation in the time series confounds the detection time; as the autocorrelation tends to unity, the time to detection will increase. Conversely, if the autocorrelation nears -1, then the time to detect will decrease.

In order to carry out the detection time analysis, the control run data were used initially to calculate the noise and the assumption was made that the noise would be the same in the A2 case.

In this experiment, a signal was considered detected if the left hand side of Equation 4.3, is less than the length of the record, t, beginning with 5 years of record. A caveat was added to this, that was not included in Feldman et al., (2011)(b) - the signal needed to be detected for at least 3 continuous years after the first detection. This value was chosen based on the minimum lifetime of a TRUTHS-like instrument. For completeness, example calculations were also performed setting this limitation to 5 years and 10 years in order to see how much of an effect this had on the time to detect for 550nm clear sky. Changing this value made no difference, which implies that once the signal has been detected for 3 years, it will continue to be detectable for at least 10 years.

Figure 4.2 provides a visual indication of how the time to detect is determined. Plotted against time on the x axis, are the values of the left hand side of the inequality in Equation 4.3 at each time, t. The dashed line is an x=y line that shows the boundary below which the values must fall to be considered detected, i.e. when they are <t. This

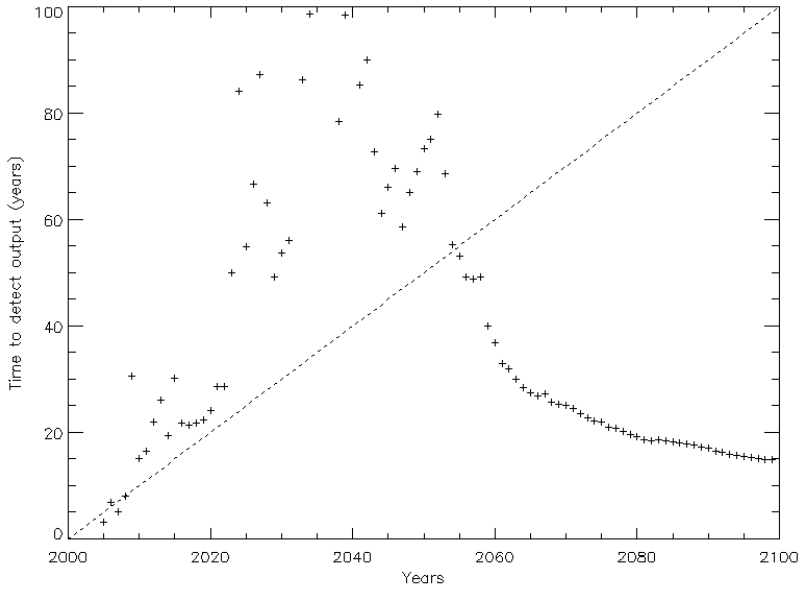


FIGURE 4.2: Detection time values from Equation 4.3

example is for 15°N, at 550nm, and under clear sky conditions. The data is plotted from 2005 due to the initial data record length being 5 years, but continues to 2100. It can be seen that the plotted values fall beneath the dashed line at 2005, however, at 2006 the value is above the dashed line again. This repeats at 2007, however this time the values remain above the dashed line until 2054, after which the values are consistently beneath the dashed line. It is for this reason that the new requirement was introduced - in order to reduce the possibility of obtaining a 'false' time to detect. While the signal must be detectable for a set number of years, the value recorded for the actual time to detect is considered to be the last year of this set time frame, i.e. the third consecutive year of detection. Hence, in this case, a robust detection would be at 2057.

4.1.1 Idealised case

The above method was tested using specific values to show how the detection time varies with the three variables; trend (ω), autocorrelation of the noise (ϕ), and standard deviation of the white noise (σ). In order to select appropriate values, the time series for the TOA reflectance from the COSSEs were examined at the eight wavelengths of interest specified in Chapter 2 (550nm, 660nm, 865nm, 940nm, 1375nm, 1600nm, 1680nm and 2190nm), and for both clear and all sky conditions. These wavelengths each have a

different purpose; 550nm is a transparent wavelength and used to define optical properties, 660nm and 865nm are in the red and NIR regions of the spectrum and can be used for vegetation characterisation. The 940nm and 1375nm are both in water vapour absorption bands, with 1375nm also being used for analysing cirrus clouds. Finally, 1600/1680nm are used to differentiate between ice and water clouds, and 2190nm is a final transparent wavelength used for soil moisture analysis. The values chosen as the typical values were as follows - ω of 0.0005 yr^{-1}, ϕ of 0.1, and σ of 0.005. The values chosen for each variable can simply be input into Equation 4.3 for each time step in order to obtain the detection time. Under these standard conditions, the detection time is 21 years.

The values of the three variables were altered to explore the effect each has on the time to detect. Table 4.1 shows how the trend affects the time to detect when compared to 'standard' conditions, with a higher trend of 0.001 yr^{-1}, and an almost zero trend of 0.00002 yr^{-1}. The detection times vary greatly for the range of trends tested - with a detection time of 15 years for a stronger trend, to undetectable within 100 years for the very low tend. Since these trend values are based on what is seen in the reflectance data being used in these studies, this gives a real insight into the detection times expected.

Trend (yr^{-1})	Detection time (years)
0.001	15
0.0005	21
0.00002	Undetected

TABLE 4.1: Detection times for varying trends for an artificial time series.

Table 4.2 shows the detection times for cases which have varying magnitudes of σ, but with trend and autocorrelation kept at standard values. It is clear that the larger the magnitude of σ, the longer the time to detect. This is expected since increasing σ would result in a lower signal to noise ratio, and fundamentally it would be more difficult to clearly detect a signal above the noise. The detection time varies from 21 years to 30 years which is a smaller range than that when varying the trend, but is still significant.

σ	Detection time (years)
0.01	30
0.0075	26
0.005	21

TABLE 4.2: Detection times for varying magnitudes of standard deviation of the white noise for an artificial timeseries.

Finally, Table 4.3 shows how varying the autocorrelation of the noise affects the detection time. The ω and σ were kept at their standard values of 0.0005 yr^{-1} and 0.005 respectively. The detection times increase with increasing autocorrelation, however the variation between the detection times is a lot smaller than those in Table 4.1 but is comparable with those in Table 4.2 which implies that the trend is the most significant factor that affects the detection times given realistic variations in σ and ϕ.

Autocorrelation	Detection time (years)
0.4	28
0.1	21
0.01	20

TABLE 4.3: Detection times for varying autocorrelations of the noise for an artificial timeseries.

4.2 Detection Time and Spatial Resolution

Since TRUTHS plans to derive nadir spectral reflectances, in this section the methodology described in Section 4.1 is applied to the nadir spectral reflectance time series that were simulated as part of the IPCC AR4 A2 Scenario COSSEs (described in Section 2.2). Apart from the previous stipulation that a signal should be detected for a specified period of time in order for detection to be considered as having occurred, the difference between this experiment and that carried out in Feldman et al., (2011)(b) is that here the data were analysed at two different resolutions; at coarse 10° latitude bands, and at the smallest resolution of 1.41° latitude bands. This is to determine if the spatial resolution has an effect on the time to detect. Zonal 10° bands were chosen as the lower resolution as this is the nominal grid size at which CLARREO products will be released to the scientific community (Wielicki et al., (2014)). In essence, the aim

of this study is to help direct instrument design or, alternatively, the way in which the data are provided to the user community.

4.2.1 Noise Characterisation

One of the features of TRUTHS, second to its ability to act as a standards laboratory in space, is that it will be able to take measurements with high accuracy and so potentially detect the signals of climate change above natural variability more rapidly than less accurate measurements. In order to detect a robust signal of change it is important that the change is larger than the noise of the time series, and therefore it is important to characterise the noise. The noise varies globally and with wavelength and as discussed before, identifying spatial and spectral regions that are less noisy could be of use for a mission such as TRUTHS. The aims of this section of work are to characterise the noise at certain wavelengths in order to see how the noise varies, and where the largest noise is globally. It is important to understand what a 'significant' signal above the noise would be.

Method and results

While the noise characteristics were calculated at all wavelengths, in order to understand its characteristics (calculated from Equation 4.1, using the control run data which contained no trend), specific wavelengths were chosen to focus on. Here, 550nm was chosen as it is a window region in the visible part of the spectrum (see, Figure 1.2) and it is commonly used as a reference wavelength to define cloud and aerosol optical depth.

The next stage was to determine how the noise varies spatially across the latitude bands, and also how stable it is over the 100 years of simulation. Figure 4.3 shows the total noise contour plots for spectral reflectance at 550nm under clear sky (Figure 4.3a) and all sky (Figure 4.3b) conditions using the 1.41° latitude band data. The largest variations in noise in clear sky conditions are confined to the Arctic and Antarctic regions. For the all sky case (Figure 4.3b), the largest noise is still in the Arctic and

Antarctic regions though these peaks are smaller than for the clear sky case. It can also be seen that elsewhere the noise is of a similar magnitude in both Figure 4.3a and 4.3b. Equivalent plots were also created for the 10° latitude band data; in this case, the range and location of the extremes in the noise are the same. As seen in Equation 4.2, the noise is assumed to be an AR(1) process with additional white noise. Analysing the white noise component as derived from the data shows that with increasing record length, the variance tends towards a constant value, and its average tends towards zero as required. Figure 4.3c shows the white noise, ϵ(t), for the case of 550nm under clear sky conditions. It is clear to see that the features are the same spatially as that in Figure 4.3a, albeit with slightly lower magnitudes, suggesting that the noise is dominated by the white noise component. Figure 4.3d also shows how the lag 1 autocorrelation in the total noise varies with latitude. It is clear to see the autocorrelation fluctuates substantially across the globe, from -0.55 to +0.5 and changes sign multiple times. The strongest negative autocorrelation is at the equator, with the largest autocorrelations occurring at high latitudes.

It is possible that the larger noise in the Arctic is due to ice melt and growth, as the simulations do account for this. Though the data has been deseasonalised, it is possible that timings of the ice growth and melt vary from year to year, and also that the extent of the ice is different every year in the model, as it is in reality as shown in Stroeve et al., (2012). Also, the reduction in noise in the all sky compared to the clear sky case at the poles could be due to clouds partly masking the ice melt and growth. These findings provided motivation for the polar sensitivity studies described in Chapter 3.

4.2.2 Resolution Comparisons

Figures 4.4 through 4.7 show the times to detection for the nadir reflectance at 550nm. Each figure is a contour plot of the reflectance anomalies which are relative to the average reflectances for the period 2000-2009 and the black line displays the time to detect the signal for each latitude band. Figures 4.4 and 4.5 are both at 10° resolution. The reflectance anomaly in Figure 4.4 shows an increase in reflectance about the tropics between 2020 and 2060. This corresponds to the increase in aerosols that is seen in Figure

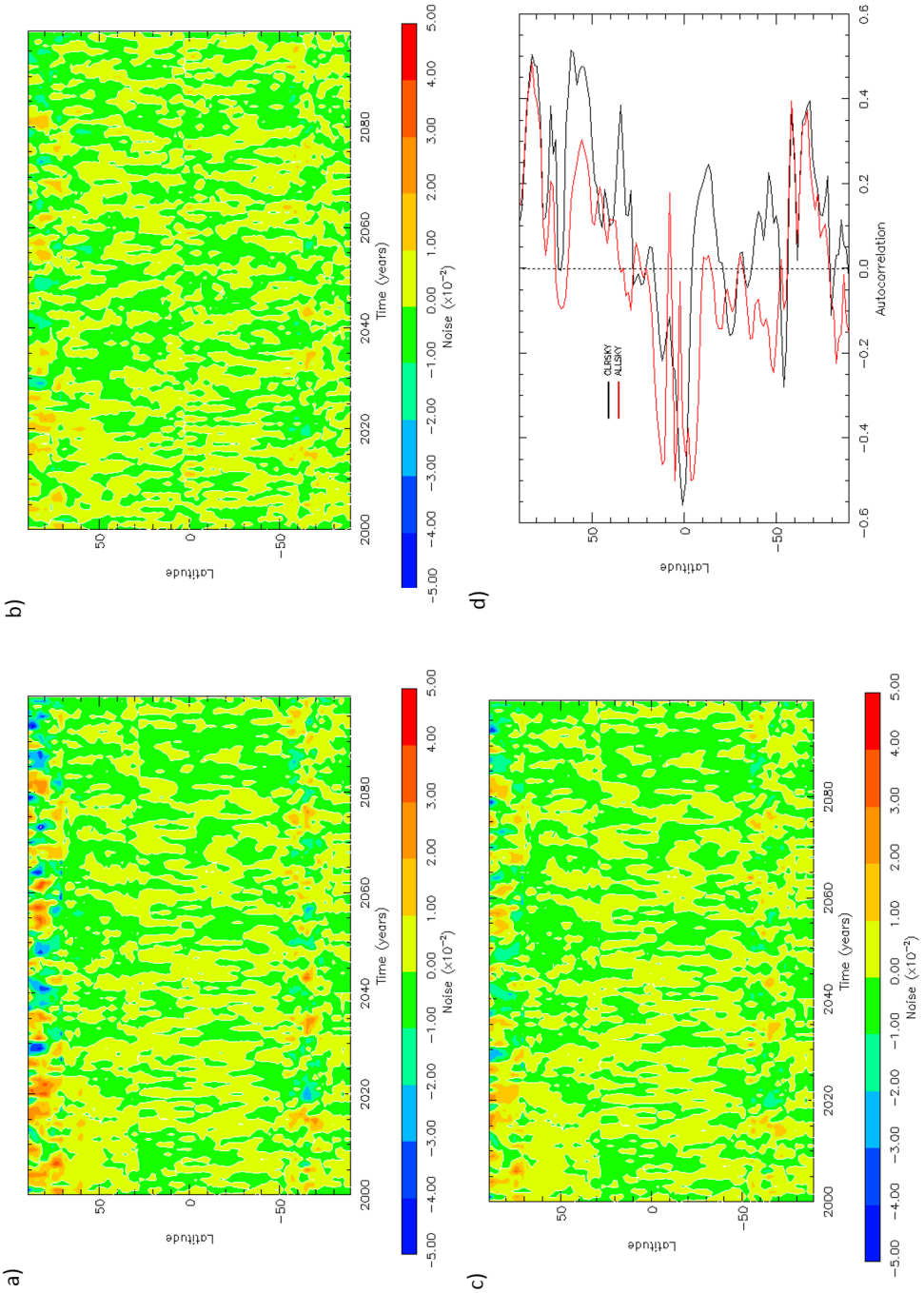


FIGURE 4.3: a) Noise for 550nm at each latitude band for the time period 100 years for clear sky conditions, b) the same for all sky conditions, c) white noise under clear sky conditions, d) the lag 1 autocorrelation for 100 years under clear and all sky conditions. All at 1.41°.

2.5 which increase the reflectance since they are typically brighter than the underlying surface. The anomaly also shows a significant decrease in reflectance in the northern hemisphere - the reflectance anomaly reaches -0.05 around the pole first, before spreading south as far as 50°N by 2100. There is also a negative anomaly of -0.05 centred on 65°S which presents itself later at 2075. This latitude is for the Southern Ocean and the tip of Antarctica. While it is accepted that the ice sheet in Antarctica undergoes no annual melt, it is discussed in Liston and Winther, (2005) that there is surface ice melt in near-coastal regions of Antarctica, and therefore these anomalies could be attributed to melting ice which would lead to a decrease in reflectance.

The detection times in Figure 4.4, denoted by the black line, show two peaks at the Arctic (70-80°) and Antarctic/Southern Ocean (50-70°). The Antarctic peak is larger with a detection time of 77 years, while the peak at the Arctic reaches 48 years. These two long detection times occur in regions where there is a strong negative anomaly in the reflectances, so are unexpected. However, as shown previously in Figure 4.3a, the noise in these areas is larger, which would make it more difficult to detect a trend. Related to this, the anomalies in these regions are variable and oscillate between negative and positive - this variability would also affect the ability to detect trends. The detection time clearly coincides with the beginning of a robust negative signal.

The detection times are typically lowest between 50°N-50°S. Figure 4.4 shows the detection times are 8-11 years between 30°N-50°S corresponding to the positive anomalies around this region. Also comparing with Figure 4.3a, the noise is relatively low in these regions and therefore a combination of the steady, positive trend and low noise leads to a swift detection time.

In Figure 4.5 for the all sky conditions, similar patterns are seen in the anomalies. However, the decreases in reflectance around the Southern Ocean and the Arctic are smaller, with both beginning later at 2085 and 2055 respectively, and with the Southern Ocean anomaly only reaching -0.03. Positive anomalies are of the same magnitude as in the clear sky but are more fragmented and spread into the south and the north at 60°N. This shows that the addition of clouds adds some variability in the anomalies.

For all sky conditions, the detection times are longer around the tropics and midlatitudes, averaging at 20 years. This is expected due to the confounding influence of the clouds. Clouds tend to be more variable in space and time than the underlying atmospheric state (e.g. temperature, humidity) and therefore are likely to be obscuring the aerosol induced reflectance trends in the tropics. The detection time only reaches 10 years at one latitude band - 20-30°N. Conversely, the detection times in the Arctic and Antarctic regions are reduced with the addition of cloud. This is due to there being less noise in these regions when clouds are added. This can be seen in Figure 4.3b which shows the noise in the Arctic peaking at 0.015 as opposed to 0.035 in Figure 4.3a.

Figures 4.6 and 4.7 show the same as Figures 4.4 and 4.5 but at the higher 1.41° resolution. Comparing the reflectance anomalies, the clear sky anomalies show the same broad features at both resolutions. There is more variability seen at 50-70°S and 70-90°N in Figure 4.6 which isn't captured at the lower resolution. However, at 50-70°S the detection time is approximately the same at 81 years, versus the 77 years at low resolution. This can be seen clearly in Figure 4.8, which shows the detection times for both 1.41° and 10° resolutions. In the 70-80°N band, the high resolution detection times range from 22-66 years compared to the 45 years in the low resolution scenario. This is due to the fact that the 10° latitude bands effectively average all of these small fluctuations together and so there is less noise. However at 1.41° latitude bands, the detection times can vary due to these small fluctuations which can lead to, for example, a 22 year detection time at 80°N, and then a detection time of 66 years at 70°N.

In the all sky case, Figure 4.7, again the reflectance anomalies are very similar but with the added level of detail expected. There is also a broken 'line' of positive anomaly around the equator up to 2100 that is not seen in Figure 4.5. This plot also shows clearly that there is a large difference around 60-70°S, the Southern Ocean/Antarctic region. By considering the anomalies, Figure 4.7 shows there are lots of fluctuations and noise in this region which could mask the signal and lead to a longer detection time, whereas in Figure 4.5 the detection time is shorter due to the positive signal in the reflectance up to 2040.

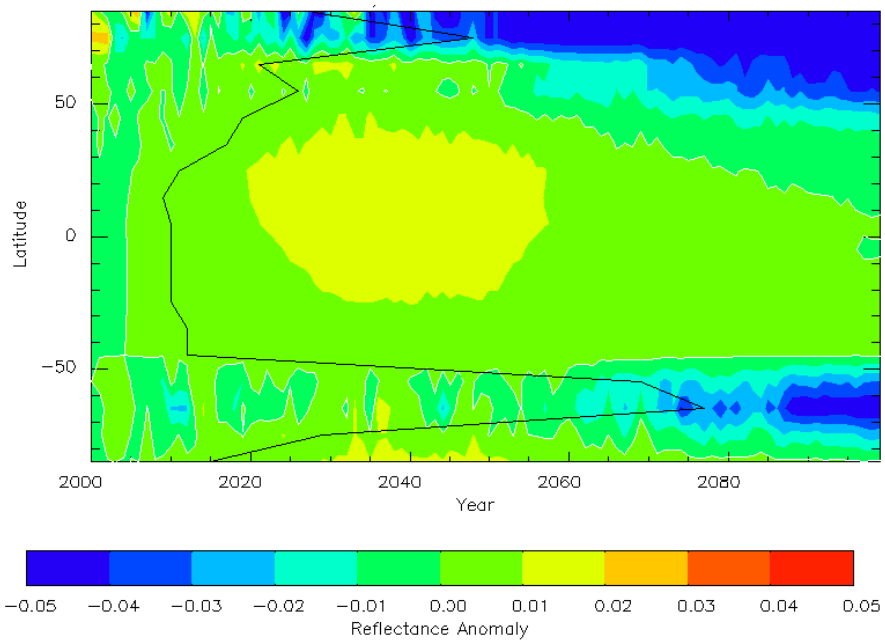


FIGURE 4.4: Zonally and annually averaged nadir reflectance anomalies for 10° latitude bands at 550nm, with respect to the average reflectance for the time period 2000-2009, under clear sky conditions. The black line indicates the time to detect; the white contours indicate zero anomaly.

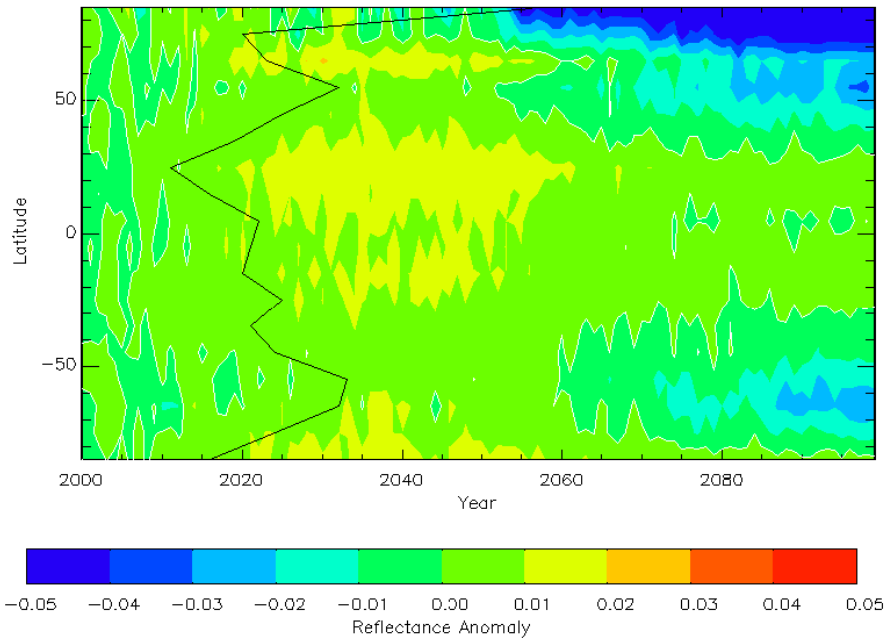


FIGURE 4.5: Zonally and annually averaged nadir reflectance anomalies for 10° latitude bands at 550nm, with respect to the average reflectance for the time period 2000-2009, under all sky conditions. The black line indicates the time to detect; the white contours indicate zero anomaly.

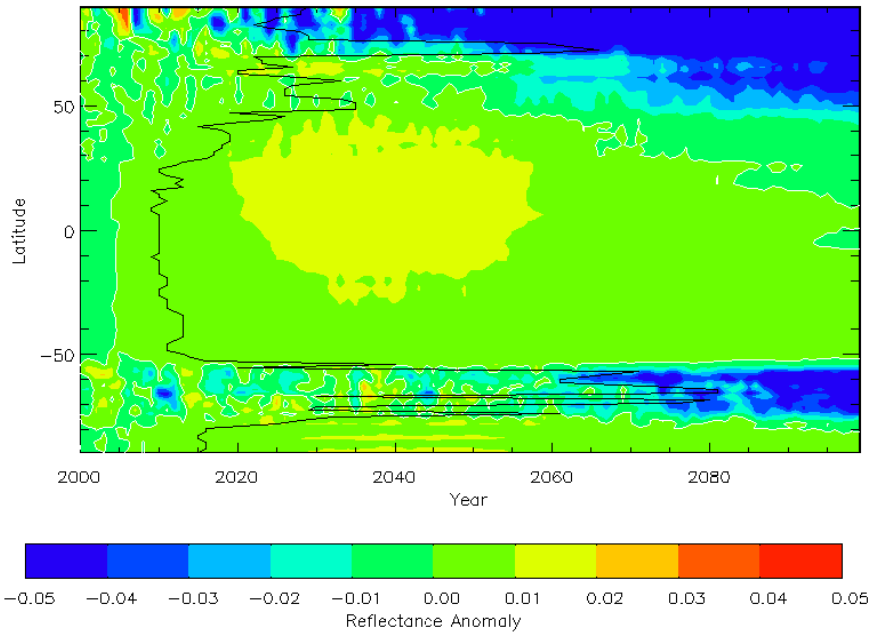


FIGURE 4.6: Zonally and annually averaged nadir reflectance anomalies for 1.4° latitude bands at 550nm, with respect to the average reflectance for the time period 2000-2009, under clear sky conditions. The black line indicates the time to detect; the white contours indicate zero anomaly.

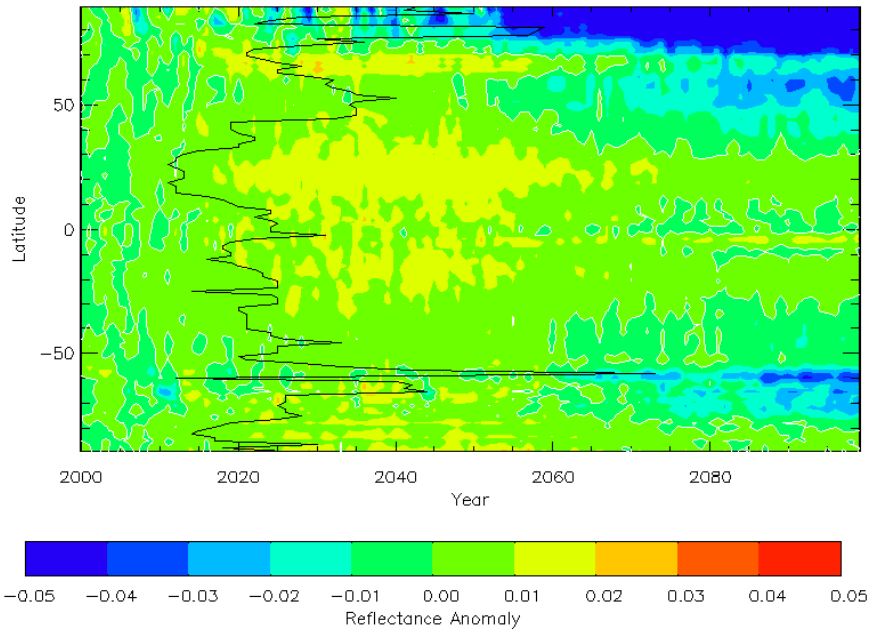


FIGURE 4.7: Zonally and annually averaged nadir reflectance anomalies for 1.4° latitude bands at 550nm, with respect to the average reflectance for the time period 2000-2009, under all sky conditions. The black line indicates the time to detect; the white contours indicate zero anomaly.

While there are differences between all of the plots, they all show the same broad features; strongly decreasing reflectance at northern most latitudes, extending progressively southward as time progresses to 50°N, a notable decrease in reflectance after year 2060 at 60-80°S, and a positive anomaly region around the equator. The positive anomaly region corresponds with the changes in AOD, seen in Chapter 2, Figure 2.5. This indicates that the increase in aerosol optical depth towards 2050 causes an increase in reflectance which is particularly noticeable in the clear sky case. As noted earlier, the decrease in reflectance in the poles points to a decrease in snow cover and sea ice. For both features the patterns are more coherent in the clear sky simulations, and that cloud adds additional 'noise' to these aerosol induced responses in the tropics, however the clouds reduce the noise at the poles, as shown previously in Figure 4.3b.

Figures 4.8 and 4.9 extract the detection times at each latitude for both high and low resolutions, for clear and all sky conditions, respectively. A dashed line has been added to show a simple average of the 1.41° detection times into 10° bands. This is a different approach to the method used here, where the reflectances are averaged into the 10° latitude bands prior to calculating the detection time. The purpose of the analysis in Figures 4.8 and 4.9 is to investigate whether it is a linear process, i.e. whether the method affects the detection time. This shows that the relationship between the detection time and the TOA nadir reflectance is near linear in some regions, i.e. averaging the reflectances first and averaging into latitude bands after calculating the detection times yield similar results in some areas. For example, in Figure 4.8 the relationship is nearly a linear process in clear sky conditions between 10°N and 40°S, and is also very close at the same latitudes in the all sky case too (Figure 4.9). The detection times are different, and therefore the relationship is not linear, at higher latitudes. Comparing the times to detection in all cases, the major difference is that in the high resolution cases there is a lot of fluctuation in the times to detect across the latitude bands. However, generally speaking the 10° resolution appears to result in a quicker time to detect, seen in both Figures 4.8 and 4.9 where the 10° detection times are slightly lower. In Figure 4.8, the detection times at both resolutions are generally the same at 5°N-15°S, however for the 10° resolution detection times are predominantly lower in this clear

sky case. One exception is for the 10° latitude band 50-60°S where the detection time is 70 years, compared to the range of 13-70 years at 1.41° resolution over the same band. In Figure 4.9, the detection times are also generally shorter for the lower 10° resolution latitude bands.

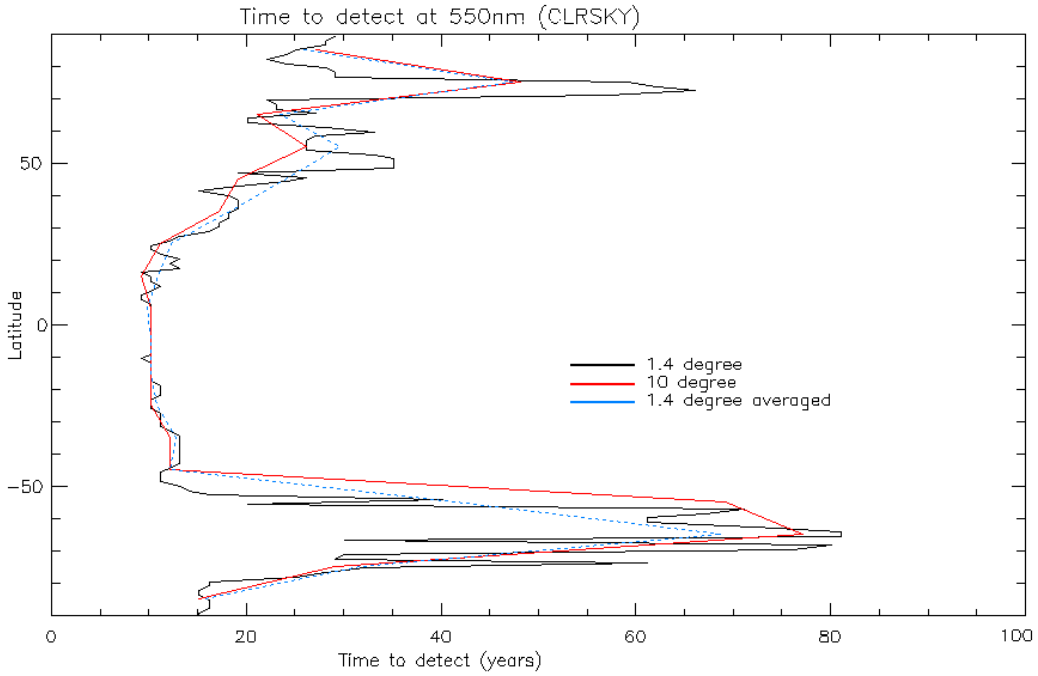


FIGURE 4.8: Detection times at 550nm clear sky for 1.4°, 10°, and the 1.4° data averaged into 10° latitude bands.

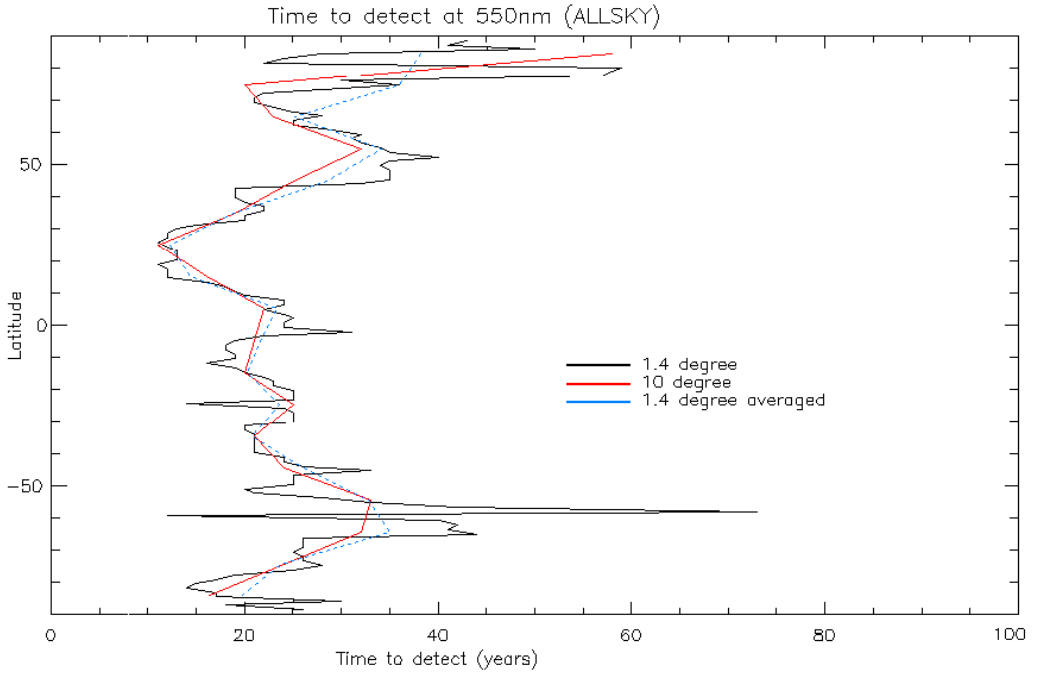


FIGURE 4.9: Detection times at 550nm all sky for 1.4°, 10°, and the 1.4° data averaged into 10° latitude bands

Having focussed on the time to detect at a particular wavelength, it is then of interest to extend the calculations to every wavelength included in the data. Figure 2.7 showed the variability in the albedo anomalies at different wavelengths for a given latitude, and it is expected that these types of differences will be seen at all latitudes manifesting in varying detection times with wavelength as well as location. Figure 4.10 shows that the time to detect does indeed vary with wavelength, and that some of the regions with higher times to detect correspond to the absorption bands seen in Figure 1.2, such as at 940nm and 1400nm. Also shown is the ability of the 10° latitude band average data (Figure 4.10c and d) to still show the same patterns as the higher resolution data and broadly capture the variation across the latitude bands and wavelengths (Figures 4.10a and b). However, as demonstrated in Figures 4.4-4.7, some small scale detail is lost by using the lower resolution.

The most noticeable feature in Figure 4.10, as noted in the 550nm example in Figures 4.4 - 4.7, is that the times to detect a signal under all sky conditions are typically longer. In Figure 4.10a there are large areas that only take 7-15 years to detect a signal, however, in Figure 4.10b the same areas show 10-25 years as the typical time for detecting a signal. However, all figures show that the time to detect a signal is long at high latitudes, with both clear and all sky displaying times of 50-100+ years in these areas at several wavelengths (typically <1300nm). The time to detect is also relatively longer than at other wavelengths at the same latitudes in the tropics and mid-latitudes in the water vapour absorption bands under both clear and all sky conditions. The effect of wavelength on the time to detect does however vary depending on latitude. For example, under clear sky conditions (Figure 4.10a) the time to detect at the equator remains at 10-15 years for all wavelengths. However, at 60°S the time to detect ranges from 10-15 years at 1850nm, all the way to 50-75 years at 700nm. 1850nm is the centre of a CO_2 absorption band and so it is possible that the detection time here is a lot shorter due to the increasing CO_2 in this model scenario. Using plots such as these, it is possible to identify wavelengths and latitudes at which it would be quicker to detect a signal – this is potentially useful for satellite missions like TRUTHS as attention can be focussed towards these regions.

The longest times to detection are often seen in the polar regions, most noticeably in the clear sky cases, from 300-1300nm. This might seem surprising given the large warming trends expected in these regions coupled with reducing snow and ice fractions but has been shown to be a direct result of the noise in the data. The noise is seen to be much larger in the Arctic, and often in the Antarctic region too. The first possible source of this noise is variable seasonality in ice melt and growth seen in these areas, coupled with their highly variable albedos, which themselves show a strong SZA and wavelength dependence. In the sensitivity studies for the Arctic region in Chapter 3, it was shown that SZA and clouds also have large effects on the fluxes and that the relative magnitude of their impact varies with surface albedo. Hence the variety and complexity of cloud over the region, and its interplay with the underlying surface is likely to also have contributed to the noise.

In the water vapour bands, such as 940nm and 1375nm, the detection times are approximately 20-25 years under clear sky conditions, but increase significantly to 30-75 years with the addition of cloud. Clouds not only introduce more water vapour into the atmosphere which can dominate and obscure climate change signals, but also the clouds themselves are variable and not always there or always the same. This adds interannual variability in the TOA reflectance and therefore increases the detection time.

It is interesting to see that at 2190nm (and 1600/1680nm), in both the clear and the all sky cases, the time to detect is relatively low with a range of 10-25 years throughout the majority of the latitude bands. The window regions generally show shorter detection times than the absorption bands, with the exception of the 50-80° in the Northern and Southern Hemispheres at <1300nm. The detection times at 2190, 1600 and 1680nm are still relatively short even in all sky conditions as seen in Figure 4.10b. These three wavelengths are all in window regions and the long wavelengths are able to penetrate thin clouds, since they are less susceptible to scattering by the clouds. This means that there isn't a dramatic change in the detection times, such as that seen in the water vapour bands. This all suggests that 2190nm and 1600/1680nm may be particularly useful in order to detect signals of climate change above natural variability earlier than at other wavelengths.

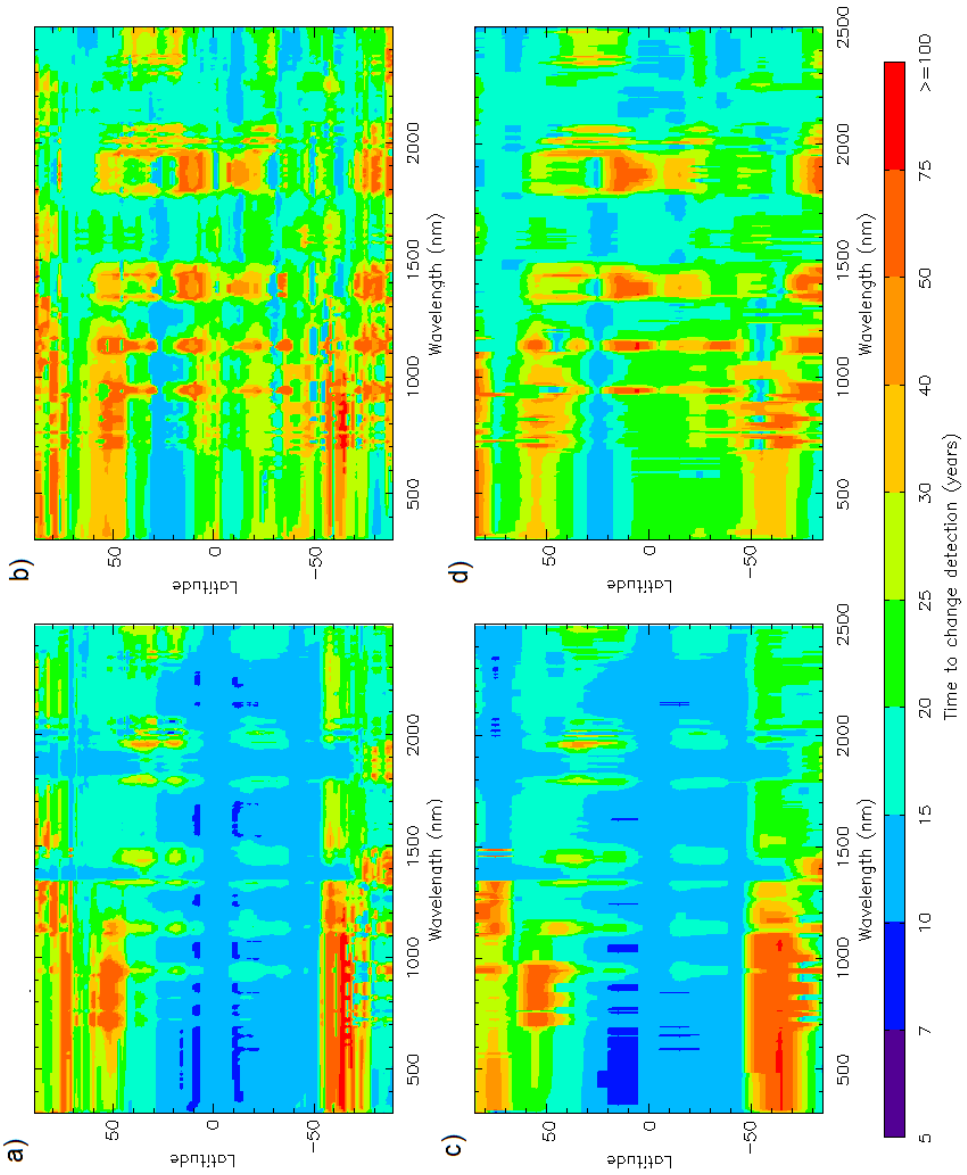


FIGURE 4.10: Time to detect for each latitude band, for every wavelength (300-2500nm). (a) 1.41° latitude bands, clear sky conditions, (b) 1.41° latitude bands, all sky conditions, (c) 10° latitude bands, clear sky conditions, (d) 10° latitude bands,all sky conditions.

4.2.3 Summary and Inferences

COSSE data have been used to calculate the time it would take to detect a climate change signal above the noise of natural variability. Based on a record starting in 2000 and following the IPCC AR4 A2 scenario, it has been shown that in clear sky conditions there are some latitudes and wavelength regions where a signal could be detected in 7 years. However, while the average time to detect under these conditions is relatively low (<15 years), there are still spectral and spatial regions where the time to detect would be 50-75 years, with small areas with a time to detect of >75 years or no detection would be possible within the record length, such as at 65°S between 700-900nm. The addition of cloud increases the time to detection on average; there are only small regions that display a time to detect of 10-15 years, and this is the lowest value seen under the all sky conditions. Comparing the two spatial resolutions of 10° and 1.41° latitude bands provided interesting insights into the spatial coherence of the signals. While fine details were understandably not visible at the coarser resolution, the general structure and magnitudes of values were comparable to those of the high resolution data. For example, in the clear sky scenario (Figures 4.10a,c) the broad 10-15 year band detected at 30°N-50°S (as well as the 15-20 year features within this) are captured in the lower resolution example (Figure 4.10c).

One question that has been asked by the CLARREO science team, and is of the same importance relative to TRUTHS, concerns the optimal resolution at which to provide data to the community, if the data were to be used directly for trend detection. Figures 4.11a-d address this by comparing the number of wavelengths (440 wavelengths for the range 300-2500nm) and latitude bands at which signals are detected for the two resolutions of data. Figure 4.11a shows the number of wavelengths with a time to detect less than 10 years for clear sky conditions at both resolutions. Figure 4.11b shows the equivalent information for all sky conditions. Comparing the conditions first, the most notable difference is that there are significantly fewer wavelengths with signals detectable within 10 years in the all sky case – essentially summarising the general impression from Figure 4.10 that the all sky times to detection are generally longer. Looking more closely, it can be seen at most latitudes that the number of wavelengths

that provide a time to detection of <10 years is larger for the 10° latitude bands confirming that the results seen in Figure 4.9 are general across wavelength. There are exceptions in the clear sky case for 10-20°S, 50-60°S and 30-40°N, where nearly all of the higher resolution latitude bands show more wavelengths available than the equivalent 10° zonal mean. This is also evident in the all sky case (Figure 4.11b) at 10-20°N, 40-50°S and 60-70°S.

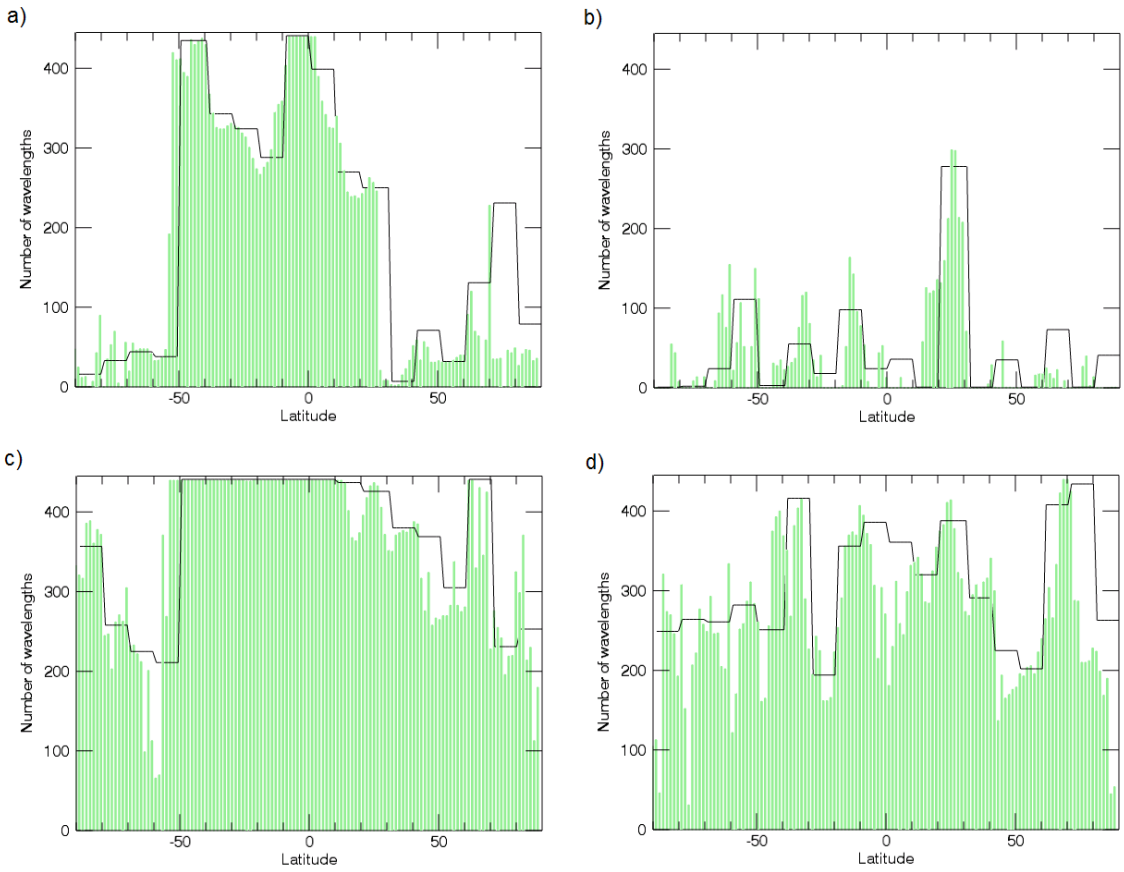


FIGURE 4.11: a) Number of wavelengths which have a time to detection for the spectral nadir reflectance less than 10 years, for each latitude band, for clear sky conditions. The green bars show the values for the 1.4° latitude band data, while the black line shows the same values for the 10° latitude bands; b) same information for the all sky case; c) same information for clear sky case but with a condition of 20 years, and d) as (c) for all sky.

Figures 4.11c and 4.11d show the same information as Figures 4.11a and b but with the condition of a 20 year detection time. The obvious difference is that there are a lot more wavelengths that allow a detection in this time frame. There also appears to be less discrepancy between the clear and all sky numbers - this is due to the fact that many clear sky detections have already occurred within 10 years, especially in the tropics

and the mid-latitudes. Comparing the clear and all sky cases, it seems that the high resolution results are more variable under all sky conditions, with more examples of the 1.41° bands performing better than the 10° data in terms of number of wavelengths showing a detection compared to a 10 year limit. At 70-80°N in the clear sky case, the number of wavelengths for the 10° latitude band appears to not have changed between Figure 4.11a and 4.11c. However, it is especially noticeable that the values for 60-70°N have changed dramatically.

Generally, the 10° resolution data results in more wavelengths at which a robust signal is detectable, however in Figure 4.11c the high resolution data results in significantly more wavelengths providing a detection in the 70-90°N bands. This could be due to a combination of the region undergoing ice melt and regrowth affecting the times to detection. At high resolution, some areas aren't affected seasonally by ice and so shorter detection times are possible. However, averaging over these areas to create the 10° bands, averages across these different conditions which makes it more difficult to detect any signal above the noise. Conversely, at high resolution, the small signals from ice melt and regrowth can be detected due to lower noise. Also, comparing with this region in Figure 4.10a shows that these wavelengths with a shorter detection time are predominantly in window regions of the spectrum, as opposed to the absorption bands which supports the idea that the surface changes are affecting the time to detect in this region.

This all leads to the conclusion that providing data for the detection of trends to the community at 10° averaged latitude bands may in fact be more beneficial as there is little difference between the higher and lower resolution latitude bands. Looking at the specific numbers of wavelengths at which the detection time is <10 or <20 years supports this conclusion in both clear and all sky. Comparing the percentages of wavelengths at which a signal is detectable for both the 10° and 1.4° latitude bands, seen in Table 4.4, it is clear that in each of the four cases (<10/20 years, and clear/all sky) the 10° bands perform better and provide a detection where the high resolution data doesn't. The largest differences in numbers are under all sky conditions with a detection time of less than 20 years, where the 10° bands detect a signal at 9.2% more

wavelengths. It is also interesting to see that under these conditions, 70% of wavelengths show a detection. Also, while a much smaller percentage, it is still possible to detect a signal within 10 years at 10% of wavelengths with 10° latitude bands (also under all sky conditions).

	<10yrs (CLR)	<10yrs (ALL)	<20yrs (CLR)	<20yrs (ALL)
1.4° bands	40.1%	9.0%	80.9%	60.9%
10° bands	43.3%	10.1%	82.6%	70.1%

TABLE 4.4: Number of wavelengths with detectable signal for 1.4° and 10° latitude bands

These analyses have helped to understand the effects of spatial resolution on the time to detect a signal above the noise of natural variability. However, it is important to understand that these are based on a 100 year continuous time series, whereas realistically, satellite observed data will most likely have gaps in it. The effects of this are explored further in Chapter 5.

4.3 Land-Ocean Comparisons

So far, the analyses carried out have looked at latitude band averages, however almost all of these bands are composed of both land and ocean. The properties of these two surfaces are very different; firstly, the albedos of these surfaces are different; under most illumination conditions the ocean is a darker surface, with albedos as low as 0.03-0.06 (Payne, (1972)), and the continents are typically much brighter and also more variable (He et al., (2014)). Moreover, due to both thermodynamics (differing heat capacities) and dynamical influences (e.g. prevailing winds), different cloud characteristics over different surface types may be expected. For example, marine stratocumulus clouds over the ocean on the western coasts of land masses, or deep convection over land. Hence an interesting question is whether it would be quicker to detect a climate change signal over the land or the ocean. If a significant difference is seen in the detection times between the two surfaces, it could have implications for the way in which data from a TRUTHS type mission is processed and distributed.

4.3.1 Global Detection Times

For these analyses, the reflectances and the subsequent detection times were calculated for every 1.41x1.41° grid point instead of averaging into latitude bands. Initially, these detection times were plotted at the specific wavelengths discussed in Chapter 3. This was to look at the global variation in the time to detect, before looking more in depth at the differences between land and ocean. The first example shown here, in Figures 4.12 and 4.13 is for 2190nm, under clear and all sky conditions respectively. As discussed in Chapter 2, 2190nm is in a window region and is used by Sentinel-2 for snow/ice/cloud discrimination (Li et al., (2017)) and by Landsat (Band 7) for moisture analysis (Barsi et al., (2014)). In Figure 4.12, the detection time is generally low, at less than 20 years. However, there are regions with a very long time to detect. Several of these regions appear over deserts - it is very easy to pick out the Sahara and the Arabian desert (10-30°N, and 0-60° in longitude), and follow the larger detection times across the Indian desert to the Gobi desert. It is also possible to see a small amount of desert in Northern America, centred at 40°N. The Australian deserts do not have as long detection times as the aformentioned deserts, but can be distinguished from the surrounding areas. The changes in this IPCC AR4 A2 climate change scenario are fuelled by increases in CO_2 and sulphate aerosols, and aerosol scattering over the bright desert surfaces would have less of an effect than aerosol scattering over dark ocean surfaces. This means that even though there are significant increases in the aerosols over the aforementioned deserts (see Figure 2.5), these changes cannot be detected at this wavelength. This translates to a long detection time over the deserts, i.e. 2190nm, is not useful for detecting aerosol changes in these regions. There is also a region over the Southern Ocean that exhibits a longer time to detect. This is seen in most of the time to detect maps that were examined, and is due to the fact that the aerosol changes are very small at 55-65°S (as seen in Figure 2.5), and so there is little trend, resulting in larger detection times.

Figure 4.13 shows the equivalent information but for all sky conditions. It is immediately obvious that the time to detect is longer under all sky conditions, consistent with previous results. Unsurprisingly the deserts are still visible, with little change in

the time to detect from clear sky conditions due to the fact that little cloud is seen in these areas. There is a general increase in time to detect over all ocean basins with a particularly large increase in the time to detect over the Pacific Ocean. This is due to the cloud adding variability, or noise, since it has a much more dramatic effect over the ocean than land due to the much larger contrast between the dark ocean surface and the bright clouds above.

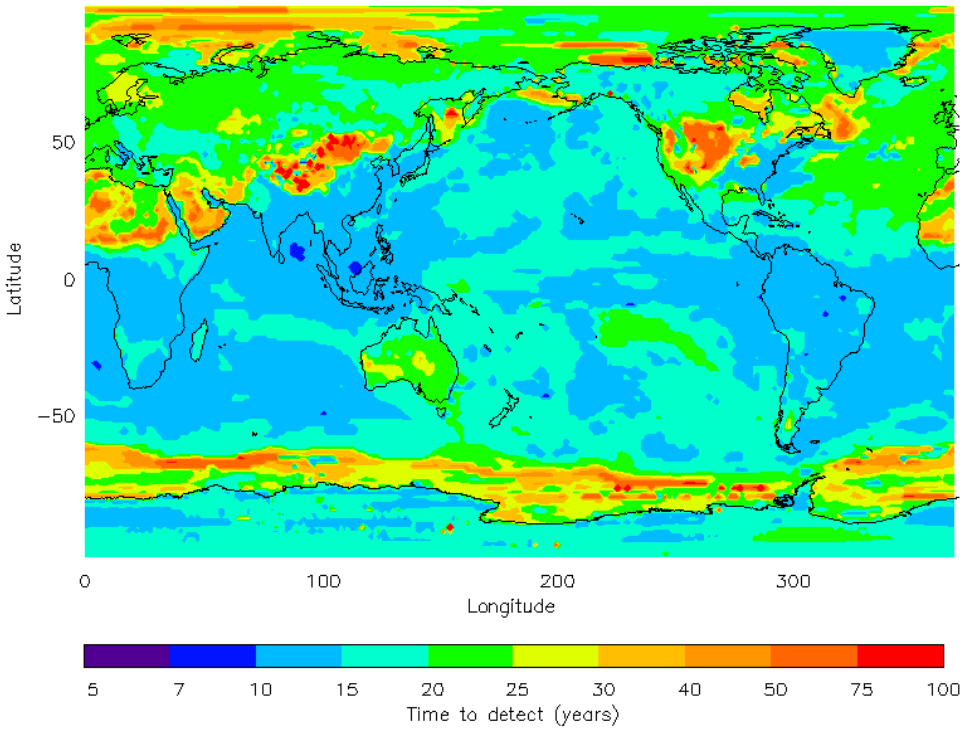


FIGURE 4.12: Map of the detection times at 2190nm, under clear sky conditions

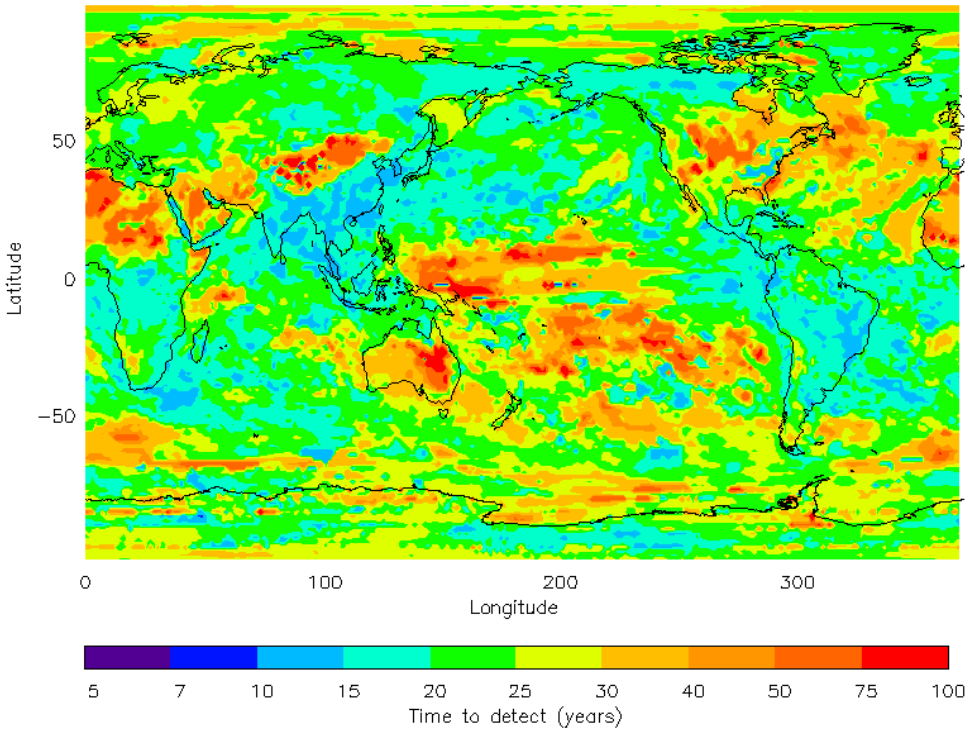


FIGURE 4.13: Map of the detection times at 2190nm, under all sky conditions

The next example is for the wavelength 940nm, which is a water vapour absorption band and the detection time results are shown in Figure 4.14. The detection times for 940nm are higher than in the previous example at 2190nm (Figure 4.12). It is also very easy to distinguish the continents, which under clear sky conditions typically exhibit enhanced detection times compared to the oceans. In general, the continental areas with long detection times correspond to areas that do not contain forest, with the shorter detection times found in forested regions. As demonstrated in Chapter 3, water vapour has a larger effect on the TOA nadir reflectance when over land compared to over ocean. This can be used in this case to explain the difference in detection times over the bright desert and the forests which also have very low albedos like the ocean. In water vapour absorption bands, the water vapour is absorbing the incoming radiation and reflected radiation from the surface, therefore reducing the amount that reaches the TOA. Over a dark surface such as the ocean or forest, this effect is less noticeable since the albedo of the surface is very low, and so the amount of radiation reaching TOA is very low with or without water vapour. However, as the land has a higher albedo, the amount of radiation absorbed by water vapour is larger. As shown in Chapter 3 Figure 3.17, this effect means that changes in water vapour have a much larger effect on the TOA nadir reflectance over land than the forest. Because there is no coherent trend in water vapour, this results in a longer detection time over the land because this greater sensitivity results in more variability which masks the aerosol induced signal. It can be seen that the Sahara Desert and tip of southern Africa have detection times of approximately 50-75 years, whereas the central region (the Congo River Basin Rainforest) has a detection time of 15-25 years. Antarctica also has a long time to detect as it is also dry, as does the Australian desert. The shorter detection times (as seen in the Congo River Basin) are seen across Asia which is covered in tropical rainforest, and the majority of the forest area across Russia also displays the same lower detection time.

The all sky case at 940nm is shown in Figure 4.15 and clearly shows the effect of clouds on the time to detect. The detection times increase significantly, with most areas displaying times of 40 years or more, because the clouds change the reflectivity and obscure the atmospheric and surface changes. Figure 4.15 is a typical example of the all

sky detection time maps at most of the examined wavelengths (excepting 2190nm), with very long detection times seen over most of the globe. In the visible (550, 660 and 865nm), the all sky maps (not shown) predominantly show long detection times of 50-100 years, with clouds obscuring any detectable signal. This is rather different to the 2190nm results shown in Figure 4.13 and occurs because the visible wavelengths are shorter and are subject to strong scattering effects by all but sub-visual clouds. In contrast, 2190nm is a much longer wavelength and is able to penetrate thin clouds.

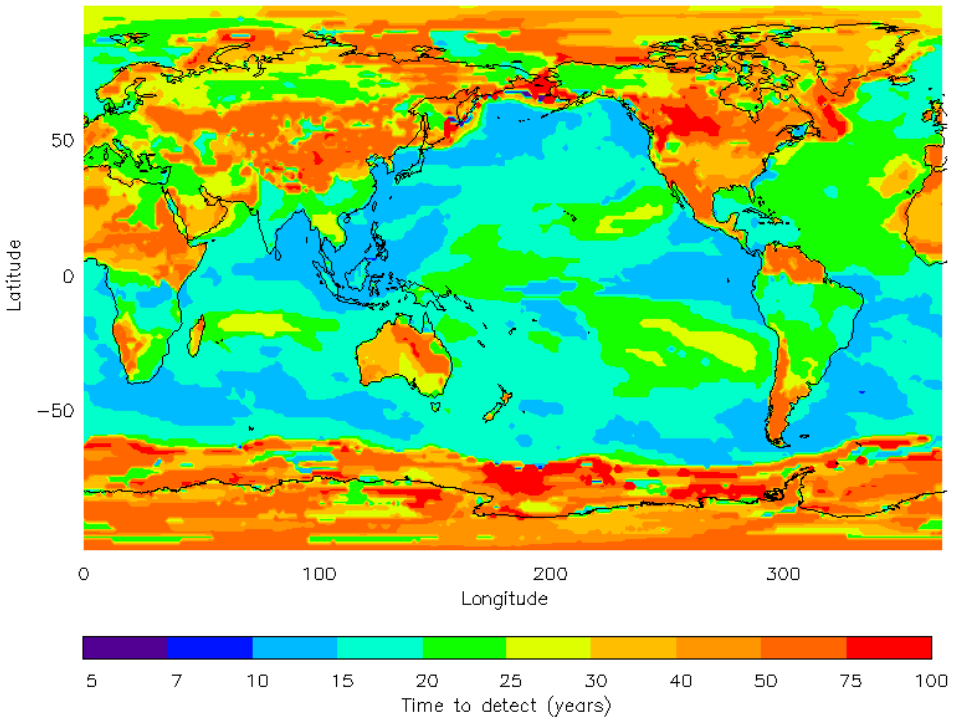


FIGURE 4.14: Map of detection times at 940nm, under clear sky conditions

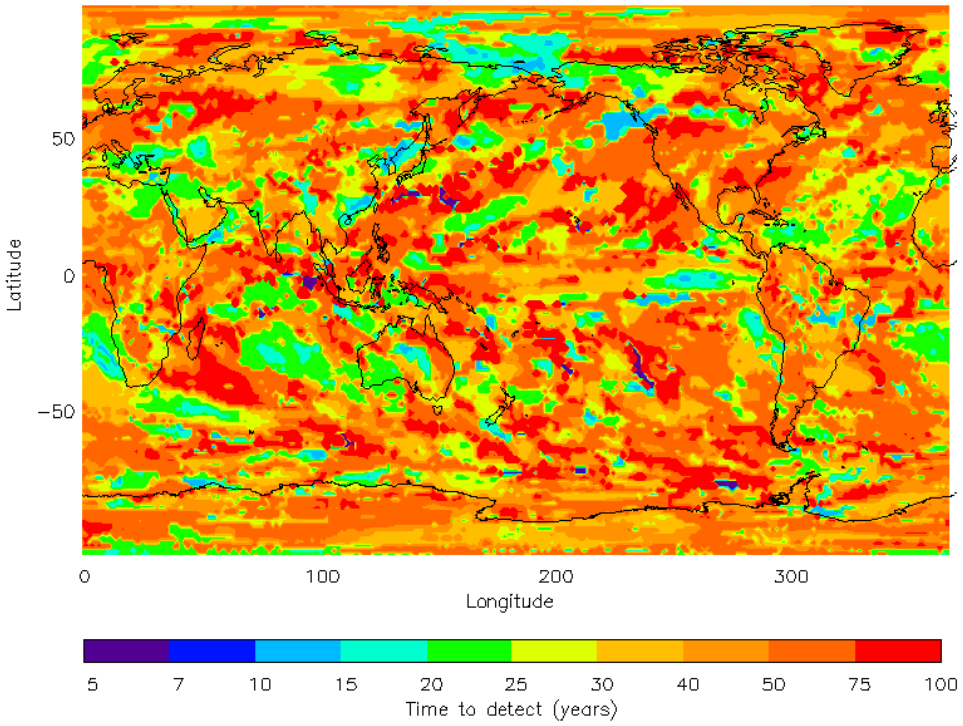


FIGURE 4.15: Map of detection times at 940nm, under all sky conditions

4.3.2 Land-Ocean Separation

The next stage was to specifically separate the data points into the land or ocean categories. To do this, a land mask was created at the same resolution as the COSSE data (Figure 4.16). This landmask was applied to the reflectance data to get two data sets - one for land, and one for ocean. These two data sets were then averaged into 1.41° latitude bands as before, and then the detection times calculated.

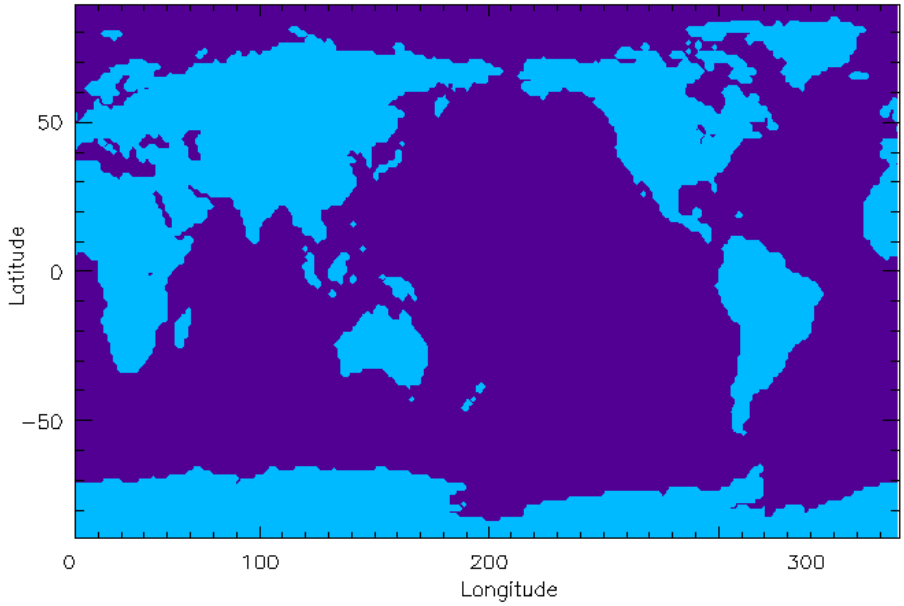


FIGURE 4.16: Land mask used for land-ocean separation

Figure 4.17 shows the detection times for each latitude band (y-axis) and for each wavelength (x-axis), as in Figure 4.10a, but using only the land grid points. Figure 4.18 shows the equivalent information but using only the ocean grid points, with both figures representing the clear sky only data. In Figure 4.17, there is a white band at 55-65°S which is due to the Southern Ocean which flows unhindered around the globe at these latitudes, passing between Argentina and Antarctica. There is a similar white band in Figure 4.18 due to Antarctica. Comparing the two figures, it is noticeable that the time to detect is significantly longer in the water vapour absorption bands over land than over ocean. As before, water vapour over a bright land surface has a greater effect on the TOA reflectance than when there is water vapour over a low albedo ocean surface. This sensitivity over land causes more variability in these regions and obscures

the aerosol induced signal, which in turn results in a longer time to detect than in the ocean case in Figure 4.18.

Looking closely at the water vapour absorption bands in Figure 4.17, the time to detect is lower in the Southern Hemisphere (0-40°S), at 15-25 years rather than 30-75 years from 0-50°N. In this southern region, the land is mostly forest in southern Africa and South America, as opposed to the deserts in the 0-30°N region, and so the effect is similar to that over the ocean, with a lessened effect of the absorption bands. In Figure 4.18, particularly between 40°N and 50°S, the time to detect is predominantly less than 15 years. While this quick detection time between 40°N and 50°S is seen in the ocean only data, it is not a surface change, but an aerosol effect - as the aerosol is concentrated over this region, the highly reflective aerosols over the dark background of the ocean increase the TOA reflectance significantly. An increase in aerosols over time would cause an increase in the TOA reflectance, and therefore a quicker detection time.

Comparing these plots to Figure 4.10a, it is possible to see how the land and ocean values average to give the combined detection times. The water vapour absorption bands in Figure 4.10a are clear but not as strong as in Figure 4.17, this is due to the fact that this central latitude region is mostly ocean, and so the ocean detection times dominate. It is interesting to note that the detection times are sometimes shorter when considering both surface types together, rather than separately. For example, at 51°N, the time to detect at 400nm is 30-40 years in both Figure 4.17 and Figure 4.18, whereas in Figure 4.10a is 25-30 years. The specific detection times are 32 years over ocean, 35 years for land, and 29 years for the combined data. In these regions, the signal of change is masked by large noise when land and ocean are considered separately. However, when the data is averaged into latitude bands, the noise is reduced, resulting in the signal being detectable. While the detection time in the combined data is only 3-6 years shorter, any time that can be saved in order to detect a signal is important.

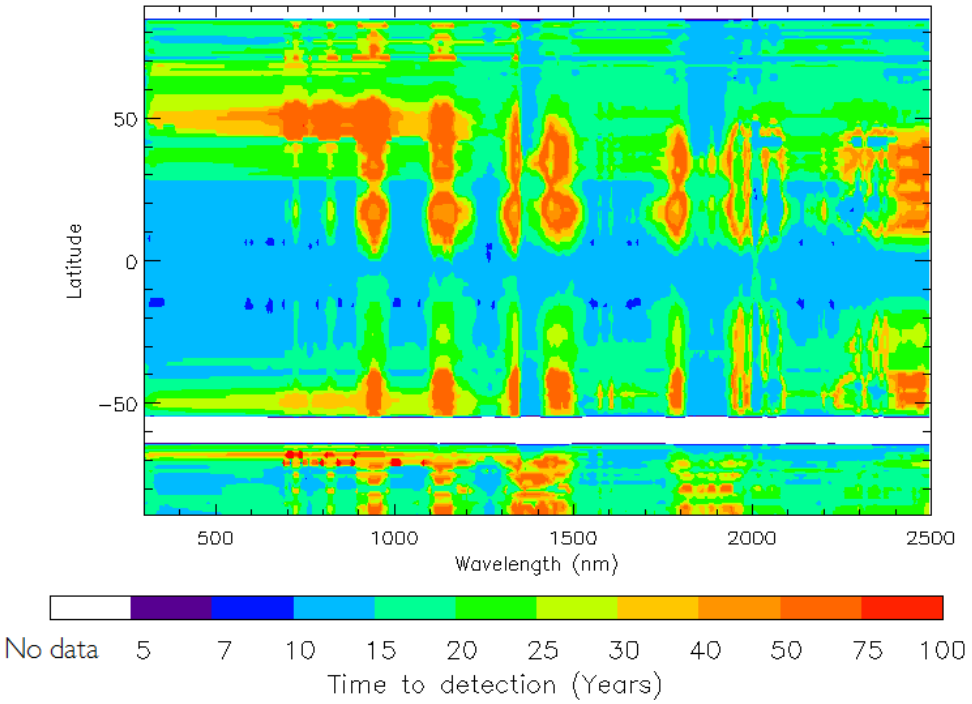


FIGURE 4.17: Time to detect over land under clear sky conditions for each wavelength and each 1.41° latitude band.

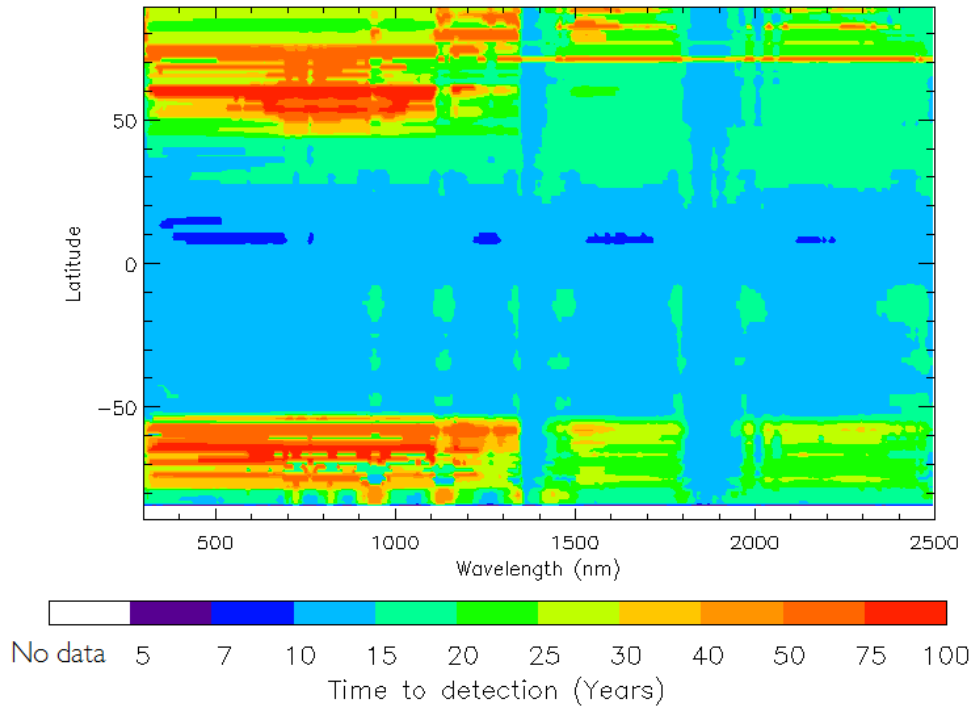


FIGURE 4.18: Time to detect over ocean under clear sky conditions for each wavelength and each 1.41° latitude band.

Figures 4.19 and 4.20 also show the time to detect for each latitude and wavelength, for land and ocean respectively, but now for all sky conditions. As discussed previously, in these cases the time to detect is typically longer under all sky conditions, due to the cloud providing additional noise. In these two figures, the water vapour absorption bands are very noticeable over both land and ocean, with the all sky case exhibiting obvious water vapour absorption bands over the ocean. The clouds introduce a significant amount of water vapour which obscures any climate change signal over both land types.

Comparing to Figure 4.10b which is the equivalent plot, but combines land and ocean together, the large detection times in the absorption bands are the main features. Figure 4.19 shows a large time to detect at 30-50°S, but this feature is not seen in the combined example in Figure 4.10b. At this latitude, there is mostly ocean, and so in the combined land-ocean averaging the lower ocean detection times dominate. This also occurs at 50-80°N for the opposite case - this region is predominantly land, and so the long detection times exhibited in Figure 4.20 from 300-1300nm are reduced and the average in Figure 4.10b is dominated by the lower detection times in Figure 4.19.

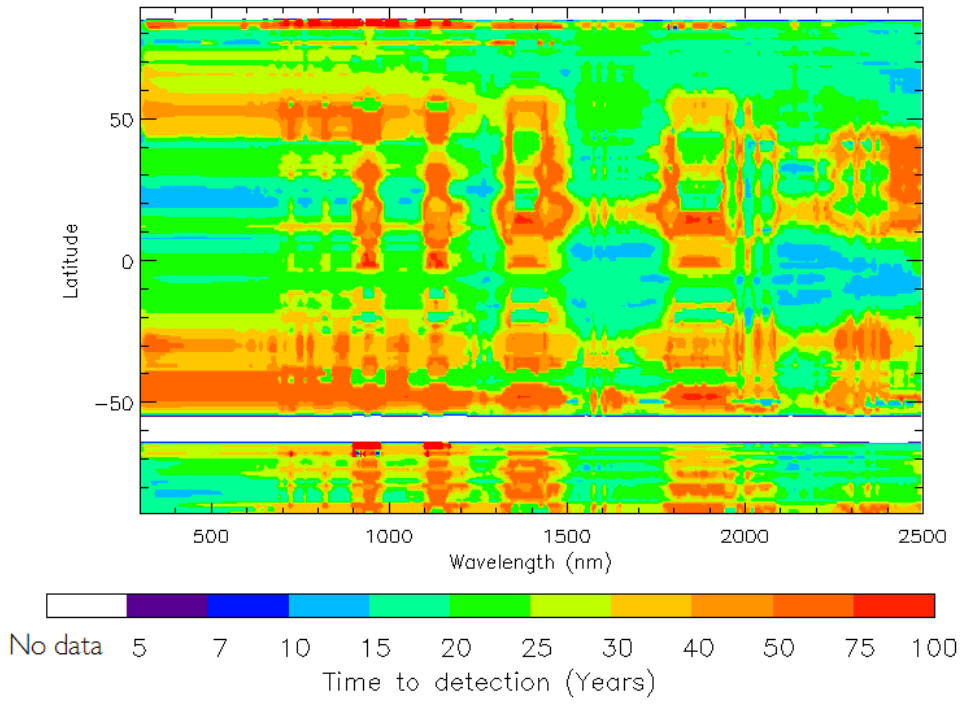


FIGURE 4.19: Time to detect over land under all sky conditions for each wavelength and each 1.41° latitude band.

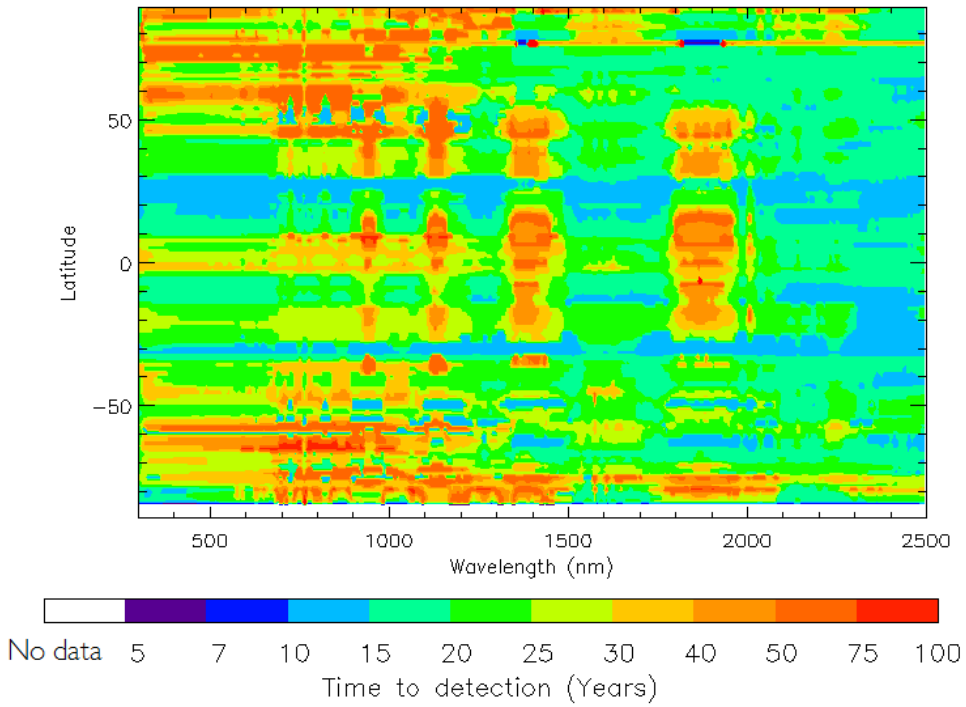


FIGURE 4.20: Time to detect over ocean under all sky conditions for each wavelength and each 1.41° latitude band.

4.3.3 Summary

In this section, the effect of separating the data points into land and ocean for calculating the detection times was investigated. It was again shown that the detection times are often lower between 50°N-50°S. An interesting result was that in comparing land and ocean, the time to detection in the water vapour absorption bands under clear sky conditions was longer over land compared to ocean. Under all sky conditions, both land and ocean are similarly affected by these water vapour absorption bands which increase the all sky detection times from approximately 10-25 years at transparent wavelengths, to 30-75 years at the water vapour absorption bands. While there are some regions that show very high detection times when separating into land and ocean in the all sky cases (above 50° in both hemispheres for ocean, and from 30-50°S for land), these are diluted when the data is averaged across both land and ocean. This shows that separately, the signals of change are obscured by larger noise, but by averaging the latitude bands, the noise is reduced and the signal can be detected. Overall, this, in conjunction with the results of Sections 4.2.2 and 4.3, suggests that there is no gain by separating the data points into land and ocean, and that full 10° latitude bands provide the best approach for minimising the time in which a signal of climate change may be expected to be detected.

Chapter 5

Effect of data gaps on detection times

So far in these studies, only a 100 year continuous data set has been used. However, it is unrealistic to expect to be able to obtain continuous measurements for this length of time. While there are satellites that have been functioning for nearly 20 years, such as MODIS or CERES, the anticipated lifetime of TRUTHS is approximately 3.5 years as a minimum, with hope this will extend to 5 years. For this reason, it is important to explore non-continuous, or gapped, data sets to fully understand the capabilities of TRUTHS-like satellites. The aim of this chapter is to investigate the impact of adding gaps into data on the time to detect a signal. It will also give an indication of how many TRUTHS-like satellites are required to confidently detect a signal, and the maximum gap 'allowed' between satellites, before the results begin to be compromised. It is expected that there will be a point at which TRUTHS would lose its ability to detect the small signals of climate change quickly, i.e. the time to detect would increase to a level that is achievable by other satellite instruments. The impact of measurement uncertainty on the detection times will also be considered in this chapter.

5.1 Method

For these studies, the 10° latitude band averaged data (introduced in Chapter 4) were used. The 10° data were employed following the conclusions drawn in Chapter 4; that there is little to be gained from using the high resolution 1.41° data. Also, the following

analysis was carried out on the 8 wavelengths that have been considered throughout this research - 550nm, 660nm, 865nm, 940nm, 1375nm, 1600nm, 1680nm and 2190nm. The full reasoning for these specific wavelengths is discussed in Chapter 2, but these wavelengths cover transparent regions, water vapour absorption bands, or are used by various satellite instruments for vegetation identification, for detecting cirrus clouds or ice clouds, or for drought analysis.

As in Chapter 4, the time to detect is calculated here using Equation 4.3, however the time series analysis performed prior to this is different to the method in Chapter 4. In Chapter 4, the noise from the control run COSSE data was used as an estimate for the noise in the COSSE data for the A2 scenario. However, in a real life scenario, having a control run data set to compare against and calculate the noise from would not be possible. By putting gaps into the time series, the aim is to simulate real life conditions, and in order to do this, a different method was chosen. Therefore, a multiple linear regression model with AR noise by Myles Allen was used (Allen, (1999)), which directly estimates the noise from the A2 scenario data. The model computes the linear fit to the data, and then the AR(1) noise as well as the white noise. From these variables, the autocorrelation of the noise, the standard deviation of the white noise, and the trend are calculated. These three values are then input into the time to detect equation, Equation 4.3. Henceforth, the method used in Chapter 4 is referred to as the 'original method', and the method used in this chapter is referred to as the 'linear regression model'.

The linear regression model is an iterative process that cycles through up to a maximum of 40 iterations in order to fit to the data and allow the code to converge. Successful convergence is assessed by comparing to a user-defined tolerance level. For this study, the optimal tolerance level was derived for each of the wavelengths analysed, by trial and error. This was in order to maximise the number of locations of convergence, while still allowing the code to function properly. Non-convergence did occur within the data set for a few locations and wavelengths. Examination of the data and convergence errors showed that the code failed to converge if the autocorrelation of the noise was very small - less than approximately 10^{-28} (compared to autocorrelation that was

of the order 10^{-6} on average). If the code did not converge, the required output variables were automatically estimated using an Ordinary Least Squares approach which introduced inconsistency into the analysis. For this reason, only points that indicated successful convergence were considered when assessing the detection time.

In order to test the new method, it was applied to the continuous time series for the selected wavelengths and the results were compared with the detection times from the original approach. It is important to recognise that besides the fact that the original approach uses noise statistics generated from the control run compared to the new method, which obtains estimates directly from the A2 scenario, the length of record analysed is also subtly different. In Chapter 4 detections can only occur after 8 years have elapsed since the first 5 years are used to set up the analysis. Using the new approach, all of the record is used, giving the possibility for detections to occur after 3 years. Hence, if there is no change in the trend and noise level, the new approach should detect change earlier. However, the trend and noise are not invariant and so differences of both sign may occur.

A comparison of the results under clear sky conditions are shown in Figure 5.1, where a) shows the detection times from the linear regression model, b) are the original detection times, and c) shows the difference between the two methods. Figure 5.2 shows the same information but for all sky conditions. The detection times in Figure 5.1a show that there are shorter detection times when using the linear regression model around the tropics, with longer detection times at higher latitudes around the Southern Ocean, Antarctic and Arctic (mainly in the visible wavelengths). There is also an increase in the detection times in the 940nm and 1375nm channels, reaching 50-75 years. Comparing with Figure 5.1b, the variation in the detection times across the latitude bands and wavelengths is very similar with typically lower values at low-mid latitudes and a more varied picture at higher latitudes, particularly at shorter wavelengths. However, it is clear that there are some differences in the actual values of detection time, particularly around the tropics. The results using the original method show a detection time of 10-20 years for a majority of 50°S-50°N for most wavelengths, whereas the linear regression model provides more detection times of 0-10 years in this region.

Figure 5.1c shows the differences between the two sets of detection times. This shows that a majority (88%) of the detection times from the two approaches are within $\pm$10 years of each other. As expected from the previous discussion, the new approach, inferring the noise directly from the A2 time-series, tends to give shorter detection times in the tropics and mid-latitudes. There are, however, some instances where the detection times are very different, reaching 30-50 years difference in one case. These cases primarily occur in the Arctic and Southern ocean for visible wavelengths and 940nm. As shown previously, in Chapter 4, these high latitudes tend to exhibit large variability due to sea ice melt and regrowth, and at 940nm the water vapour absorption obscures any signals, such that the largest differences are expected to occur in these regions and wavelengths due to the difficulties in unambiguously separating a trend from the underlying variability.

The all sky detection times from the linear regression model in Figure 5.2a show 10-20 year detection times in 56% of latitude bands and wavelengths, though there are still some regions that show a detection time of less than 10 years (12.5%). There is a significant increase in detection times at 940nm and 1375nm to 50-100 years, which is again expected from the results in Chapter 4. Examining the original detection times from Chapter 4, shown in Figure 5.2b, the times are longer. While there are instances of 10-20 year detection times, an equal number of the detection times are 20-30 years years. Figure 5.2b does also show the increase in detection times at 940 and 1375nm, however the detection times can be strikingly different to those in Figure 5.2a. For example, at 0-10°S, the 940nm detection time is 75-100 years with the linear regression model inferring the noise from the A2 scenario data, but 20-30 years using the original method.

Finally, Figure 5.2c shows that the difference between the detection times is $\pm$10 years in 76% of cases. While this is less than the 88% under clear sky conditions, it is still a significant percentage that shows good agreement between the methods. It also shows that the sign of the difference is mainly negative, as in the clear sky case, implying a quicker detection if the A2 scenario is used to calculate noise and trend. Compared to the clear sky case, there are more examples of larger differences between the detection

times. This is to be expected for the all sky case where there is inherently more variability in the time series - since it is essentially the estimation of the noise which differs between the two approaches.

Overall the results suggest that using the control run to characterise the noise in the A2 time-series typically results in an overestimate of the detection time, possibly indicating a corresponding overestimate in the noise level. Spatially and spectrally the pattern of the time to detection is very similar using both approaches.

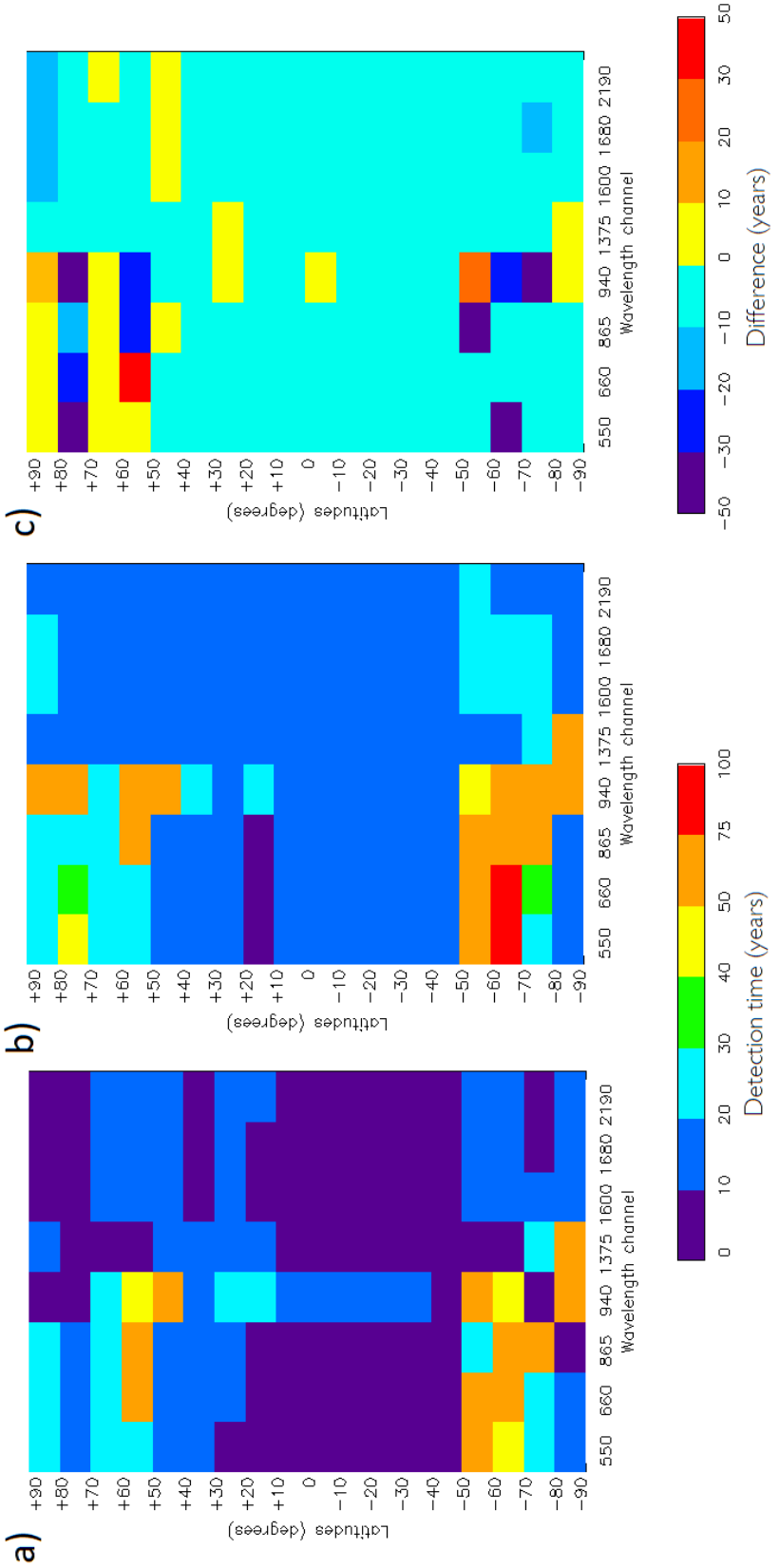


FIGURE 5.1: a) Detection times at each latitude band for 8 selected wavelengths under clear sky conditions, using the linear regression model, b) the corresponding detection times from Chapter 4, c) the difference in the detection times between the two methods (linear regression times minus original times).

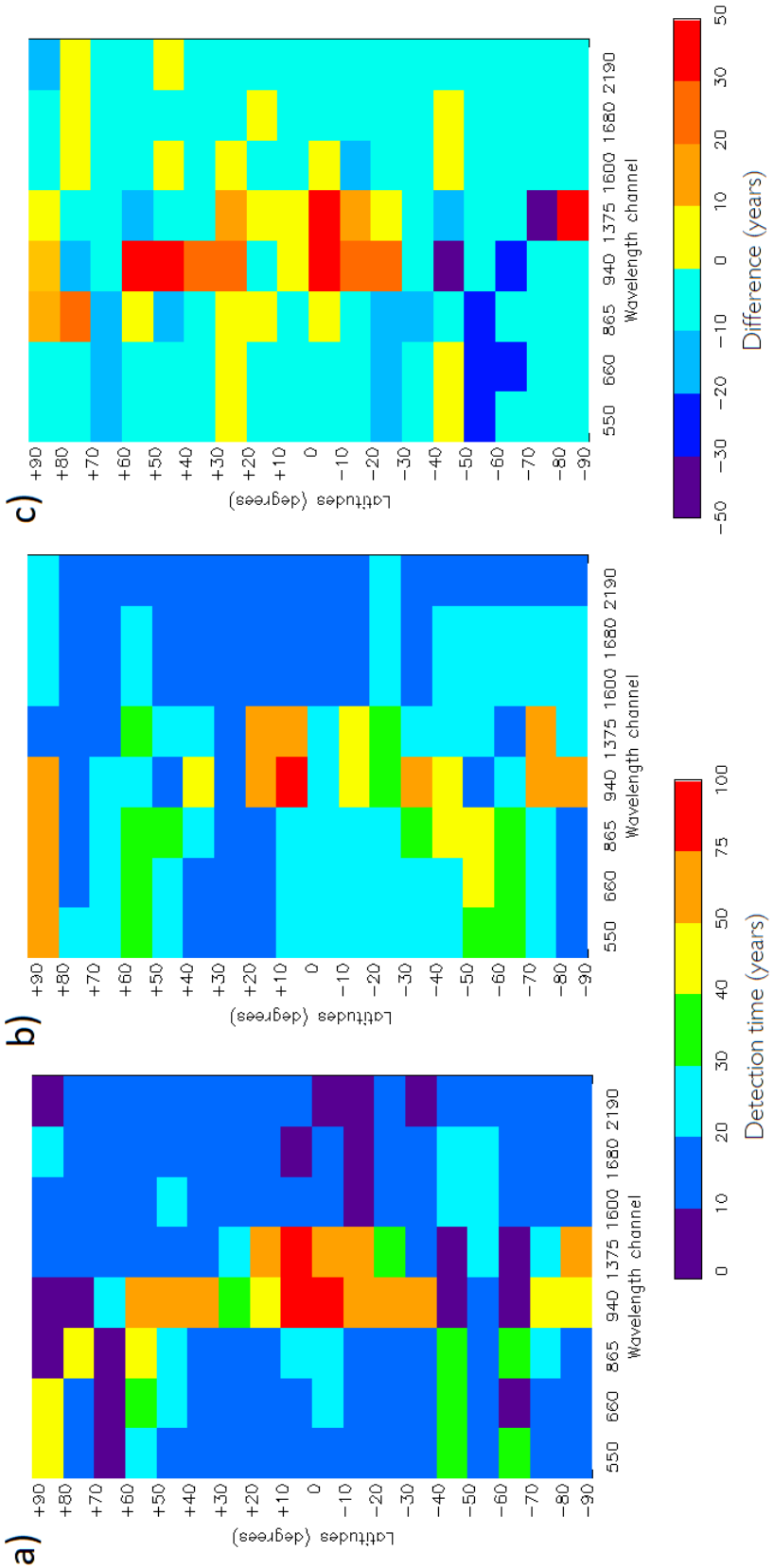


FIGURE 5.2: a) Detection times at each latitude band for 8 selected wavelengths under all sky conditions, using the linear regression model, b) the corresponding detection times from Chapter 4, c) the difference in the detection times between the two methods (linear regression times minus original times).

As mentioned previously, the main difference between the two methods is the fact that they characterise the noise differently. The original method in Chapter 4 uses the control run COSSE data to estimate the noise, rather than calculating the noise from the A2 scenerio COSSE data. To show how the noise is characterised differently by the two methods, an example was chosen by examining Figure 5.1c to look for a case where the detection times are very different. The chosen example is 660nm at the 50-60°N latitude band, which shows a difference of 30-50 years. The specific difference is 31 years, with the detection times for the original and linear regression methods at 26 and 57 years respectively.

Figure 5.3a shows the reflectance time series for the whole record for the clear sky example above at 50-60°N for 660nm. Figure 5.3b shows the noise time series up until the detection time for both methods. The noise in this case is the total noise, or N_t from Equation 4.2. In Figure 5.3 the black line shows the noise calculated by the linear regression model until the 57 years detection time, and the red line shows the noise calculated from the control run COSSE data using the original method until the 26 year detection time. It can be seen that the overlapping section of the noise time series are very different. During the first 10-15 years, the noise time series are almost anti-phase, with the rest of the time series showing little agreement. This shows how different the two methods are in estimating the noise in the TOA reflectance.

Regarding the detection times themselves, it is obvious that the linear regression model is detecting the signal (at 57 years) after the reflectance begins to decrease as shown in Figure 5.3a. The value of the trend at detection is -0.000105 yr^{-1} with the standard deviation of the white noise, σ, of 0.0035. The same values for the original method at the 26 year detection time shows a trend of 0.000258 yr^{-1}, which is larger than the trend when the linear regression model makes its detection (with σ = 0.0029). Examining the linear regression model at 26 years, the value of the trend is 7.5x10^{-5} yr^{-1} (with σ = 0.0025) which is significantly smaller than either trend at the respective detection times. This is why the detection is not made by the linear regresion model at 26 years. The difference in the trend, and ultimately the detection times, is due to the different methods of estimating the noise. The 26 year detection appears to occur during a

period of relatively constant TOA reflectance, but due to the noise being calculated from the control run COSSE and not the A2 scenario data, a positive trend emerges which causes the detection.

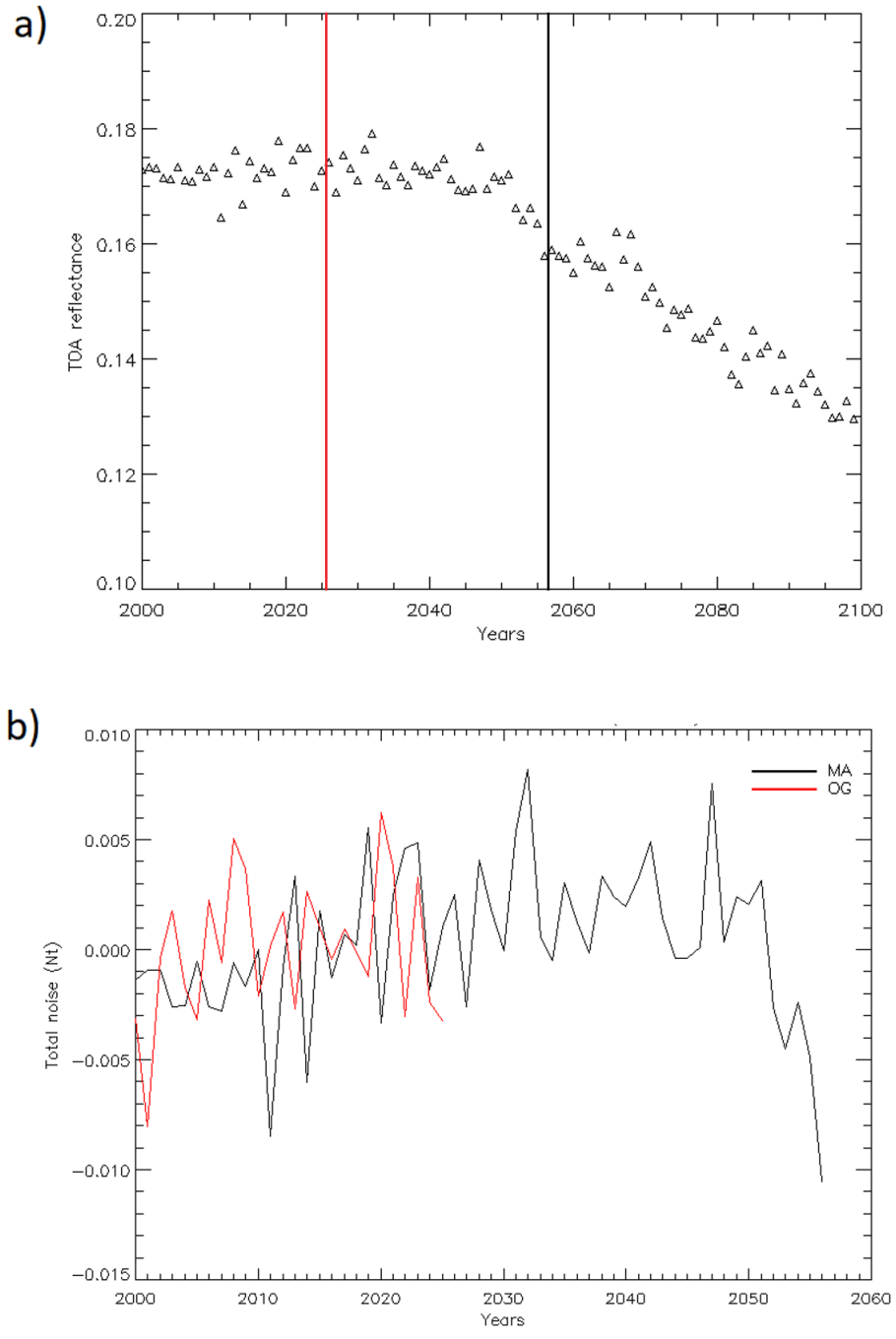


FIGURE 5.3: a) TOA reflectance at 660nm for the 50-60°N latitude band under clear sky conditions. Red line denotes 26 year detection time, black line denotes the 57 year detection time. b) noise time series until the respective detection times using the original method and the linear regression method. The black line represents the linear regression model, and the red line represents the original method.

In conclusion, the detection times were compared for the two methods for 8 wavelengths that have been used throughout these studies - 550, 660, 865, 940, 1375, 1600, 1680 and 2190nm. Typically, detection times are lower when using the A2 scenario to directly estimate the noise - for detections in less than 8 years this may be due to the different starting points of the two analyses, however this should not affect longer detection times. There are instances where there are marked inconsistencies in the detection times particularly at higher latitudes. These tend to be regions which were characterised by high variability in Chapter 4. Noticeable differences can also be seen at 940nm and 1375nm under all sky conditions. Again, based on the results in Chapter 4, both of these wavelengths exhibited high variability under both clear and all sky conditions, with correspondingly long detection times (Figure 4.10). Using the A2 scenario to estimate noise tends to increase these detection time estimates. Given they were already long, this increase is not so critical in the context of driving mission design. Indeed, it was already concluded in the previous chapter that 940nm, or other water vapour absorption bands, are not suitable for the swift detection of climate change signals under this emissions scenario.

The final stage of this analysis was to decide on the range of gaps, as well as realistic lifetimes for each TRUTHS instrument. Since the planned lifetime for TRUTHS is 3.5 years, with expectations to extend this to 5 years, 3 and 5 years were chosen as the options for satellite data in this analysis. The range of gaps chosen was 10, 15, 20 and 25 years. In summary, the gap configurations all begin with 3 or 5 years of satellite data, and are followed by a gap of 10-25 years, and this pattern is repeated. Therefore, an example of the data would be as follows; 3 years of data, 10 year gap, 3 years of data, 10 year gap and so on. This analysis of the data assumes that any subsequent satellites would be launched at regular intervals.

5.1.1 Idealised Time Series

As in Chapter 4, the method for the gap analysis was tested using specific values to show how the detection time varies with the three variables; trend (ω), autocorrelation of the noise (ϕ), and standard deviation of the white noise (σ). The same 'standard

values' were used in this section for consistency with Chapter 4 and were as follows - ω of 0.0005 yr^{-1}, ϕ of 0.1, and σ of 0.005. For this gap example, the gap configuration used was 5 years of data, with a 10 year gap. With these standard conditions, the detection time now becomes 33 years, compared to the original 21 years.

Table 5.1 shows how the trend affects the time to detect for both the original continuous example and the gapped example. The addition of a gap increases the detection time as expected, and the increase is smaller for the example with the larger trend. This is expected since a large enough trend would still be detectable early on and with fewer data points.

Trend (yr^{-1})	Continuous detection time (years)	Gapped detection time (years)
0.001	15	18
0.0005	21	33
0.00002	Undetected	Undetected

TABLE 5.1: Detection times for varying trends for an artificial time series.

Table 5.2 shows the detection times for a case which has varying magnitudes of noise, but with trend and autocorrelation kept at standard values, for both continuous and gapped data. As before, the addition of the gap increases the detection time, but interestingly, the detection times span just two years when there is a gap. This is compared to the nine year range for the continuous data.

Noise	Continuous detection time (years)	Gapped detection time (years)
0.01	30	34
0.0075	26	33
0.005	21	32

TABLE 5.2: Detection times for varying magnitudes of standard deviation of the white noise for an artificial timeseries.

Finally, Table 5.3 shows how varying the autocorrelation of the noise affects the detection time comparing continuous and gapped data. As seen in the above example for the standard deviation of the white noise, the detection times in the gapped example are within one year of each other, with two exhibiting the same detection time. This

implies that the autocorrelation of the noise has almost no effect on the detection time when there is gapped data. It is possible that the uncertainty in the detection time is dominated by the existence of gaps, and therefore the standard deviation of the white noise and the autocorrelation on the noise have a far smaller effect in these cases.

Autocorrelation	Continuous detection time (years)	Gapped detection time (years)
0.4	28	34
0.1	21	33
0.01	20	33

TABLE 5.3: Detection times for varying autocorrelations of the noise for an artificial timeseries.

5.2 Effect of Gaps in Climate Record

Having checked the performance of the linear regression model and its agreement with the detection times from Chapter 4, the effect of gaps in the TOA reflectance time series on the ability to detect a signal above natural variability can be investigated. The detection times were calculated at each of the eight wavelengths for each 10° latitude band, and for each of the gap configurations. Figure 5.4 shows the detection times for gapped data sets with 3 years of data available (Figure 5.4a) and for 5 years of data (Figure 5.4b) under clear sky conditions. Each wavelength band consists of 4 sections which provide the detection time whe using each of the 4 gap lengths - 10, 15, 20 and 25 years. Black squares represent areas where a signal was undetectable within the 100 year record.

Figure 5.4a shows that in most areas the detection times increase with increasing gap length which is intuitive since the longer the gap, the more delayed the next data set will be, which delays when it is possible to make a detection. Also, there are fewer data points available, which would increase the uncertainty in detecting a signal. Also, due to this factor, there is a limit in how short the detection times can be. For example, with a 25 year gap, it is unlikely to obtain a detection time below 30 years, and therefore this must be considered when analysing the detection times.

The detection times in Figure 5.4a are mostly below 30 years, however there are several areas that display longer detection times. It can be seen that there are two main regions where the detection time is particularly long - 30-70°N (at shorter wavelengths), and 60-70°S (at all wavelengths). This is consistent with results from Chapter 4 which showed longer detection times at higher latitudes, around the poles, due to ice melt and regrowth and the variability caused by this process. It is noticeable that 940nm has longer detections times in this figure, which is also expected given the results in Chapter 4 and in Figures 5.1 and 5.2.

There are obvious differences in Figure 5.4b which uses 5 year periods of data compared to Figure 5.4a. The tropics and mid latitudes show more consistency in the detection times with less global variation, and detection times predominantly below 30 years. This is compared to Figure 5.4a which show several areas of 40-100 year detection times in the tropics and mid latitudes. Figure 5.4b does still show the longer detection times around the poles that are seen in Figure 5.4a at 550-940nm. However, the gap configurations with 5 year records allow shorter detection times at 940nm at the tropics, compared to the 3 year records.

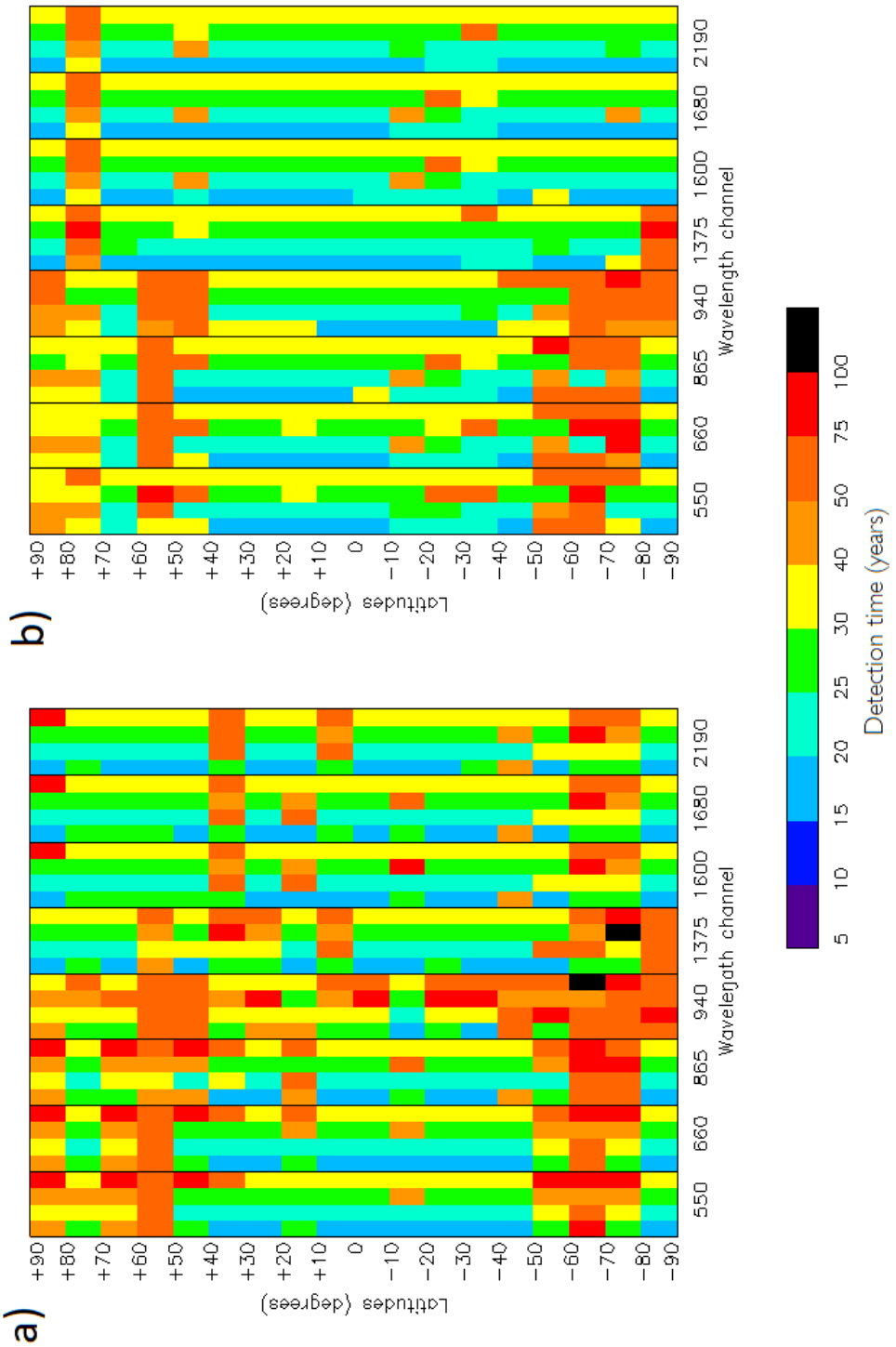


FIGURE 5.4: a) Detection times using 3 year periods of data, for each latitude band and wavelength under clear sky conditions. b) The same as a) using 5 year periods of data. Each wavelength band comprises of 4 detection times signifying the detection time for increasing gap length; 10, 15, 20 and 25 years respectively. Black areas represent no detection within 100 year record.

In most regions, the detection times increase with gap length, and as mentioned previously, this is due to the increasing gaps pushing the possible detection times later. An example of this is shown in Figure 5.5a which displays the TOA reflectance at 1600nm for 0-10°N, under clear sky conditions. This figure is for the example of 3 years of data, with a 20 year gap, and shows the full record with grey panels covering the data points not used in this specific configuration. There are also coloured data points on Figure 5.5a that show the data points used for each gap configuration - blue represents the 10 year gapped data, the green represents 15 year gapped data, and finally red represents the 25 year gaps. These values have been offset from the real time series for clarity and are each offset by approximately 0.0015. The specific detection times for this example for all four gap lengths are 16, 21, 26 and 31 years. Figure 5.5a shows that initially there is a very strong trend with small interannual variability, and all of the four detection times occur within this region of strong positive trend. In these cases, the trend is so strong that despite the gap length, the signal will always be detected during the second 3 year record, which is apparent by looking at the coloured data points in Figure 5.5a. This explains why the detection times simply increase by 5 years as the gap length increases by 5 years. Figure 5.5b shows the trend and standard deviation of the white noise for each data point used for the specific example of 20 year gaps. It also displays the value of the main body of Equation 4.3 which is $(3.96\sigma/\omega)^{2/3}$ and denoted by 'Eqn' in the following figures. These values have been plotted to show the relationship between the trend and standard deviation of the white noise as represented in the time to detect equation. In the linear regression model, ϕ is approximately zero implying that the main body of Equation 4.3 can be simplified to the above. This figure shows that detection occurs where the trend is larger than the standard deviation of the white noise, behaviour which acts to reduce the right-hand side of equation 4.3 such that detection is possible.

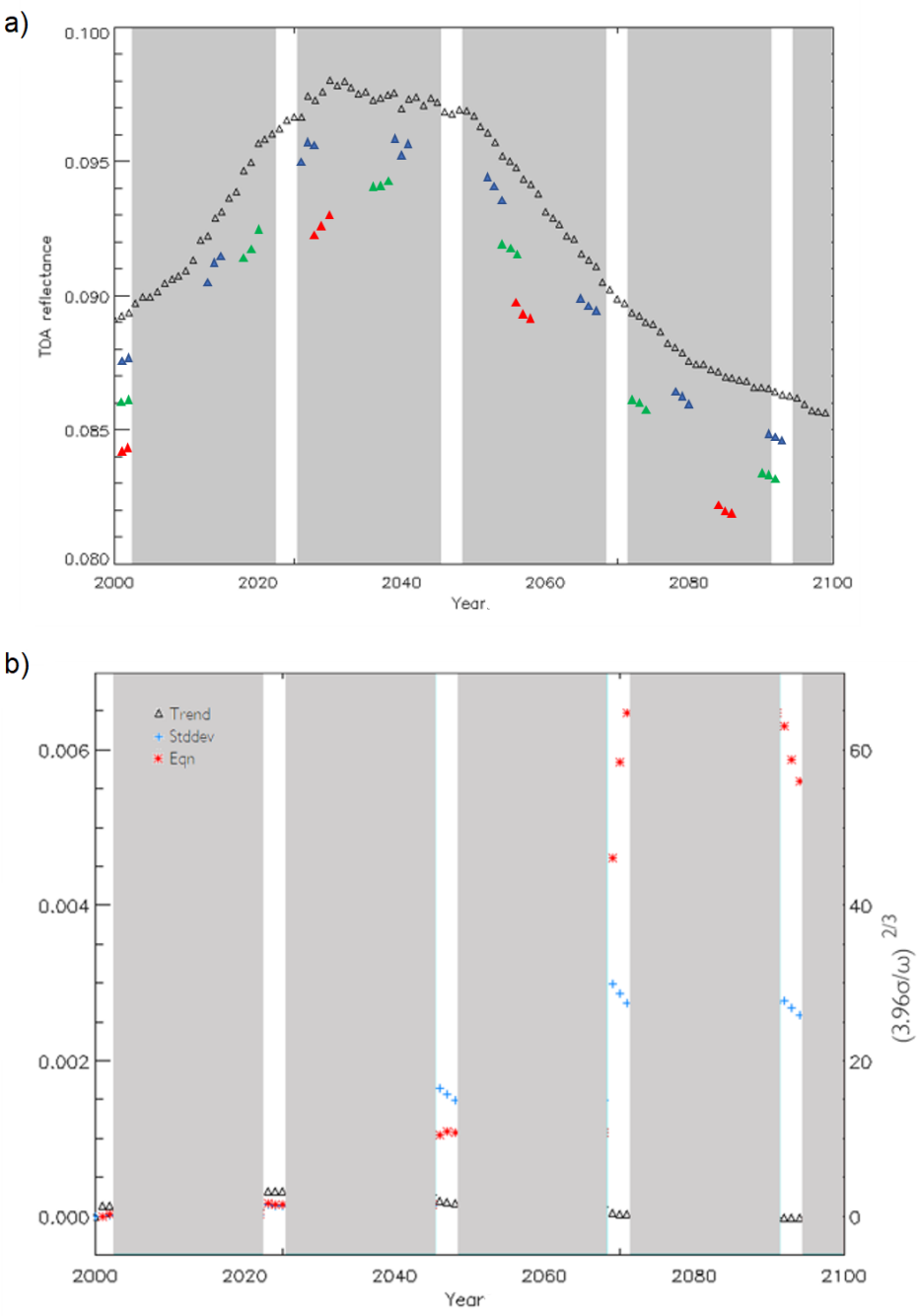


FIGURE 5.5: a) TOA reflectance under clear sky conditions at 1600nm for the 0-10°N latitude band. The grey panels show the 20 year gaps between 3 year periods of data and therefore the data points that are not used in calculations. The blue, green and red data points represent the points used with 10, 15 and 25 year gaps respectively, and are offset for clarity. b) the trend, standard deviation of the white noise, and the main body of Equation 4.3 at each data point for a 20 year gap.

In some regions, however, there is counter intuitive behaviour in the progression of detection times with gap length. For example, the case of 660nm under clear sky conditions for the latitude band 60-70°S. At this location, using 3 year periods of data the detection times vary as follows with increasing gap - 68, 55, 49 and 87 years, and it is important to understand why this behaviour is seen. Figure 5.6a shows the TOA reflectance for this example, for the gap configuration of 3 year record length with 20 year gaps shown by the grey panels. Again, the coloured points represent the data used in each of the other gap configurations (blue for 10 years, green for 15 years, and red for 25 years) and are offset from the main time series for clarity as before. This figure shows that the reflectance is initially very noisy, with no discernable trend emerging until approximately 2050. Figure 5.6b shows analogous information to Figure 5.5b. Compared to Figure 5.5b, the values here are highly variable. While the trend is never larger than the standard deviation, the detection at 49 years occurs when the trend is at its largest. Detection also occurs when the value of $(3.96\sigma/\omega)^{2/3}$ and the standard deviation of the white noise are both relatively low compared to the values at other years. For example, the average of the 3 points at which detection occurs (years 2046, 47, 48) show an average value of 27 for $(3.96\sigma/\omega)^{2/3}$ compared to an average of 40 for the previous 3 year data set. The average standard deviation on the white noise for the same time periods are 0.0054 and 0.006 respectively.

The variation in the detection times with increasing gaps is in part an artefact of the method. With each gap length, different data points are used to calculate the detection time. It may be that the values sampled for one gap configuration are all similar in value and therefore show no trend over the time series. In contrast, a different gap configuration may make use of different points that show a stronger trend and would therefore give a shorter detection time. In the case for 660nm above, there is no real trend until after 2050, and so the detection in most gap configurations occurs during the first 3 year record that is placed after this 2050 point. This 3 year period naturally occurs at different times due to the gap length, giving the variation in the detection times, as shown by the coloured points. For the case shown in Figure 5.6a with the detection time of 49 years, the data points sampled would result in a linear fit with a slightly positive linear trend, allowing a detection at this time. Whereas, the coloured

points show that in those examples there is some variation in the reflectance values, which means that a detection is not made until later on, when the stronger negative trend has begun. This dependence on the precise points selected is more of an issue with cases that have a large standard deviation of the noise and/or a low trend, and not in cases such as 1600nm in Figure 5.5.

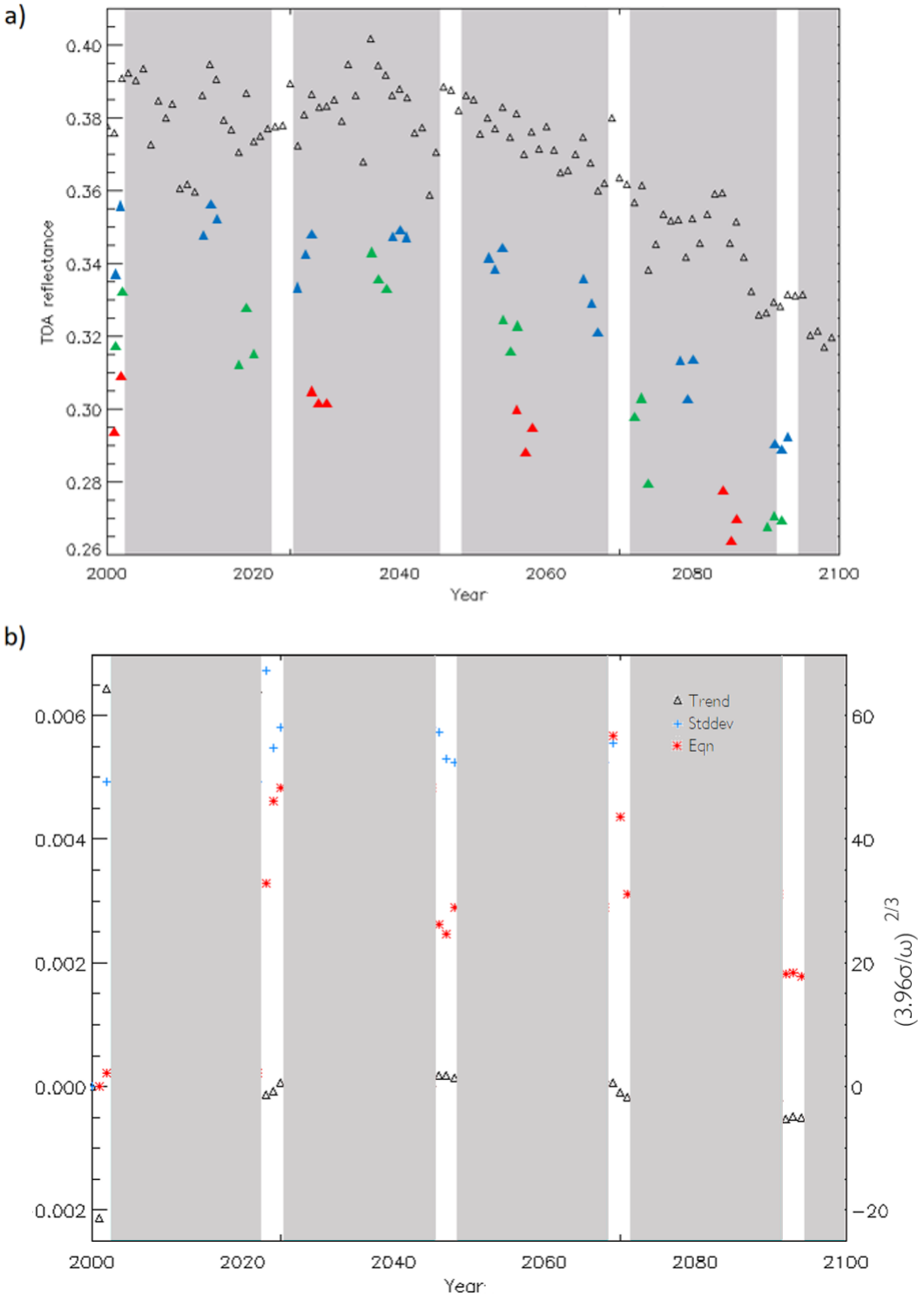


FIGURE 5.6: a) TOA reflectance under clear sky conditions at 660nm for the 60-70°S latitude band. The grey panels show the 20 year gaps between 3 year periods of data and therefore the data points that are not used in calculations. The blue, green and red data points represent the points used with 10, 15 and 25 year gaps respectively, and are offset for clarity. b) the trend, standard deviation of the white noise, and the main body of Equation 4.3 at each data point.

Figure 5.7 shows analogous information to Figure 5.4, but for all sky conditions. As seen in previous studies in Chapter 4, the detection times increase under all sky conditions. This change is significant in Figure 5.7a which shows that detection times are now predominantly in the 40-100 year range. There are, however, still some latitude bands where detection can occur at less than 30 years. For example, 10-20°S provides low detection times of 15-30 years for most gap configurations, similar to those under clear sky conditions at almost all wavelengths, excluding 940nm and 1375nm. In fact, at some gap configurations, e.g. a 20 year gap at 550nm, the detection time is shorter in the all sky case. The shorter detection times at the longer wavelengths (1600, 1680 and 2190nm) seen in the clear sky case are still apparent in some regions, particularly in the northern latitudes, but the long 40-100 years detection times are fairly widespread.

Figure 5.7b displays very different results to the 3 year data sets considered in Figure 5.7a. The detection times in the majority of regions are on par with the clear sky detection times of 15-30 years, increasing steadily with the gap length. The major difference in Figure 5.7b compared to the clear sky equivalent (Figure 5.4b) is that there is a significant increase in the detection times at 940nm and 1375nm. In the clear sky scenario, the detection times were 15-40 years around the tropics for 940 and 1375nm, however in the all sky case the detection times are 50-100 years in the same region. As seen in the clear sky cases (Figure 5.4), the detection times are mostly <30 years with several areas of 15-20 year detection times at 1600, 1680 and 2190nm. Though Figure 5.7b shows that these detection times are consistently low at all latitude bands with the shortest time at 15-20 years (ranging to 30-40 years for the 25 year gaps). This is compared to the equivalent plot for the clear sky case, where Figure 5.4b shows longer detection times at 70-80°N of 30-75 years. The results suggest that under all sky conditions, with a 5 year record length a 10 year gap, signals of change above the natural variability can be detected within 20 years in several wavelength bands across a wide range of latitudes.

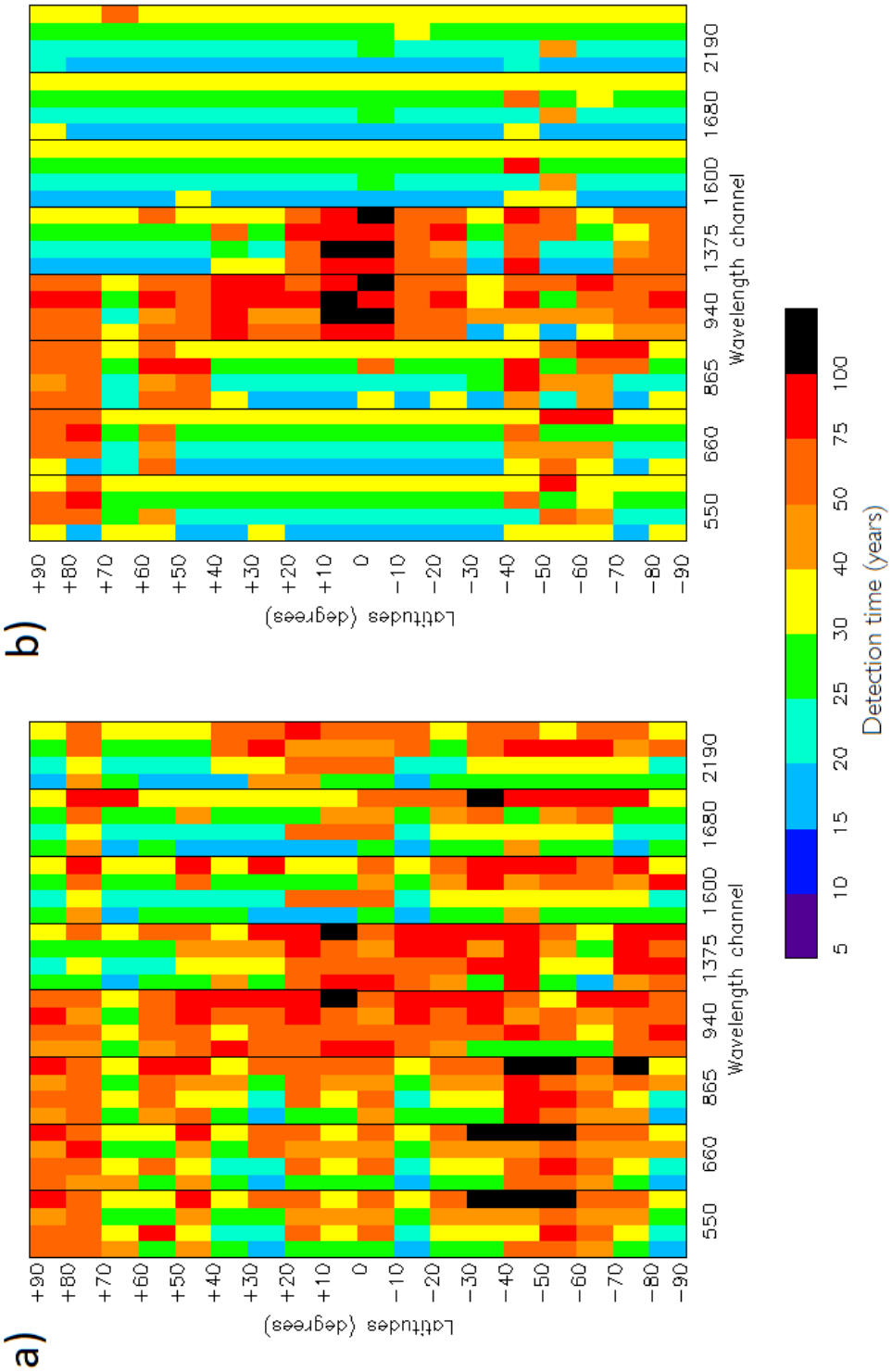


FIGURE 5.7: a) Detection times using 3 year periods of data, for each latitude band and wavelength under all sky conditions. b) The same as a) using 5 year periods of data. Each wavelength band comprises of 4 detection times signifying the detection time for increasing gap length; 10, 15, 20 and 25 years respectively. Black areas represent no detection within 100 year record.

Previously, the 0-10°N latitude band at 1600nm was examined as a 'well-behaved' example. The results for the same region in the all sky example in Figure 5.7b, using 5 year records also leads to the increasing detection times with gap length. However, Figure 5.7a shows that, when using 3 year records, the detection time reaches 50-75 years for a gap length of 15 years. This is compared to 20-25 years for the same gap length using 5 year records. Figure 5.8a shows the TOA reflectance time series for 0-10°N at 1600nm with grey panels representing the 15 year gaps between 3 year data sets, and Figure 5.8b shows the same as (a) with 5 year data sets. This figure shows that the reflectance has a strong trend in the first 30 years, and while there is more variability in the data under all sky conditions due to the effect of clouds, the noise is not obscuring the signal. This shows how the detection times increase with increasing gap length (as discussed for the clear sky case). Considering Figure 5.8a where the detection time is 50-75 years, it appears that the signal should be detectable earlier. However, output from the linear regression model shows that the model does not converge until the latter half of the record. Therefore the detection does not occur until 2056. As discussed previously, a lack of convergence occurs when the calculated autocorrelation of the noise is very small. This lack of convergence hinders the ability to detect a signal. Whereas, with the 5 year record, the linear regression model converges sooner and so the detection time is much faster, and the detection is made during the strong positive trend in the first 30 years of the record.

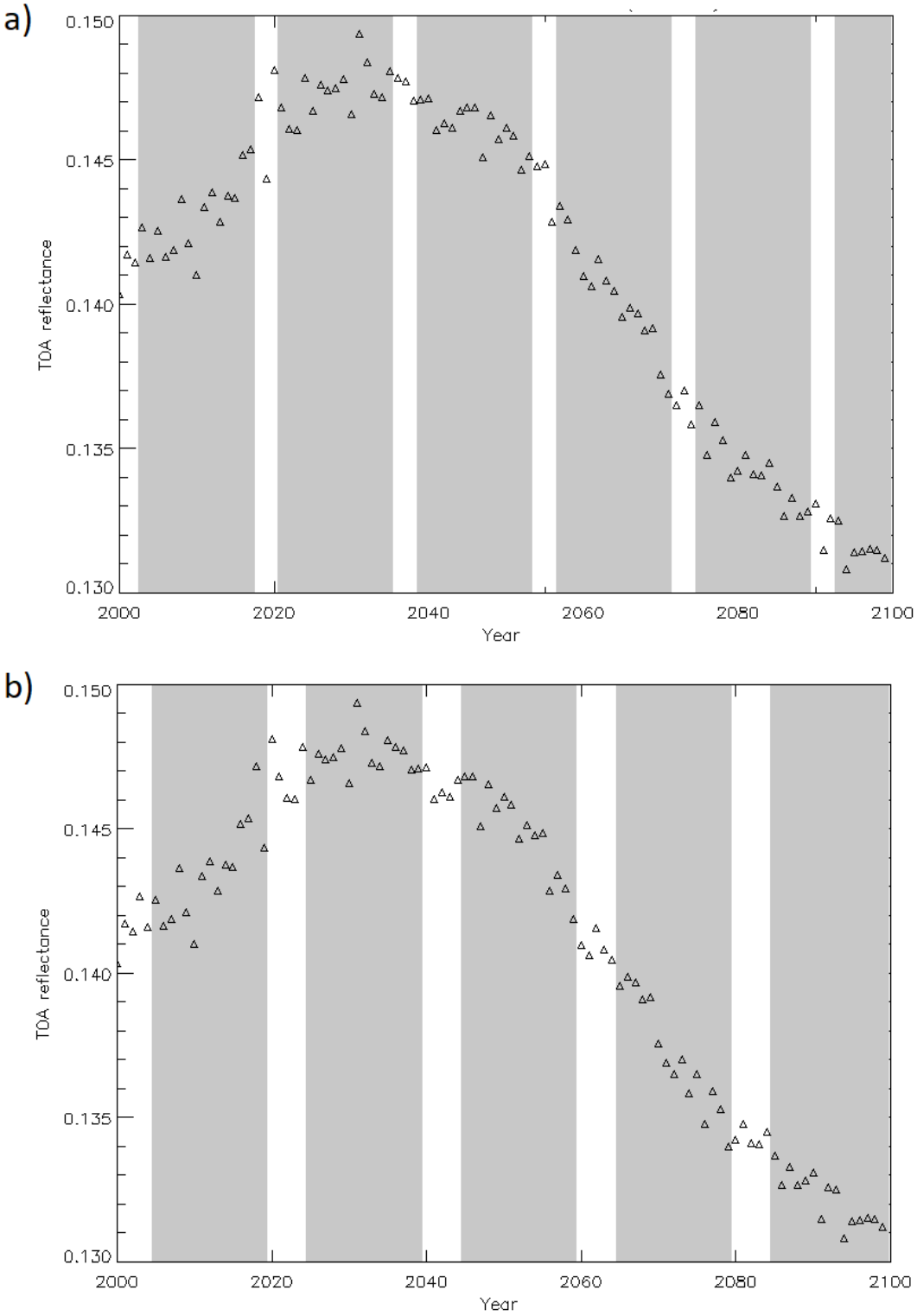


FIGURE 5.8: a) TOA reflectance for 0-10°N at 1600nm using 3 year data sets, with grey panels representing 15 year gaps, b) the same as (a) using 5 year data sets.

5.3 Effect of measurement uncertainty

So far, these analyses have not considered any instrument error in the calculations of the detection times. The aim of this section is to include the measurement uncertainty into the calculations, to further improve the estimates made so far of the detection times. In order to test the method, the detection times were first calculated for the continuous all sky data. Then, having shown in the previous section that a combination of 5 years of data with 10 year gaps will provide the shortest detection times, this is the example that will be used here in order to consider the impact of measurement uncertainties. Only the all sky data set will be used since clear sky measurements are less likely to be taken.

In order to do this, a method was used from Leroy et al., (2008), which was also later used in Feldman et al., (2011)(b). In Leroy et al., (2008) it was shown that you can allow for an 'imperfect measurement' as well as natural variability by multiplying the detection time equation (4.3) by a factor of $(1+f^2)^{(1/3)}$, where f^2 is explained by Equation 5.1.

$$f^2 = (\sigma^2_{meas}\tau_{meas})/(\sigma^2_{var}\tau_{var}) \tag{5.1}$$

Here, σ^2_{meas} is the measurement uncertainty, τ_{meas} is the correlation time for the measurement uncertainty, σ^2_{var} is the natural variability and τ_{var} is the correlation time for natural variability (Leroy et al., (2008)). In this case, the measurement uncertainty is the instrument error of 0.3% in the reflected shortwave radiation. As previously discussed, this equates to $6x10^{-4}$ reflectance units Feldman et al., (2011)(b)). The correlation timescale, τ_{meas} is the satellite lifetime which will be 5 years in this example. The second correlation timescale, τ_{var}, is set to 1 year to keep it in line with the AR(1) process that has been used throughout (Feldman et al., (2011)(b)). Finally, the natural variability was calculated from the all sky control run data since this data set only shows natural variability and no trend, therefore a good estimation can be made for the magnitude of the natural variability.

For these experiments, the natural variability was calculated at each latitude band and for each wavelength. Initially, the new detections times accounting for measurements uncertainty were calculated for the continuous data set with the added factor, $(1+f^2)^{(1/3)}$, using the values discussed here, to gauge the impact of uncertainty.

Figure 5.9 shows the detection times for the continuous data set for all sky conditions. Figure 5.9a shows the original detection times (as shown previously in Figure 5.2a), while Figure 5.9b shows the detection times when also considering the measurement uncertainty. The detection times increase due to the inclusion of measurement uncertainty which was expected, since the previous method assumes a perfect measurement. It is still clear that the water vapour channels lead to significantly longer detection times, and that the visible and longer wavelengths have shorter detection times as before. In the visible bands, the detection times have increased from 10-25 years to 15-25 years around the tropics. This increases isn't too large and so in this case the signals would still be detectable relatively quickly. Similarly, the detection times at 1600/1680/2190nm have increased from predominantly 3-20 years, to mostly 10-25 years (with some exceptions). Again, this increase is not too severe at all latitudes. In summary, while there is an increase in the detection times, in most regions and wavelengths, the increase is manageable and signals would still be detectable.

Next, the same calculations were performed for the gapped time series. Figure 5.10a shows the detection times as calculated previously for Figure 5.7b for just 10 year gaps. Figure 5.10b shows the same but having included the measurement uncertainty into the detection time calculations. Comparing the two panels, it is clear to see that there is an increase in the detection times due to the measurement uncertainty and natural variability. This is to be expected since the previous example assumes perfect measurements. Firstly, it is immediately clear that there is now an area where a signal is undetectable - at 0-10°S at 940nm and 1375nm. It is also now even more difficult to make any detection at these two wavelengths, supporting the idea that it would be best not to use water vapour absorption channels in order to make quick detection of signals.

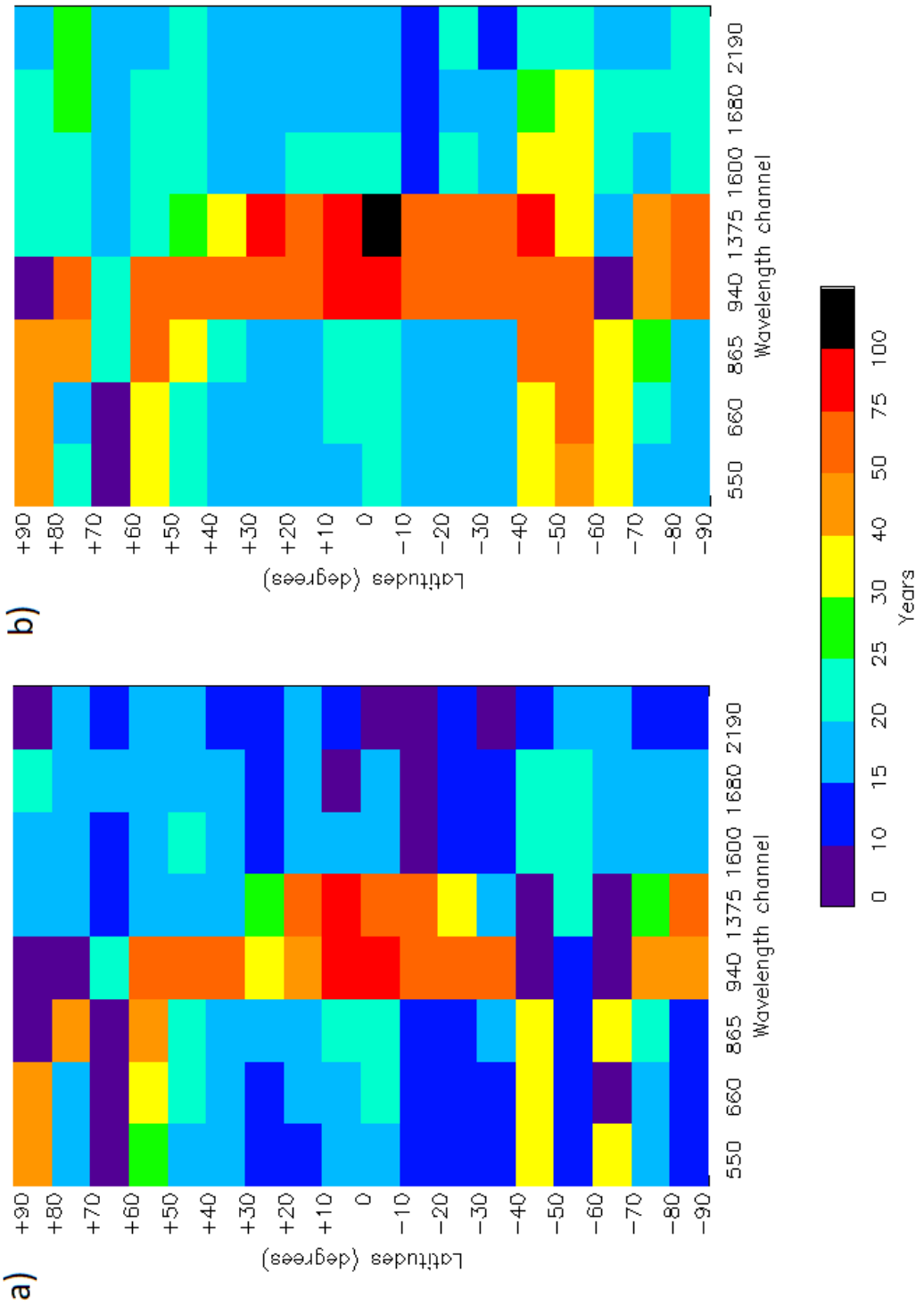


FIGURE 5.9: a) The detection times under all sky conditions for the continuous data set, b) the same as (a) accounting for measurement uncertainty.

Previously, 1600/1680/2190nm provided the fastest detection times of 15-20 years at almost all latitude bands (5.10a), however in Figure 5.10b there is a significant increase in the detection times, with several regions now as high as 30-40 years. This is an

important result as previously these wavelengths were proving to be the best wavelengths at which to make faster detections. The tropics still have faster detection times of 15-20 years, however it is predominantly the midlatitudes and poles that show an increase in detection times. This may be due to the larger natural variability in these regions.

Finally, the visible wavelengths also show some large increases in detection times. As at the long wavelengths, the detection times around the tropics remain the lowest at 15-20 years for 550 and 660nm. However, north of 30°, the detection times are all 30-75 years (with one case of 75-100 year detection time). This is the same as for 40-90°S which now ranges 30-100 years, with one anomaly of 15-20 years. Again, this is likely due to now accounting for natural variability as well as measurement uncertainty.

It is interesting to see how the detection times have changed due to the measurement uncertaitnty. While TRUTHS is planned to be one of the most highly accurate EO satellites, this section shows that when everything is taken into account, only 30% of the examined cases now have a detection time of 15-20 years. The remaining wavelengths and latitude bands predominantly having detection times of over 30 years. While the areas of low detection time are more patchy, generally the tropics have the shortest detection times.

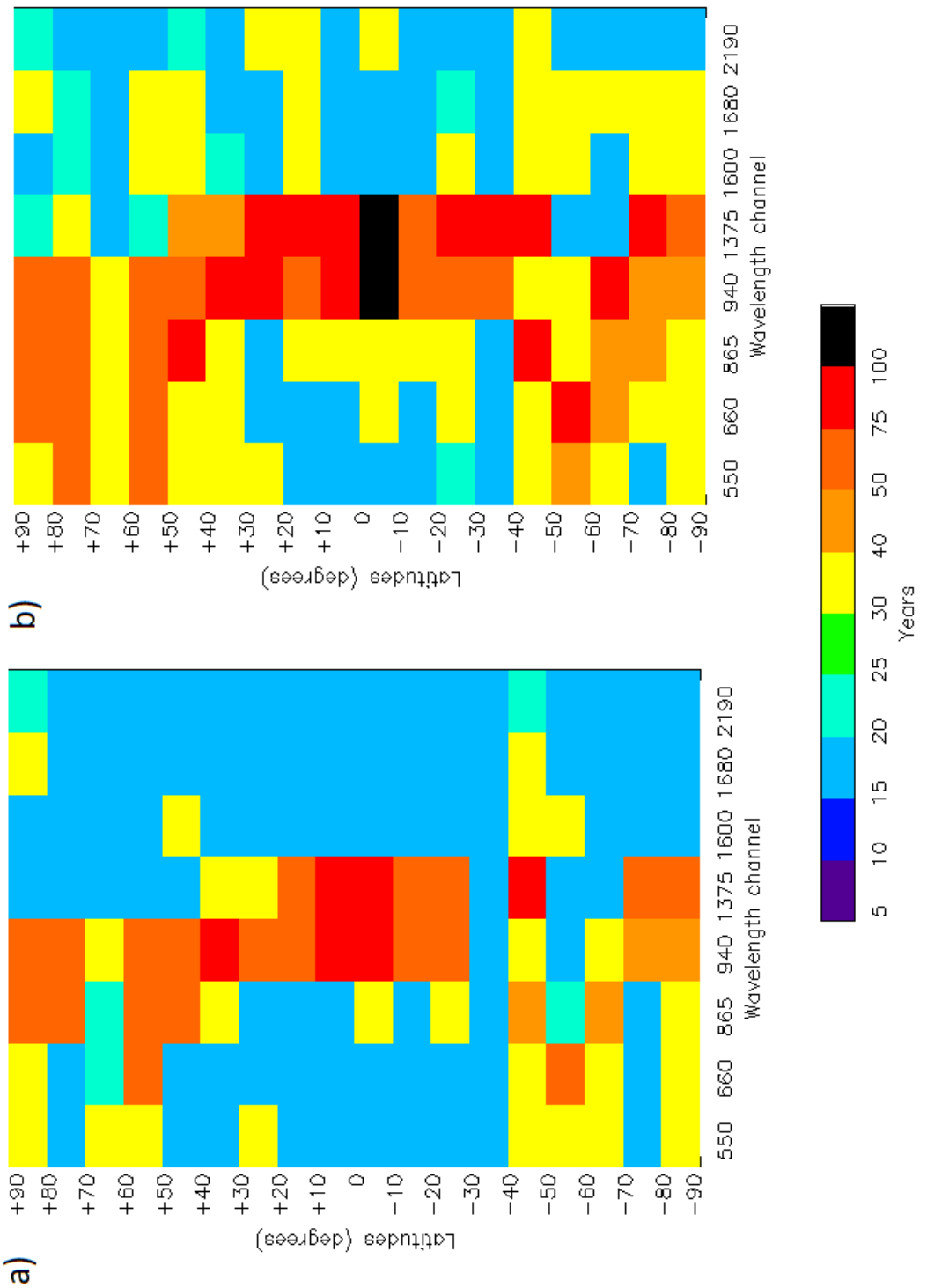


FIGURE 5.10: a) The detection times under all sky conditions for 5 year data sets and 10 year gaps, b) the same as (a) accounting for measurement uncertainty.

5.4 Summary

In this chapter, the effect of data gaps on the ability to detect a signal was investigated. For a TRUTHS-type mission, it is unlikely that a continuous data record would be obtained from overlapping, successive launches, therefore it is highly probably there will be gaps in the data record. To address the issues of gaps, the same COSSE data as those used in Chapter 4 were employed for this gap-analysis. The 10° resolution data for only eight carefully chosen wavelengths were employed. Data record lengths of 3 and 5 years were chosen, followed by gaps of 10, 15, 20 and 25 years based on possible launch scenarios, before a further 3 or 5 years of data, and so on.

In this chapter a different method has been used in order to carry out the time series analysis. This method was used as it calculates the noise from the A2 scenario data, as opposed to from the control run COSSEs as in Chapter 4. In order to check that the methods were in broad agreement, the detection times for continuous data sets were calculated using both methods. This showed that in both clear and all sky conditions, the detection times at most wavelengths and latitude bands were within 10 years of each other. The largest differences were generally at higher latitudes and in the water vapour absorption bands (940 and 1375nm). This was anticipated due to the fact that the water vapour absorption obscures any other climate change signals, as shown in the previous detection time results from Chapter 4. There was also more variation between the detection times under all sky conditions, which is also due to the increase in natural variability from the addition of clouds.

Figure 5.4a and b showed the detection times for all gap configurations for clear sky conditions. It was shown that in the majority of latitude bands and wavelengths, the detection times were 15-30 years depending on gap length. There were, however, areas where the detection time was long, i.e. longer than 40 years. These detection times mainly occurred at high latitudes around the Arctic and Antarctic. This is consistent with the longer detection times seen in the continuous record in these regions (Chapter 4 and Figures 5.1 and 5.2), thought to be due to the combination of ice melt and regrowth.

The detection times for the all sky scenario, shown in Figure 5.7a and b, increase as expected due to the increased variability associated with cloudy conditions. In the 3 year data period example, the detection times increase at most wavelengths and latitude bands. Conversely, using 5 year periods of data results in detection times similar to those seen in the clear sky case (15-40 years). The wavelengths that show an increase in detection time is at 940nm and 1375nm, which mainly has detection times of 40-100 years.

Comparing between the 3 and 5 year record lengths, it is apparent in both clear and all sky conditions that the 5 year records produce the most consistent detection times, and generally the shorter detection times. Five year missions separated by 10 year gaps would provide the fastest detection times across the largest number of wavelengths and latitude bands. By analysing Figure 5.7b for all sky conditions, the 5 year records with 10 year gaps provide the quickest detection times in 78% of cases (considering the 8 wavelengths and 18 latitude bands).

It is important that detection of the signals of climate change is achieved as quickly as possible, so that mitigation strategies can be employed at the earliest opportunity. The calibration accuracy of other satellites such as CERES and MODIS are discussed in Fox, (2010) and Wielicki et al., (2013), along with the estimated time it would take for them to make detections. This is shown in Figure 1.4 in Chapter 1. CERES would take 25 years and MODIS would take 40 years to detect 100 % positive cloud feedback (with 95% calibration accuracy), whereas TRUTHS is predicted to take only 12 years. Reducing to 50% positive cloud feedback lengthens the timescale to 40 years for CERES. Though this is assuming that there is a continuous, overlapping and well intercalibrated record from the CERES instruments. While it may be possible for CERES to detect a certain signal in 40 years, based on the aforementioned assumptions, it means that a minimum of 40 years will pass before mitigation strategies can be decided on and then enforced. Therefore it is important to choose a configuration for TRUTHS that results in detection times that are significantly less than 40 years, and potentially <30 years to ensure early detection and mitigation.

Figure 5.11 compares the detection times from the 5 year record with 10 year gap configuration, to the detection times for a continuous data set (for the same wavelengths and 10° latitude bands, as shown in Figure 5.2a). This figure shows the number of wavelengths at each latitude bands which would provide a detection within 30 years if the 10 year gap configuration (discussed above) were used for data in all sky conditions. In 14 of the 18 latitude bands, the number of detections within 30 years with gaps is less than when using a continuous data set. However it is interesting to note that there are 3 latitude bands where the number of detections within 30 years is unchanged when adding gaps into the record. All three of these cases are around the tropics (0-10 and 10-20°N, and 10-20°S), which is a consequence of generally very short detection times. Finally, at 30-40°S the gapped data leads to detections at all 8 wavelengths which outperforms the continuous data set. Figure 5.2a shows that for the continuous data set the detection time at this latitude band is only larger than 30 years at 940nm (where the detection time is 50-75 years). As discussed earlier, 940nm shows a lot of variability due to the fact it is a water vapour absorption band, and in all sky conditions, there is added variability from the clouds. It is possible that the addition of gaps into the 940nm reflectance time series only allows the use of specific data points that happen to show a strong signal, resulting in a shorter detection time.

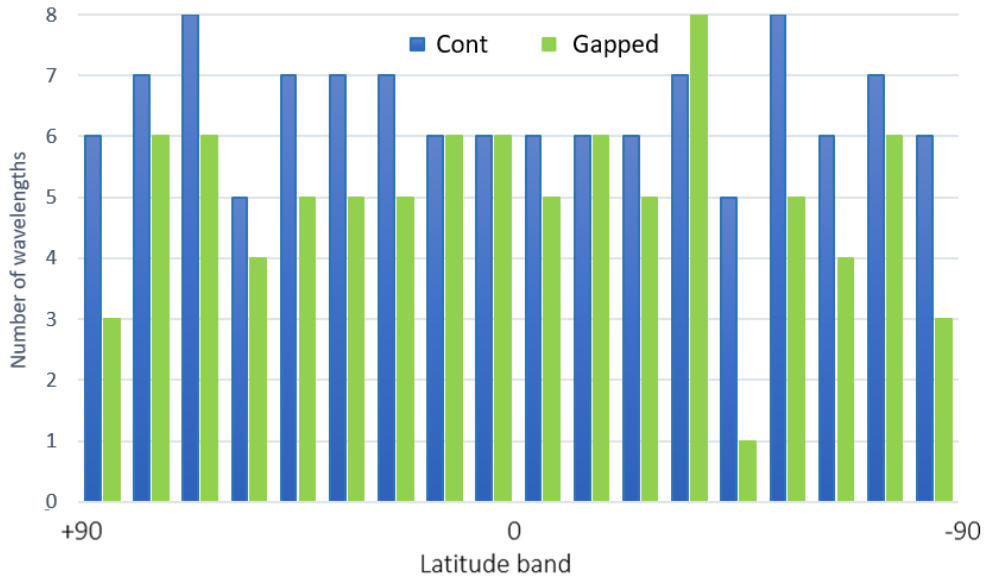


FIGURE 5.11: The number of wavelengths per latitude band with a detection time of less than 30 years using the continuous data set (blue) or using 5 year records with a 10 year gap (green) under all sky conditions.

Looking carefully at the detection times in Figure 5.7b for the all sky conditions, it is obvious that the longer wavelengths (1600, 1680 and 2190nm) have the shortest detection times. This implies that not only is the signal stronger in these regions but also that the noise is relatively small, allowing faster detections. These wavelengths also have shorter detection times at the higher latitude bands where the visible wavelengths have long and variable detection times. This shows that the longer wavelengths are well suited for making detections at these higher latitudes. Since 1600 and 1680nm are used for identifying ice clouds, it may be that (under these all sky conditions) there is a significant change in the amount of ice clouds at higher latitudes which results in a large signal to emerge. Hence this is why there are faster detection times at these wavelengths in the Arctic and Antarctic regions, and not at the visible wavelengths which cannot distinguish between ice and water clouds.

The final choice of mission design depends on the fundamental questions that need to be answered. To consider this, only the results for all sky conditions are used from Figure 5.7b for 5 year record lengths. If it is important to have full global coverage and fast detection times, then based on an A2 style scenario, a focus on the longer wavelengths such as 1600-2190nm would provide the quickest detction times. In this case, it is possible to have detection times shorter than 40 years almost everywhere with any of the gap lengths and 5 years of data. If, as mentioned above, the 30 year timescale is indeed the limit, a maximum gap length of 20 years can be allowed. However, as discussed, a 5 year mission length, with the shortest gap possible (10 years in these studies) is the optimal mission design. It is most important to be able to make the most number of detections possible as quickly as possible, in order to employ mitigation strategies. If it is more important to have fast detections at all wavelengths in one region, then it would be best to focus on the 30-40°S band with the 10 year gap. 60-70°N also presents detection times less than 30 years with a gap length of 15 years. However, in this scenario the tropics (40°S-40°N) provide short detection times at all wavelengths except those in the water vapour bands. Therefore this may be a good compromise to obtain fast detection times at the most wavelengths and across the largest global region.

Finally, while the measurement uncertainty was considered only for one gap configuration, it gives a good indication of how the detection times increase once the uncertainties are included in the calculations. Here both the instrument uncertainty, and natural variability were taken into account. It was further shown that the water vapour bands should not be used for signal detection, and that the mid to high latitudes now have detection times longer than the 30 year timescale at the visible wavelengths, likely due to the high natural variability. The tropics, however, generally have the lower detection times and would be the better region to make detections. Finally, the detection times increase at 1600/1680/2190nm which makes it more difficult to detect signals at these wavelengths at some of the latitudes. However, even with the increase in detection times, 36% of the wavelengths and latitudes considered here have detection times less than 30 years and so relatively quick detections can still be made.

Chapter 6

Conclusions and Future Work

6.1 Conclusions

It has been discussed that it is of great importance to accurately measure the ERB and various other ECVs in order to evaluate climate change, and attribute these changes to specific causes. To address these issues, the TRUTHS satellite has been proposed. The design of TRUTHS will focus on high radiometric accuracy and will be SI traceable in orbit, with its primary aim being to perform in orbit calibration of other EO satellites to also improve their accuracy. It also has the capabilities to measure the TSI and SSI, as well as the Earth reflected solar radiation. The research carried out here investigated the ability of a TRUTHS-like intrument to detect the small signals of climate change above the background noise of natural variability. In order to do this, the effects of various factors on the TOA reflectance spectrum were investigated to give an understanding of the patterns of change seen, and subsequently the time it would take a TRUTHS-like instrument to detect a signal of change was calculated. The effect of spatial resolution was investigated, as well as the effect of surface type on the detection time. Finally, gaps were added into the data set to simulate realistic records, and the effects of these on the detection times was calculated, as well as an investigation into the optimum gap and satellite lifetime configuration. For these studies, a 100 year COSSE data set was used that had been simulated based on the IPCC AR4 A2 emissions scenario. From these data the TOA reflectances were then calculated.

In order to gain an understanding of which variables affect the TOA reflectance spectrum, a variety of sensitivity studies were carried out. These were ozone levels, surface albedo, aerosols and both water and ice clouds. The ozone sensitivity studies show that a five-fold increase in ozone levels results in a decrease in TOA reflectance of 0.025 in the Chappuis ozone absorption bands at 500-700nm. There is a larger effect of approximately 0.23 around 300nm where the Hartley-Huggins absorption band is situated. The effect of aerosols was investigated by comparing two different aerosol types; urban aerosol and desert aerosol. Both aerosol types contain insoluble and water soluble components, as well as soot, however the desert aerosol also contains mineral components. These studies were also carried out over two different surface types which showed that the impact of the desert dust aerosol on the TOA reflectance appears to be more sensitive to the underlying surface type (as shown by the change in sign when moving from an ocean to vegetated surface). The same effect is seen at visible wavelengths for the urban aerosol, however the soot component in the urban aerosol causes absorption in the NIR over both surfaces.

The albedo sensitivity studies initially focussed on spectrally invariant surfaces for simplicity and these showed a linear relationship between the albedo and TOA reflectance, however this study was then extended to consider spectrally dependent surfaces. These surfaces were desert sand, green grass, and an ocean surface. The ocean albedo had little spectral dependence but since the surface albedo ranged between 0.016 to 0.03 at all wavelengths, this significantly reduced the TOA reflectance compared to the other surface types. The grass albedo showed low values across the visible wavelengths, but then a significant increase in the albedo at the red edge. Both the sand and grass albedos showed large variation across the wavelengths, which was reinforced in the TOA reflectance spectra and shows how important the influence of surface albedo and surface type are on the TOA reflectance.

Adding cloud increased the TOA reflectance since they were brighter than the underlying surface used in these simulations, however varying the cloud properties had different effects on the reflectance spectra. For both water and ice clouds, the effects of doubling the cloud thickness and increasing the height of the cloud by 1km were

investigated. In both ice and water clouds, an increase in the TOA reflectance was seen when doubling the geometrical thickness of the cloud, though the change was larger in the water cloud reaching 0.009 compared to the same change in the ice cloud, which resulted in a change of 0.006. There was also an increase in reflectance when the cloud height was increased (maxima of 0.03 for water clouds, and 0.02 for ice clouds). The effect of changing the cloud droplet properties was also investigated by varying the effective radius. Increasing the effective radius of the water cloud droplets from 10 to 15 microns decreased the TOA reflectance by the largest amount of all the cloud variables studied. This is because larger particles have a larger absorption cross section, and therefore a greater proportion of radiation is absorbed than scattered. The same response was seen in the ice cloud example, where the effective radius was increased by the same amount to 25 microns. However, the spectral shape of the change was different in this scenario due to significant changes in the asymmetry parameter and single scattering albedo across the spectrum for ice particles.

Specific studies were performed for the Arctic, since the COSSE simulations used in this thesis identified high levels of noise and variability in the polar regions. For these studies, three main variables were investigated to examine the effect on the radiation and the interaction between these variables. Here, the surface albedo, (water) cloud optical depth and solar zenith angle were varied during the Arctic summer. While previous studies showed how large the effect of surface albedo and solar zenith angle on the TOA reflectance can be, this study showed that increasing the cloud optical depth from 2 to 8 increases the radiation that returns to TOA by 20%. Each of these variables (solar zenith angle, surface albedo and cloud optical depth) significantly affects the shortwave radiation, and in the polar regions there is a wide range of surface albedos (from dark ocean to bright snow and ice) as well as the effects of solar zenith angle and cloud conditions to consider. This provides a qualitative explanation for the large variability seen in the polar regions.

The final sensitivity study investigated the effect of water vapour absorption in the atmosphere on the TOA reflectance. By increasing the water vapour levels over two different surfaces - a dark ocean and a brighter grass surface - it was shown that the

effect on the TOA reflectance was more significant over the brighter surface. This is because for a low surface albedo, a much larger proportion of the incident radiation is absorbed by the surface meaning there is less available to be affected by the enhanced water vapour upon the return path to the TOA. However, over the brighter surface, the water vapour absorption dominates, because there is still a large amount of radiation available to be absorbed subsequent to surface reflection.

Following the sensitivity studies, a time to detection analysis based on the approach introduced by Feldman et al., (2011)(b) was performed on TOA reflectances calculated from COSSE data for both clear and all sky conditions. These analyses provided an indication of the time it would take to detect a robust signal of change above the noise of the natural variability as described in the simulations. The detection times were calculated for a wavelength range of 300-2500nm, and for two different spatial resolutions for the zonal mean (10° and 1.41°). Firstly, it was shown that detection times are generally lower around the tropics under clear sky conditions, due to the large aerosol forcing that is seen in the A2 emissions scenario. It is also apparent that the detection times are significantly longer in the water vapour absorption bands. This is due to the water vapour obscuring any other signals of climate change that may be there. There are also longer detection times in the high latitudes (around the polar regions and Southern Ocean) at the visible wavelengths. There is more variability in these regions due to sea ice melt and regrowth which prevents signals being detected quickly.

Under all sky conditions, there is a noticeable increase in the detection times in most regions. This is due to the increase in variability from adding clouds, and this variability makes it more difficult to detect a robust trend. However, there are exceptions - for example, the detection times over the Southern Ocean amd Antarctic are shorter in the visible wavelengths when under all sky conditions. This is because the large variability due to sea ice melt and regrowth is obscured by the cloud, and reduces the variability in these regions, leading to shorter detection times.

Regarding the resolution, it is evident that reducing the zonal mean resolution from 1.41° to 10° does not markedly affect the ability to detect signals of change above the

variability. It has been shown that there are more wavelengths at which detections can be made (within both 10 and 20 years, and under both clear and all sky conditions) at the 10° resolution, when compared to using the higher resolution latitude bands.

Having explored the effects of varying zonal mean resolution, a different way of separating the global data was considered. Within a latitude band average, the surface albedo can vary significantly, yet these large variations are suppressed by the averaging. Therefore, it was investigated whether it would be beneficial to separate data points into land and ocean. Looking at the global maps of the detection times, it is possible to identify features according to the wavelength at which the maps are created. For example, at 2190nm which is used for moisture analysis, it is possible to identify various deserts across the globe since they exhibit longer detection times. By separating the data into land and ocean, it was observed that the detection times in the water vapour absorption bands was significantly longer over the land than they were over ocean. This is due to the results discussed in the sensitivity analyses, where the dark ocean surface absorbs most of the radiation and so the water vapour absorption has relatively little effect on the TOA reflectance compared to when there is water vapour over a brighter land surface. However, there are some regions where the detection time is longer in both land and ocean, than it would be if the latitude band was averaged fully. This is due to the individual land and ocean reflectances having larger variability, and this variability is reduced by averaging, allowing a signal to be detected. Therefore, it is concluded that there is no obvious advantage to separating the data into land and ocean.

The final study looked into the effect of adding data gaps into the TOA reflectance time series from the COSSE data. With TRUTHS intending to have a minimum life span of 3.5 years, with hope that this would be extended to 5 years, it is likely that there would be significant gaps in the data record owing to the time between the launch and operation of subsequent instruments. However, thus far the time to detection analyses used an idealised time record, i.e. a continuous data set. The configurations used were based on 3 or 5 year records, with gaps in between ranging from 10, 15, 20 to 25 years. It was shown that in most geographical and spectral regions, the detection times increase

with increasing gap length. This was an expected result since not only are there fewer data points available to detect a signal from, therefore increasing the uncertainty, but longer gaps delay the year at which a detection can possibly be made. Inspecting the resulting detection times showed similar global and spectral patterns that were seen in the continuous data. For example, 940nm and 1375nm both continue to display longer detection times due to the water vapour absorption obscuring any detectable signal. Also, detection times remain longer in the higher latitudes at the visible wavelengths due to the high noise in these regions due to the sea ice melt and regrowth here.

Comparing between using 3 or 5 year data records clearly indicated that detection times are shorter and more consistent when using 5 years of data as opposed to 3. It was also shown that it is beneficial to use the shortest gaps of 10 years, in order to be able to detect signals quicker. It is important that TRUTHS is still able to make detections as fast as possible in order to introduce early mitigation strategies, and faster than other satellite intruments available currently (assuming that current instruments are continuous and there is no change in calibration accuracy). It was previously shown that an instrument with the accuracy of CERES would be able to detect a 50% positive cloud feedback within 40 years, with the aforementioned assumptions, and therefore it would be a minimum of 40 years before mitigation strategies can be employed. It is important that TRUTHS can make detections and subsequent mitigation strategies can be enforced as quickly as possible, and so detections need to be made by TRUTHS within 30 years. With this limit in mind, it is possible to extend to 15 or 20 year gaps.

The impact of measurement uncertainty was also considered, firstly for all sky continuous data sets. This showed that including the measurement uncertainty of 0.3% and natural variability increased the detection times all round, which was expected. The same experiment was run for one of the gapped data sets with 5 years of data and 10 year gaps, also under all sky conditions. This showed that there were some significant increases in detection time, predominantly around the mid to high latitudes for visible wavelengths, likely due to the higher natural variability in these regions. At most latitudes for the longer wavelengths, the detection times increased from 15-20 years to 30-40 years which puts them outside of the 30 year threshold previously

discussed. However, despite these increases, 36% of the cases considered are still detectable within 30 years which means that there is still a lot to be gained from making these measurements.

Finally, the influence on mission design was discussed which highlighted that if the aim is to provide low detection times on a global scale, assuming the A2 emissions scenario, it would be recommended to use long wavelengths such at 1600, 1680 and 2190nm as these wavelengths lead to the shortest detection times, even under all sky conditions. If the intention is to have short detection times in one region at the most wavelengths, then focus should be applied to the tropics, where detection times are shortest for the visible wavelengths and the long wavelengths mentioned above. The water vapour absorption bands at 940nm and 1375nm still lead to long detection times globally. Unless the intent is to detect signals in the water vapour, it is recommended that these two wavelengths are not used for trend detection under this emissions scenario.

In conclusion, it has been shown that TRUTHS would significantly help to detect trends in the climate record and is very much worthwhile as a mission. It has been shown that even in the worst case scenario (all sky conditions, with gaps in the record and considering measurement uncertainty), there are still several wavelengths and latitude bands at which climate change trends can be detected within 30 years or less. With shorter gaps between missions, or with a slightly longer mission lifetime, it would be possible to make these trend detections even faster. With it's high radiometric accuracy, TRUTHS will be quicker to detect the small signals of climate change above the background noise of natural variability than other satellite missions, which ultimately leads to quicker and more specific mitigation strategies being employed. This is also a more economical solution as different, tailored mitigation strategies could be employed in various regions due to the trends detected, rather than wasting time and money on a global strategy that is ineffective for vast areas. It was shown in Chapters 4 and 5 how the detection times vary with latitude band and global region, and due to the different processes occurring in these areas. This shows that with the high spatial and spectral resolution of TRUTHS, the trends detected in specific areas may be attributed to certain

processes which would futher our understanding of climate change. Also, while it will take time to detect these trends, the other motivation for TRUTHS is to 'upgrade' the current EO system and inter-calibrate other satellites to maintain accuracy, which is a goal that can be achieved immediately once the satellite has launched.

6.2 Future Work

There are many directions that can be explored in order to further this research. Firstly and fundamentally, this research was only carried out for one of the IPCC climate change scenarios. Within the same IPCC report (IPCC, (2000)), there are 6 groups of identified emissions scenarios - A1F1, A1B, A1T, A2, B1 and B2. These scenarios cover a wide range of possibilities as to how the global climate could change over time. However, it is important to note that there are more recent IPCC reports (IPCC, (2013)), and therefore more recent ideas of the way in which global emissions will evolve. For direct comparison with this work, however, the emissions scenarios from the same report are considered.

The A2 scenario is one of the 'strongest' emissions scenarios, in that it includes large increases of CO_2 and CH_4. The A1F1 is the other option for the strongest emissions scenario which displays slightly larger CO_2 emissions, but lower CH_4 emissions than the A2 scenario. The same analysis could be run on at least another scenario that is classifed as one of the 'weakest', e.g. A1T or B1 which both display the lowest emissions values of all the scenarios, with the B1 scenario showing the lowest values by 2100 (IPCC, (2000)). By repeating the above work for both the strongest and weakest emissions scenarios, it would provide detection times for the two extremes of predicted climate change, and should encapsulate the full range of possibilities within this range. Since it remains highly uncertain how the climate will evolve in the future, it would be interesting to extend this research to cover more of the different scenarios in order to provide a deeper understanding. For example, the A1B, A1T and B1 scenarios all display a peak in CO_2 emissions at 2050 reducing by 2100. Exploring these scenarios would give an indication of detection times where CO_2 is not constantly increasing as

is the case in the A2 scenario. Also, in all except the A2 scenario, the SO_2 levels are decreasing over time though the A1F1 and B2 scenarios combine steadily increasing CO_2 with decreasing SO_2 which would provide an interesting comparison with the A2 scenario results to investigate the effect of SO_2.

Another aspect to explore is to repeat the analysis using the same scenario, but to use a different climate model for the simulations. It would be wise to repeat with two different climate models with different climate sensitivities; one with high sensitivity and one with low climate sensitivity. The climate sensitivity of a model is the change in the global mean surface temperature due to a doubling of CO_2 concentration. As above, using two models with extreme climate sensitivities should encompass the range of possibilities in the simulations, and therefore the detection times.

It would also be interesting to generate the spectral radiances from selected CMIP6 (Coupled Model Intercomparison Project Phase 6, Eyring et al., (2016)) simulations which are being carried out for the next IPCC report. For example, the selected simulations should include a weak and a strong emissions scenario (pathway), again to cover the spectrum of results. The radiances can be calculated using a fast and accurate radiative transfer model, such as PCRTM-SOLAR from Liu et al., (2016). PCRTM-SOLAR functions within the required wavelength range of 300-2500nm and has the capabilities for both clear and all sky conditions. It would be important to also know the cloud, surface types, and aerosol profiles from the simulations in order to aid the analysis and attribution of changes in the TOA reflectances that can be subsequently calculated from the radiances. The purpose of this is to then have radiances for a variety of emissions scenarios, and also from a selection of the models that make up CMIP6, that extend further into the future and enable a more complete analysis.

Further work should be conducted on the method used to calculate the time to detect itself. In certain regions the evolution of the TOA reflectance is non-linear in time, and therefore the question must be asked as to whether a linear model is the best option. In most areas under clear sky conditions, the TOA reflectance peaks halfway through the record, following the pattern of the sulphate aerosol. It can be argued that while

the time series is not linear, the change in the reflectance is sufficiently large to enable detection during the first half of the record where the reflectance does exhibit linear behaviour. However, if the research were repeated for other emissions scenarios, it cannot be assumed that those reflectances would follow a linear trend and therefore it would be interesting to identify another method and repeat the analysis, and compare the results to investigate the effect of changing the approach. Different non-linear trend estimation methods are discussed in Franzke, (2012). For example, Ordinary Least Squares (OLS) can be used in quadratic or cubic form instead of linearly, or a robust regression could be used.

These studies clearly only look at the ability of TRUTHS to detect change, however, it is important to have studies that also assess the requirements for the intercalibration with other satellites. For example, if for intercalibation purposes there are specific requirements for the orbit of TRUTHS, or the sampling, this may affect the detection times as calculated here. Some investigation has been conducted by Gorrono et al., (2017) into the sources of uncertainty in the intercalibration process, and that, for example, an asynchronous near-polar orbit is required to reach cross-calibration uncertainties of potentially <0.5%.

In summary, there are many interesting avenues to explore in order to extend upon the work shown here. Primarily, the same analysis for different emissions scenarios and also using different climate models with varying degrees of climate sensitivity should be performed in order to investigate the detection times in different cases, in order to provide a deeper understanding of the capabilities of a TRUTHS-like instrument to detect signals of climate change. It is also important to investigate the instrument noise as this has not been considered thus far, and would be expected to increase the detection times obtained here. Finally, since the primary aim of TRUTHS is to cross-calibrate with other satellites in orbit, it would be of interest to investigate whether the requirements for cross-calibration affect the detection times.

Bibliography

Allen, M. ((1999)). "Principles of Quantitative Earth Observation". In: Oxford/RAL Spring School in Quantitative Earth Observation.

Anderson, G.P. et al. ((1986)). "AFGL Atmospheric Constituent Profiles (0-120km)". In: *Environmental Research Papers* 984, p. 1.

Baldridge, A.M. et al. ((2009)). "The ASTER Spectral Library Version 2.0". In: *Remote Sensing of Environment* 113, pp. 711–715. URL: http://speclib.jpl.nasa.gov/.

Barsi, J.A. et al. ((2014)). "The spectral response of the Landsat-8 Operational Land Imager". In: *Remote Sensing* 6, pp. 10232–10251. DOI: 10.3390/rs61010232.

Berk, A. et al. ((1998)). "MODTRAN cloud and multiple scattering upgrades with applications to AVIRIS". In: *Remote Sensing and the Environment* 65, pp. 367–375.

Bhartia, P.K. et al. ((1996)). "Algorithm for the estimation of vertical ozone profiles from the backscattered ultraviolet technique". In: *Journal of Geophysical Research* 101.D13, pp. 18793–18806.

Bojinski, S. and J-L. Fellous ((2013)). *Response by ESA to GCOS: Results of the Climate Change Initiative*.

Bojinski, S. et al. ((2014)). "The concept of essential climate variables in support of climate research". In: *Bulletin of the American Meteorological Society*, pp. 1431–1443. DOI: 10.1175/BAMS-D-13-00047.1.

Bovensmann, H. et al. ((1999)). "SCIAMACHY: Mission objectives and measurement modes". In: *Journal of Atmospheric Science* 56, pp. 127–150.

Brindley, H. and J. Russell ((2013)). "Monitoring the climate system from space: progress, pitfalls and possibilities". In: *Grantham Institute for Climate Change, Briefing Paper No. 9*.

Burrows, J.P. et al. ((1999)). "The Global Ozone Monitoring Experiment (GOME): Mission concept and first scientific results". In: *Journal of Atmospheric Sciences* 56, pp. 151–175.

Chatfield, C. ((2003)). *The Analysis of Time Series, An Introduction*. Vol. Sixth Edition.

Clough, S.A. et al. ((2005)). "Atmospheric radiative transfer modelling: a summary of the AER codes". In: *Journal of Quantitative Spectroscopy and Radiative Transfer* 91, pp. 233–244. DOI: 10.1016/j/jqsrt.2004.05.058.

Collins, W.D. et al. ((2006)). "The Community Climate System Model Version 3 (CCSM3)". In: *Journal of Climate* 19, pp. 2122–2143.

Curry, J. et al. ((1996)). "Overview of arctic cloud and radiaiton characteristics". In: *Journal of Climate* 9, pp. 1731–1764.

Dong, X. et al. ((2010)). "A 10 year climatology of arctic cloud fraction and radiative forcing at Barrow, Alaska". In: *Journal of Geophysical Research* 115. DOI: 10.1029/2009JD013489.

Drury, E. et al. ((2008)). "Improved algorithms for MODIS satellite retrievals of aerosol optical depths over western North America". In: *Journal of Geophysical Research* 113.D16204. DOI: 10.1029/2007JD009573.

Emde, C. et al. ((2015)). "The libRadtran software package for radiative transfer calculations (Version 2.0)". In: *Geoscientific Model Development Discussions* 8, pp. 10237–10303. DOI: 10.5194/gmdd-8-10237-2015.

ESA ((1998)). "Science and research elements of ESA's Living Planet Programme". In: SP-1227.

– ((2006)). "The changing Earth; New scientific challenges for ESA's Living Planet Programme". In: SP-1304.

Eyring, V. et al. ((2016)). "Overview of the Coupled Model Intercomparison Project Phase 6 (CMIP6) experimental design and organisation". In: *Geoscientific Model Development* 9, pp. 1937–1958. DOI: 10.5194/gmd-9-1937-2016.

Feldman, D. et al. ((2011)[a]). "CLARREO shortwave observing system simulation experiments of the twentt-first century: Simulator design and implementation". In: *Journal of Geophysical Research* 116. DOI: 10.1029/2010JD015350.

Feldman, D. et al. ((2011)[b]). "Simulation studies for the detection of changes in broadband albedo and shortwave nadir reflectance spectra under a climate change scenario". In: *Journal of Geophysical Research* 116. DOI: 10.1029/2011JD016407.

Filella, I. and J. Penuelas ((1994)). "The red edge position and shape as indicators of plant chlorophyll content, biomass and hydric status". In: *International Journal of Remote Sensing* 15.7, pp. 1459–1470. DOI: 10.1080/01431169408954177.

Forster, P.M. et al. ((2011)). "Evaluation of radiation scheme performance within chemistry climate models". In: *Journal of Geophysical Research* 116. DOI: 10.1029/2010JD015361.

Fox, N. ((2010)). "TRUTHS: A benchmark mission for climate change and GMES". In: *Proposal for Earth Explorer 8*.

Fox, N. et al. ((2011)). "Accurate radiometry from space: an essential tool for climate studies". In: *Philosophical Transactions of the Royal Society of London A* 369, pp. 4028–4063. DOI: 10-1098/rsta.2011.0246.

Franzke, Christian ((2012)). "Nonlinear trends, long-range dependence, and climate noise properties of surface temperatures". In: *Journal of Climate* 25. DOI: 10.1175/JCLI-D-11-00293.1.

Gao, B-C. and Y.J. Kaufman ((1995)). "Selection of the 1.375-μm MODIS channel for remote sensing of cirrus clouds and stratospheric aerosols from space". In: *Journal of the Atmospheric Sciences* 52.23, pp. 4231–4237.

GCOS ((2003)). *Second report on the adequacy of the global observing systems for climate in support of UNFCCC*.

– ((2011)). *Systematic observation requirements for satellite-based data products for climate*.

Goldberg, M. et al. ((2011)). "The global space-based inter-calibration system". In: *Bulletin of the American Meteorological Society*, pp. 467–475. DOI: 10.1175/2010BAMS2967.1.

Gordon, I.E. et al. ((2017)). "The HITRAN2016 molecular spectroscopic database". In: *Journal of Quantitative Spectroscopy and Radiative Transfer*. DOI: 10.1016/j.jqsrt.2017.06.038.

Gorrono, J. et al. ((2017)). "Radiometric inter-sensor cross-calibration uncertainty using a traceable high accuracy reference hyperspectral imager". In: *ISPRS Journal of Photogrammetry and Remote Sensing* 130, pp. 393–417. DOI: 10.1016/j.isprsjsprs.2017.07.002.

Gürbüz, S.Z., H. Özena, and G. Chanderc ((2012)). "A survey of landnet sites focussing on". In: International Archives of the Photogrammetry, Remote Sensing and Spatial Information Sciences, ISPRS Congress. Vol. XXXIX-B1.

Haigh, J. ((2003)). "The effects of solar variability on the Earth's climate". In: *Philosophical Transactions of the Royal Society of London A* 361, pp. 95–111.

– ((2011)). "Solar influences on climate". In: *Grantham Institue for Climate Change: Briefing Paper No. 5*.

Hansen, J. et al. ((2011)). "Earth's energy imbalance and implications". In: *Atmospheric Chemistry and Physics* 11, pp. 13421–13449. DOI: 10.5194/acp-11-13421-2011.

He, T., S. Liang, and D-X. Song ((2014)). "Analysis of global land surface albedo climatology and spatial-temporal variation during 1981-2010 from multiple satellite products". In: *Journal of Geophysical Research: Atmospheres* 119, pp. 10281–10298. DOI: 10.1002/2004JD021667.

Hess, M., P. Koepke, and I. Schult ((1998)). "Optical Properties of Aerosols and Clouds: the software package OPAC". In: *Bulletin of the American Meteorological Society* 79.5, pp. 831–844.

Hoffmann, Gerd ((2007)). "Principles and working mechanisms of water-filtered infrared-A (wIRA) in relation to wound healing". In: *GMS Krankenhaushygiene Interdisziplinär* 2.2.

Hollmann, R. et al. ((2013)). "The ESA climate change initiative: Satellite data records for Essential Climate Variables". In: *Bulletin of the American Meteorological Society*, pp. 1541–1552. DOI: 10.1175/BAMS-D-11-00254.1.

Hu, Y. and K. Stamnes ((1993)). "An accurate parameterisation of the radiative transfer properties of water clouds suitable for use in climate models". In: *Journal of Climate* 6, pp. 728–742.

IPCC ((2000)). *IPCC Special Report - Emissions Scenarios. Summary for policy makers*.

– ((2007)). *Climate Change 2007: Synthesis report, contribution of working groups I, II and III to the fourth assessment report of the Intergovernmental Panel on Climate Change*, pp. 36–41.

– ((2013)). "Climate Change 2013: The Physical Science Basis". In: *Fifth Assessment Report of the Intergovernmental Panel on Climate Change*.

Jin, X., J. Haniesak, and D. Barber ((2007)). "Detecting cloud vertical structures from radio sondes and MODIS over arctic first year sea ice". In: *Atmospheric Research* 83, pp. 64–76. DOI: 10.1016/j.atmosres.2006.03.003.

Kaufman, Y.J. et al. ((1997)). "Operational remote sensing of tropospheric aerosol over land from EOS moderate resolution imaging spectroradiometer". In: *Journal of Geophysical Research* 102.D14, pp. 17051–17067.

Klassen, S. and B. Bugbee ((2005)). *Shortwave Radiation*.

Knap, W.H., P. Stammes, and R.B.A. Koelemeijer ((2000)). "Discriminating between water and ice clouds using near-infrared AVIRIS measurements". In: *AVIRIS Workshop Proceedings 2000*.

Krummel, P.B., P.J. Fraser, and N. Derek ((2016)). *The 2015 Antarctic ozone hole summary: final report*, p. 27.

Kurucz, R.L. ((1994)). "Synthetic Infrared Spectra". In: *Proceedings of the 154th Symposium of the International Astronomical Union* 19, pp. 523–531.

Leroy, S.S., J.G. Anderson, and G. Ohring ((2008)). "Climate signal detection times and constraints on climate benchmark accuracy requirements". In: *Journal of Climate* 21(4), pp. 841–846. DOI: 10.1175/2007JCLI1946.1.

Li, S. et al. ((2017)). "Sentinel-2 MSI radiometric characterisation and cross-calibration with Landsat-8 OLI". In: *Advances in Remote Sensing* 6, pp. 147–159. DOI: 10.4236/ars.2017.62011.

Liou, K.N. ((2002)). *An introduction to atmospheric radiation*. Vol. 84. International Geophysics Series, Second Edition.

Liston, G.E. and J-G. Winther ((2005)). "Antarctic surface and subsurface snow and ice melt fluxes". In: *Journal of Climate* 18, pp. 1469–1481.

Liu, X. et al. ((2016)). "Development of a fast and accurate PCRTM radiative transfer model in the solar spectral region". In: *Applied Optics* 55.29, pp. 8236–8247.

Liu, X. et al. ((2017)). "Spectrally dependent CLARREO infrared spectrometer calibration requirement for climate change detection". In: *Journal of Climate* 30, pp. 3979–3998. DOI: 10.1175/JCLI-D-16-0704.1.

Liu, Y. et al. ((2012)). "Arctic cloud macrophysical characteristics from CloudSat and CALIPSO". In: *Remote Sensing of Environment* 124, pp. 159–173.

Loeb, N. et al. ((2009)). "Impact of data gaps on satellite broadband radiation records". In: *Journal of Geophysical Research* 114. DOI: 10-1098/2008JD011183.

Martin, S. ((2014)). *An introduction to ocean remote sensing (Second Edition)*. Cambridge University Press.

Mayer, B. and A. Kylling ((2005)). "Technical note: the libRadtran software package for radiative transfer calculations - description and examples of use". In: *Atmospheric Chemistry and Physics* 5, pp. 1855–1877.

Mayer, B. et al. ((2014)). *LibRadtran user's guide*.

Myers, N. ((2013)). *Tropical forests and climate*.

Neeck, S.P., T.J. Magner, and G.E. Paules ((2005)). "NASA's small satellite missions for Earth observation". In: *Acta Astronautica* 56.1-2, pp. 187–192.

Ohmura, A. et al. ((1998)). "Baseline Surface Radiation Network (BSRN/WCRP): New precision radiometry for climate research". In: *Bulletin of the American Meteorological Society* 79.10, pp. 2115–2136.

Ohring, G. and A. Gruber ((2001)). "Climate monitoring from operational satellites: accomplishments, problems and prospects". In: *Advances in Space Research* 28, pp. 207–219.

Palle, E. et al. ((2004)). "Changes in Earth's reflectance over the past two decades". In: *Science* 304, pp. 1299–1301. DOI: 10.1126/science.1094070.

Park, C. ((2001)). *The environment: principles and applications (Second Edition)*.

Patadia, F., E-S. Yang, and S.A. Christopher ((2009)). "Does dust change the clear sky top of atmosphere shortwave flux over high surface reflectance regions?" In: *Geophysical Research Letters* 36. DOI: 10.1029/2009GL039092.

Payne, R. ((1972)). "Albedo of the sea surface". In: *Journal of Atmospheric Sciences* 29, pp. 959–970.

Pilewskie, P. and S. Twomey ((1987)). "Discrimination of ice from water in clouds by optical remote sensing". In: *Atmospheric Research* 21, pp. 113–122.

Platnick, S. et al. ((2003)). "The MODIS cloud products: algorithms and examples from Terra". In: *IEEE Transactions on Geoscience and Remote Sensing* 41.2, pp. 459–473.

Protat, A. et al. ((2007)). "Evaluation of ice water content retrievals from cloud radar reflectivity and temperature using a large airborne in situ microphysical database".

In: *Journal of Applied Meteorology and Climatology* 46, pp. 557–572. DOI: 10.1175/JAM2488.1.

Roberts, Y., P.A. Pilewski, and B.C. Kindel ((2011)). "Evaluating the observed variability in hyperspectral Earth-reflected solar radiance". In: *Journal of Geophysical Research* 116.D24119. DOI: 10.1029/2011JD016448.

Rothman, L.S. et al. ((2005)). "The HITRAN 2004 molecular spectroscopic database". In: *Journal of Quantitative Spectroscopy and Radiative Transfer* 96 (2), pp. 139–204. DOI: 10.1016/j/jqsrt.2004.10.008.

Sandford, M.C.W. et al. ((2003)). "The geostationary Earth radiation budget (GERB) instrument on EUMETSAT's MSG satellite". In: *Acta Astronautica* 53 (11), pp. 909–915.

Schwalb, A. ((1978)). "The Tiros-N/NOAA AG Satellite Series". In: *NASA Technical Report N*.

Shettle, E. ((1989)). "Climate signal detection times and constraints on climate benchmark accuracy requirements". In: *Atmospheric propagation in the UV, visible, IR and mm-region and related system aspects, no.454 in AGARD conference proceedings*.

Stamnes, K. et al. ((1998)). "Numericall stable algorithm for discrete-ordinate-method radiative transfer in multiple scatteringand emitting layered media". In: *Applied Optics* 27.12, pp. 2502–2509.

Stroeve, J.C. et al. ((2012)). "The Arctic's rapidly shrinking sea ice cover: a research synthesis". In: *Climate Change* 110, pp. 1005–1027. DOI: 10.1007/s10584-011-0101-1.

Stubenrauch, C.J. et al. ((2013)). "Assessment of global cloud datasets from satellites". In: *Bulletin of the American Meterological Society*, pp. 1031–1049. DOI: 10.1175/BAMS-D-12-00117.1.

Trenberth, K.E., J.T. Fasullo, and J. Kiehl ((2008)). "Earth's global energy budget". In: *Bulletin ofthe American Meteorological Society*. DOI: 10.1175/2008BAMS2634.1.

UNEP ((1987)). "The Montreal Protocol to the United Nations Framework Convention on climate change". In: *United Nations Environment Program*.

UNFCCC ((1998)). "Kyoto Protocol to the United Nations Framework Convention on Climate Change". In: *COP3, UNFCCC*.

Vaughn, W.W. and D.L. Johnson ((1994)). "Meteorological Satellites - The very early years prior to the launch of TIROS-1". In: *Bulletin of the American Meteorological Society* 75, pp. 2295–2302.

Wallace, J.M. and P.V. Hobbs ((2006)). *Atmospheric Science - An introductory survey*. Vol. 92. International Geophysics Series, Second Edition.

Wang, J., W. Rossow, and Y. Zhang ((2000)). "Cloud vertical structure and its variations from a 20 year rawinsonde dataset". In: *Journal of Climate* 13, pp. 3041–3056.

Weatherhead, E. et al. ((1998)). "Factors affecting the detection of trends: Statistical considerations and applications to environmental data". In: *Journal of Geophysical Research* 103.D14, pp. 17149–17161.

Weatherhead, E.C. et al. ((2017)). "How long do satellites need to overlap? Evaluation of climate data stability from overlapping satellite records". In: *Atmospheric Chemistry and Physics Discussions*. DOI: 10.5194/acp-2016-1156.

Wielicki, B. et al. ((2013)). "Achieving climate change absolute accuracy in orbit". In: *Bulletin of the American Meteorological Society*, pp. 1519–1539. DOI: 10.1175/BAMS-D-12-00149.1.

Wielicki, B. et al. ((2014)). "The CLARREO mission - Earth's climate change observations". In: *CLARREO Science Definition Team Report*.

Wielicki, B.A. et al. ((1996)). "Clouds and the Earth's Radiant Energy System (CERES): An Earth Observing System experiment". In: *Bulletin of the American Meteorological Society* 77.5, pp. 853–868.

Wielicki, B.A. et al. ((2002)). "Evidence for large decadal variability in the tropical mean radiative energy budget". In: *Science* 295.

Wiscombe, W. and S. Warren ((1980)). "A model for the spectral albedo of snow. I: Pure snow". In: *Journal of Atmospheric Sciences* 37, pp. 2712–2745.

Wong, T. et al. ((2005)). "Reexamination of the observed decadal variability of the Earth radiation budget using altitude corrected ERBE/ERBS Nonscanner WFOV data". In: *Journal of Climate* 19.

Zibordi, G. et al. ((2009)). "AERONET-OC: A network for the validation of ocean colour primary products". In: *Journal of Atmospheric and Oceanic Technology* 26, pp. 1634–1651. DOI: 10.1175/2009JTECHO654.1.